


Fall 12-1-2015

## Hydrogen Bond-Mediated Structural Order in Hydroxylated bis-MPA Dendritic Polymers: Experimental and Molecular Dynamics Simulation Study

Maliha N. Syed  
*University of Southern Mississippi*

Follow this and additional works at: <https://aquila.usm.edu/dissertations>

 Part of the [Biological and Chemical Physics Commons](#), [Condensed Matter Physics Commons](#), [Materials Chemistry Commons](#), [Physical Chemistry Commons](#), and the [Polymer Chemistry Commons](#)

---

### Recommended Citation

Syed, Maliha N., "Hydrogen Bond-Mediated Structural Order in Hydroxylated bis-MPA Dendritic Polymers: Experimental and Molecular Dynamics Simulation Study" (2015). *Dissertations*. 202.  
<https://aquila.usm.edu/dissertations/202>

This Dissertation is brought to you for free and open access by The Aquila Digital Community. It has been accepted for inclusion in Dissertations by an authorized administrator of The Aquila Digital Community. For more information, please contact [Joshua.Cromwell@usm.edu](mailto:Joshua.Cromwell@usm.edu).

HYDROGEN BOND-MEDIATED STRUCTURAL ORDER IN HYDROXYLATED  
BIS-MPA DENDRITIC POLYMERS: EXPERIMENTAL AND  
MOLECULAR DYNAMICS SIMULATION STUDY

by

Maliha Naqvi Syed

A Dissertation  
Submitted to the Graduate School  
and the School of Polymers and High Performance Materials  
at The University of Southern Mississippi  
in Partial Fulfillment of the Requirements  
for the Degree of Doctor of Philosophy

Approved:

---

Dr. Sergei Nazarenko, Committee Chair  
Professor, School of Polymers and High Performance Materials

---

Dr. Robert Lochhead, Committee Member  
Professor, School of Polymers and High Performance Materials

---

Dr. Robson Storey, Committee Member  
Distinguished Professor, School of Polymers and High Performance Materials

---

Dr. James Rawlins, Committee Member  
Associate Professor, School of Polymers and High Performance Materials

---

Dr. Derek Patton, Committee Member  
Associate Professor, School of Polymers and High Performance Materials

---

Dr. Jeffrey Wiggins, Committee Member  
Associate Professor, School of Polymers and High Performance Materials

---

Dr. Karen S. Coats  
Dean of the Graduate School

December 2015

COPYRIGHT BY  
MALIHA NAQVI SYED  
2015

## ABSTRACT

# HYDROGEN BOND-MEDIATED STRUCTURAL ORDER IN HYDROXYLATED BIS-MPA DENDRITIC POLYMERS: EXPERIMENTAL AND MOLECULAR DYNAMICS SIMULATION STUDY

by Maliha Naqvi Syed

December 2015

Dendritic architectures are echoed throughout nature. While the significance of these pervasive patterns is not entirely clear, connections between their structures and physical properties are fascinating to contemplate. Particular interest has been paid to a family of synthetically manufactured and commercially available dendritic polymers based on 2,2-bis(hydroxymethyl) propionic acid (bis-MPA) as a monomer. Composed of two hydroxyls and a carboxyl group, bis-MPA based structures hydrogen bond (H-bond) profusely. Given the high concentration and unique spatial orientation of end-groups, as well as the multitude of carbonyl, ester, and ether interior H-bond acceptors, a set of distinct H-bond organizations may be observed for these dendritic systems. The purpose of this dissertation was to elucidate the H-bond organizations in relation to bulk thermal and free volume properties of bis-MPA based dendritic polymers, with an emphasis on developing a fundamental understanding of the extent to which randomly branched hyperbranched polymers (HBPs) of this type compare to perfectly branched dendrimers.

Chapter I of this dissertation provided a background of dendritic architectures, specifically those based on bis-MPA, relevant structure-property relationships, including those related to H-bonding, and a brief synopsis of molecular dynamics (MD) type computer simulations. In Chapter II, atomistic simulations of bis-MPA dendrimers and

HBPs allowed the visualization of the globular molecular shape and end-group distribution of these complicated architectures. Through synergistic efforts of experiments and computer simulations “chain-like clusters” of O-H $\cdots$ O groups were found to pervade the bulk structure of both dendrimers and HBPs. Because these clusters bore remarkable similarity to analogous H-bond organizations in structural fluids such as water and hydrogen fluoride, it was speculated that the chain-like clusters may be responsible for specific favorable bulk physical properties of bis-MPA dendrimers. In Chapter III, the imperfect branching of the HBP was found to lead to a H-bond organization which was not prevalent in the perfectly branched analogous dendrimers, highlighting a fundamental structure-property difference between the two systems. The linear unit imperfections in the HBP were instrumental in forming a H-bond driven mesophase, which was composed of pseudo-hexagonally packed, parallel and straight, laterally H-bonded linear chain segments with cylindrical symmetry. The dynamics of mesophase ordering upon annealing were also revealed. In Chapter IV, the effect of H-bond ordering and generation number on the volumetric and thermodynamic parameters of bis-MPA based HBPs was addressed. Pressure-volume-temperature (PVT) properties were simulated and experimentally probed. The simulated bulk volumetric and thermodynamic properties were approximately similar to analogous experimental parameters, supporting that MD simulations can predict bulk properties of dendritic polymers. Thus, as the significance of dendritic architectures continues to be a mystery, the current understanding of the structure-property relationships of these fractal macromolecules has been improved through this dissertation work.

## ACKNOWLEDGMENTS

A great number of exceptional individuals were instrumental in the completion of this dissertation. Amongst them I'd like to acknowledge....

...My advisor, Dr. Sergei Nazarenko, for providing unfailing and whole-hearted guidance while simultaneously challenging and supporting me throughout my PhD. Thank you for your mentorship during my journey to improve my understanding of fundamental science.

...Dr. Robert Lochhead, my co-advisor, for guiding my educational and career decisions since my first year at USM. Thank you for always asking the right investigative questions and reminding me of the inspiration and creativity behind science.

...My committee members, Dr. Robson Storey, Dr. James Rawlins, Dr. Derek Patton, and Dr. Jeffrey Wiggins, and also other faculty members, such as Dr. William Jarrett, for their guidance and contribution to my education.

...Dr. Brian Olson for passing on his endless wisdom of computer simulations. Thank you Brian for writing and sharing your modeling scripts with me. This work would not have been possible without your expertise and generous spirit.

...Financial support from the School of Polymers and High Performance Materials (SPHPM), and the National Science Foundation (NSF) through the Experimental Program to Stimulate Competitive Research (EPSCoR), and GK-12 Program "Connections in the Classroom: Molecules to Muscles," Award # 0947944.

...Dr. Lei Zhu at Case Western Reserve University for kindly testing our materials at the synchrotron X-ray beamline at the Brookhaven National Laboratory.

...My colleagues in the Nazarenko Research Group (NRG) for providing solidarity, brainstorming with me through tough scientific conundrums, and empathizing with me throughout this difficult journey. Thank you Ramesh Ramakrishnan, Vivek Vasagar, Kevin Meyers, Beibei Chen, and many NRG alumni such as Dr. Charles Manzi-Nshuti, Dr. Mukul Kaushik, and Jason Pratt.

...My father, Dr. Ali Naqi Syed, for always supporting my decisions, no matter how eccentric, and my mother Dure Shahwar Syed for at all times providing a listening ear and being my shoulder to cry on. Thank you Ammi and Abu for your unconditional love and hard-work and sacrifice in pursuit of higher education for your children.

...My brothers: Hasan Syed for always believing in me and reminding me to take life easier; Jafar Syed for reminding me to take a deeper look into things and always providing genuine advice.

...Nadine Lipa for being the most wonderful and supportive friend, roommate, and colleague a girl could ask for. It has been a joy to complete this journey with you. Cheers, we did it!; Katrina Knauer, my fellow physical-chemist-partner-in-crime, for laughing, crying, and dancing with me through the good times and the bad; Huma Akhtar for three decades of support, love, fights, and wise words.

...Numerous colleagues and staff in SPHPM for their help, wisdom, and generosity: Brooks Abel, Emily Hoff, Keith Parsons, Andrew Janisse, Bob Peterson, Garret Campbell, Corey Parada, Morgan Heskett, Mark Brei, Dr. Stephen Foster, Dr. David Krzeminski, Dr. Katherine Frank, Stephanie Messer Foster, Dahlia Amato, Wei Guo, Brian Donovan, Christina Konecki, Greg Curtzwiler, Mark Early, David Delatte, April Fogel, Jodi Wiggins, and many others.

## DEDICATION

This dissertation is dedicated to my mother and father, Dure Shahwar and Ali Naqi, who gave me the heart, inspiration, and strength to complete this dissertation.



## TABLE OF CONTENTS

ABSTRACT .....	ii
ACKNOWLEDGMENTS .....	iv
LIST OF TABLES .....	ix
LIST OF SCHEMES.....	x
LIST OF ILLUSTRATIONS .....	xi
LIST OF EQUATIONS .....	xvii
CHAPTER	
I. RESEARCH BACKGROUND .....	1
Introduction	
Dendritic Polymers	
Hydroxylated Bis-MPA Dendrimers and Hyperbranched Polymers	
Hydrogen Bonding	
Molecular Dynamics Simulations	
Research Overview	
II. HYDROGEN BOND ASSISTED CHAIN-LIKE-CLUSTERS IN BIS-MPA DENDRIMERS AND HYPERBRANCHED POLYMERS.....	24
Abstract	
Introduction	
Experimental	
Results and Discussion	
Conclusions	
References	
III. PSEUDO-HEXAGONAL, HYDROGEN BOND-MEDIATED MESOPHASE FORMATION IN BIS-MPA HYPERBRANCHED POLYMERS .....	81
Abstract	
Introduction	
Experimental	
Results and Discussion	
Conclusions	
References	

IV.	BULK VOLUMETRIC AND THERMODYNAMIC PROPERTIES OF BIS-MPA BASED DENDRIMERS AND HYPERBRANCHED POLYMERS .....	116
	Abstract	
	Introduction	
	Experimental	
	Results and Discussion	
	Conclusions	
	References	
V.	CONCLUDING REMARKS AND FUTURE DIRECTIONS.....	146
	APPENDIX.....	153

## LIST OF TABLES

### Table

1.	Contribution of each oxygen acceptor type to cluster formation, and total number of hydrogen bonds for D20, D40, H20, and H40.....	62
2.	O-O neighbor analysis of chain-like clusters for D20 and D40: Average number of nearest neighbors (count) and average displacement between nearest neighbors according to neighbor number, $n_i$ .....	70
3.	O-O neighbor analysis of chain-like clusters for H20 and H40: Average number of nearest neighbors (count) and average displacement between nearest neighbors according to neighbor number, $n_i$ .....	70
4.	Deconvolution results of the angular position ( $2\theta$ ), d-spacing, and intensity corresponding to Peaks 1-4 from the synchrotron X-ray patterns of H20 at 25, 40, 60, 80 and 100°C .....	94
5.	Deconvolution results of the angular position ( $2\theta$ ), d-spacing, and intensity corresponding to Peaks 1-4 from the synchrotron X-ray patterns of H40 at 25, 40, and 60°C .....	95
6.	H20 deconvolution results of angular position ( $2\theta$ ), d-spacing, and intensity corresponding to Peaks 1-4 for non-synchrotron quenched and annealed X-ray patterns .....	103
7.	H40 deconvolution results of angular position ( $2\theta$ ), d-spacing, and intensity corresponding to Peaks 1-4 for non-synchrotron quenched and annealed X-ray patterns .....	104
8.	Scaling and SS Fit Parameters for Experimental Boltorn H20 and H40, as well as simulated D20, D40, and H20.....	138

## LIST OF SCHEMES

### Scheme

1. Divergent synthesis of aliphatic ester dendrimers based on bis-MPA .....7
2. Pseudo-one pot synthesis of Boltorn™ hyperbranched polymers based on a ethoxylated pentaerythritol (PP50) core and bis-MPA repeat unit. The first (i) and second (ii) generation HBP products are shown. Terminal and linear hydroxyls are highlighted in red and blue respectively .....8

## LIST OF ILLUSTRATIONS

### Figure

1. Schematic of the structure of a third generation, AB<sub>2</sub>-tetrafunctional core dendrimer and hyperbranched polymer. The main structural components, such as the central core, shell, and end, or ‘terminal’-groups are highlighted .....2
2. Structures of (a) 2,2-bis(hydroxymethyl)propionic acid (bis-MPA) branching monomer and commonly used core molecules: (b) tri-functional, tris(methylol)propane (TMP), and tetra-functional (c) asymmetric ethoxylated pentaerythritol (PP50) and (d) symmetric pentaerythritol (PE).....5
3. Decrease in viscosity upon alkylation of solid, hydroxylated Boltorn HBP (left) to a viscous liquid HBP with aliphatic chain ends (right).....9
4. Wide-angle X-ray diffraction (WAXD) patterns of Boltorn H20 and H40. The inset displays the WAXD pattern for D.I. water. The pattern for H20 was shifted vertically by 100 units for clarity .....25
5. Chemical structures of the bis-MPA/PP50 dendrimers (a) D20, (b) D40, and (c) D40-CH<sub>3</sub>, which were used in molecular dynamics simulations .....31
6. Five configurational isomers of H20 used to construct the amorphous cell for the MD simulations. Each isomer had a molecular weight of 1749 g/mol and D = 0.100; L = 0.565; T = 0.335<sup>5</sup> .....32
7. Five configurational isomers of H40 used to construct the amorphous cell in MD simulations. Each isomer had a molecular weight of 7323 g/mol and D = 0.165, L = 0.570, T = 0.265<sup>5</sup> .....33
8. Final relaxed amorphous cells of (a) 50 molecules of D20, (b) 12 molecules of D40, (c) 50 molecules of H20, (d) 12 molecules of H40, and (e) 9 molecules of D40-CH<sub>3</sub>. Within each amorphous cell, different colors indicate different molecules, and each cell was on the same scale, indicated by the scale bar .....37
9. Simulated volume-temperature (V-T) points at atmospheric pressure for simulated D20, D40 and H20 systems. The experimental V-T curves at ambient pressure are shown as a dashed line for Boltorn H20 and a dotted line for Boltorn H40.....38
10. Schematic of a hydrogen bond between a donor hydroxyl group, X-H, and an acceptor group, Y-Z. The dotted line (•••) represents the hydrogen bond. The hydrogen donor atom is highlighted in blue and the oxygen acceptor atom in red. The hydrogen bond length and angle are indicated with arrows .....41

11.	Characterization of esterified H40 showing FTIR spectra for Boltorn H40, and 10, 25, 50, 75, and 100% esterified H40.....	42
12.	Calculated ratio of [OH] to [C=O] peak areas as a function of the degree of esterification.....	42
13.	DSC thermograms for Boltorn H40 and the 10, 25, 50, 75, and 100% esterified H40 samples. The glass transition temperature is indicated for each curve .....	44
14.	Glass transition temperature ( $T_g$ ) as a function of degree of esterification of Boltorn H40 .....	44
15.	WAXD patterns of Boltorn H40, and 10, 25, 50, 75 and 100% esterified H40. The X-ray patterns were normalized and stacked vertically for clarity .....	45
16.	Three relatively orthogonal views of a representative molecule from the final amorphous cell of D20, D40, H20, H40, and D40-CH3. The three-dimensional orientation of each molecule is specified by the x,y,z-axes. Each molecule is on the same scale, specified by the scalebar. For D20, D40, H20, and H40 hydroxyl oxygen atoms are highlighted in yellow. For D40-CH3 the terminal methyl carbon atoms are highlighted in yellow. For H20 and H40, the molecules shown are representative of the isomer (a) from Figure 6 and isomer (c) from Figure 7 respectively .....	47
17.	Simulated X-ray scattering patterns for D20 and H20 and experimental WAXD pattern of Boltorn H20 .....	50
18.	Simulated X-ray scattering patterns of D40 and H40 compared with analogous experimental patterns WAXD pattern of Boltorn H40 .....	51
19.	Experimental WAXD pattern of 100% acetylated H40 (top) compared with the simulated X-ray pattern for D40-CH3 (bottom) .....	53
20.	Visualization of linear and cyclic hydrogen bonded clusters of D20 and D40. For each simulated polymer, the amorphous cell containing hydroxyl oxygen and hydrogen atoms is shown to the left and representative clusters are highlighted in blue. Each respective isolated representative cluster, a-f for D20 and a-d for D40, is shown to the right, where blue dashed lines represent hydrogen bonds. The length of each cluster is indicated by the number of hydrogen bonds.....	55
21.	Visualization of linear and cyclic hydrogen bonded clusters of H20 and H40. For each simulated polymer, the amorphous cell containing hydroxyl oxygen and hydrogen atoms is shown to the left and representative clusters are highlighted in blue. Each respective isolated representative cluster, a-d, for H20 and H40, is shown to the right, where blue dashed lines represent hydrogen bonds. The length of each cluster is indicated by the number of hydrogen bonds.....	56

22. Three-dimensional view of “chain-like-clusters” in the final relaxed amorphous cell of D20. Three rotated views of the amorphous cell are shown. Hydrogen and oxygen atoms, as well as covalent and hydrogen bonds are represented by sticks, to form a continuous O-H···O representation of a cluster. The different colors represent clusters of different lengths. Hydroxyl hydrogen and all types of oxygen atoms were included in the clusters .....57
23. Schematic displaying an example of (a) cluster of hydrogen bonded O-H···O groups, (b) single hydrogen bond between two different dendritic molecules, and (c) single hydrogen bond on the same molecule. Free (non-hydrogen bonded) hydroxyls are highlighted in green and with an asterisk (\*). Three different dendritic molecules are depicted, where each molecule name is indicated. (d) Schematic of a hydrogen bonded cluster of O-H···O groups where acceptor oxygen atoms are highlighted in red and the donor hydrogen atoms are highlighted in blue. The ‘atom name’ is specified next to each oxygen and hydrogen atom in the chain. Examples of three potential cluster shapes (e) linear, (f) cyclic, (g) and branched. The red “x” in (g) denotes that branched clusters were not allowed according to the criteria of the hydrogen bond script. For all structures shown, dotted lines (···) represent hydrogen bonds and solid lines (–) represent covalent bonds .....58
24. Average amount of clusters, as a percentage of the total number of clusters, for each cluster length, for D20, D40, H20, and H40. The cluster length is defined by the number of H-bonds in the cluster. Error bars indicate standard deviation over 1000 frames. The inset displays a zoomed-in view of the amount of clusters for a chain length of 5, 6, and 7 hydrogen bonds .....60
25. (a) Isolated hydrogen bonded cluster where dotted lines (···) represent hydrogen bonds and solid lines (–) represent a covalent bonds. The central oxygen atom in the cluster is labeled as O\*. The first, second, third, and fourth oxygen atom neighbors are labeled as O-1, O-2, O-3, and O-4 respectively. (b) Oxygen-oxygen radial distribution function,  $g(r)_{O-O}$ , calculated for carbonyl and hydroxyl oxygen atoms only, for D20, D40, H20, and H40. The dashed line represents the  $g(r)_{O-O}$  of water, replotted from the literature.<sup>1</sup> D20, D40, H20, and H40 curves were stacked vertically .....67
26. The inter and intramolecular  $g(r)_{O-O}$  for D20, D40, H20 and H40, calculated for carbonyl and hydroxyl oxygens, hydroxyl oxygens only, and carbonyl oxygens only .....69
27. Normalized inter- and intramolecular pair correlation function for all oxygen atoms and hydroxyl hydrogen atoms,  $g(r)_{O-H}$ , for (a) D20, (b) D40, (c) H20, and (d) H40. The values for the H-bond length,  $r_{O\cdots H}$ , and hydroxyl covalent bond length,  $r_{O-H}$ , are shown as the maxima of the inter- and intramolecular functions respectively .....73

28.	FTIR spectra for Boltorn H40 between 25-120°C. The curves were stacked vertically for clarity. The hydroxyl and carbonyl stretching vibrations are highlighted .....	87
29.	Frequency shift of hydroxyl (left axis) and carbonyl (right axis) stretching vibration as a function of temperature .....	88
30.	Wide angle X-ray diffraction (WAXD) patterns of Boltorn (a) H20 and (b) H40. Samples were either quenched from the melt or annealed at 60°C for 1 h. The arrows highlight the low intensity peaks at $2\theta \approx 30$ and $42^\circ$ . The annealed curves were stacked vertically above the quenched ones.....	89
31.	Synchrotron X-ray patterns ( $\lambda = 0.1371$ nm) for (a) H20 at 25, 40, 60, 80, 100, 120, and 130°C and (b) H40 at 25, 40, 60, 80, 100, and 120°C. Curves were shifted vertically for clarity where the upper-most curve corresponds to the lowest temperature and the lower-most curve corresponds to the highest temperature. The spacing between each curve is approximately 300 arb. units. The arrows indicate the main reflections .....	90
32.	Peak deconvolution results for the synchrotron X-ray patterns of Boltorn H20 at (a) 25, (b) 40, (c) 60, (d), 80, and (e) 100°C. Each pattern was deconvoluted into four peaks: Peak 1 (blue), Peak 2 (red), Peak 3 (green), and Peak 4 (purple), indicated with arrows in (a) .....	93
33.	Peak deconvolution results for the synchrotron X-ray patterns of Boltorn H40 at (a) 25, (b) 40, and (c) 60°C. Each pattern was deconvoluted into four peaks: Peak 1 (blue), Peak 2 (red), Peak 3 (green), and Peak 4 (purple), indicated with arrows in (a) .....	94
34.	Change in d-spacing and intensity of Peaks 1-4 as a function of temperature for H20 (a) and (b), and H40 (b) and (d). All values were obtained from peak deconvolution.....	97
35.	Schematic of the pseudo-hexagonal packing structure of linear chain segments which form mesophase aggregates in Boltorn hyperbranched polymers. The shape of each linear chain segment was approximated as cylindrical .....	100
36.	Peak deconvolution results for the non-synchrotron X-ray patterns of quenched (a) H20 and (c) H40, and annealed (b) H20 and (d) H40. Each pattern was deconvoluted into four peaks: Peak 1 (blue), Peak 2 (red), Peak 3 (green), and Peak 4 (purple), indicated with arrows in (a).....	103
37.	DSC thermograms for quenched and annealed samples of (a) H20 and (b) H40. Curves were stacked vertically for clarity. The annealing temperature ( $T_a$ ) is indicated next to each curve.....	106



38. DSC thermograms for Boltorn H20 annealed at  $T_a = 40^\circ\text{C}$  for (A) 5 min, (B) 60 min, and (C) 240 min. The curves were stacked vertically for clarity.....108
39. Melting temperature of mesophase aggregates ( $T_m$ ) as a function of annealing temperature ( $T_a$ ) for Boltorn H20 and H40.....109
40. Enthalpy of melting of mesophase ( $\Delta H$ ) at each annealing temperature ( $T_a$ ) for Boltorn H20 (black) and H40 (red). The dashed lines represents  $\Delta H=0$  .....111
41. Experimental volume-temperature curves for Boltorn H20 and H40 at  $p = 0$ . The dashed lines represent the linear fit of the volume at the four highest temperature points. The linear fit was extrapolated over the entire temperature range.....123
42. Melt state thermal expansion coefficient,  $\alpha_m$ , for H20 and H40 at  $p = 0$ .....125
43. Isobaric volume-temperature curves at 10, 20, 30, 40, 50, 60, 70, 80, 90, 100, 110, 120, 130, 140, 150, and 160 MPa for Boltorn (a) H20 and (b) H40.....126
44. Temperature dependence of melt state thermal expansion coefficients,  $\alpha_m$ , for H20 and H40 at 10, 40, and 150 MPa.....127
45. Isothermal compressibility,  $\beta_m$ , curves as a function of pressure for Boltorn (a) H20 between 27-117°C and (b) H40 between 57-117°C. (c) Isothermal compressibility,  $\beta_m$ , as a function of temperature at  $p = 0$  for H20 and H40.....128
46. Average free volume hole-size ( $v_h$ ) as a function of temperature of Boltorn H20 and H40 determined from PALS .....130
47. The variation of the melt thermal expansion coefficient of the hole-size,  $\alpha_{h,m}$ , with temperature .....131
48. SS EOS fit (red dashed line) to experimental specific volume from PVT dilatometry (open circles) for Boltorn (a) H20 and (b) H40.....132
49. (a) Total volume ( $V_{\text{calc.}}$ ) from PVT dilatometry and (b) specific free volume ( $V_f^{\text{SS}}$ ) from SS EOS, as a function of average hole-size ( $v_h$ ) for Boltorn H20 and H40. The dashed lines represent the linear fit for each respective data set .....133
50. Specific (a) free volume ( $V_f$ ) and (b) occupied volume ( $V_{\text{occ}}$ ) and fractional (c) free volume ( $h$ ) (d) occupied volume, ( $y$ ) for Boltorn H20 and H40. Open symbols represent values calculated from the Dlubek approach and the dashed lines represent calculations from the SS EOS.....135

51. Simulated volume-temperature (V-T) points at atmospheric pressure for simulated D20, D40 and H20. The experimental V-T curves at ambient pressure are shown as a dashed line for Boltorn H20 and a dotted line for Boltorn H40.....137
52. The SS fit (dashed line) to the simulated volume-temperature data sets of (a) D20, (b) D40, and (c) H20. Each analogous experimental V-T data set, Boltorn H20 for (a) and (c) and Boltorn H40 for (b) is plotted with the simulated data.....138
53. (a) Free and (b) occupied volume, and fractional (c) free and (d) occupied volume results calculated by the SS EOS for simulated D20, D40, and H20. In each plot, the analogous experimental SS EOS  $V_f$  and  $V_{occ}$  values for H20 (dashed line) and H40 (dotted line) are displayed.....140
54. Schematic of the bis-MPA based 7-mer structural isomers of the (A) perfect dendrimer, (B) hyperbranched polymer, and (C) linear polymer. Structure (D) is of the monomer 2,2-bis(hydroxymethyl)butyric acid, bis-MBA.....149
55. NMR spectra for kinetics of end-capping of Boltorn H40 with (a) hexamethylene diisocyanate and (b) hexyl isocyanate .....151
56. Three-dimensional view of “chain-like-clusters” in the final relaxed amorphous cells of (A) D40, (B) H20, and (C) H40. Three rotated views of the amorphous cell are shown. Hydrogen and oxygen atoms, as well as covalent and hydrogen bonds are represented by sticks, to form a continuous O-H···O representation of a cluster. All types of oxygen atoms were included in the clusters. The different colors represent clusters of different lengths .....153
57. Synchrotron X-ray patterns ( $\lambda = 0.1371$  nm) for Boltorn H20, collected over a wide angular range, at room temperature and higher temperatures. Curves were shifted vertically for clarity. The dashed line indicates Peak 4 ( $2\theta \approx 35^\circ\text{C}$ ) .....154
58. Deconvolution of synchrotron X-ray pattern ( $\lambda = 0.1371$  nm) for Boltorn H20 at room temperature. Peaks 1-3 are shown in grey and Peak 4 is shown in purple at  $2\theta \approx 35^\circ\text{C}$  .....154

## LIST OF EQUATIONS

Equation	
1.	Degree of branching according to Frey and Frèchet.....3
2.	Derivative of potential energy with respect to position .....12
3.	Tait equation of state.....30
4.	Pair correlation function, $g(r)$ .....39
5.	Debye scattering equation, $I(Q)$ .....39
6.	Radius of gyration, $R_g$ .....40
7.	Coordination number for the first coordination shell from $g(r)$ .....71
8.	Calculation of $2\theta$ value corresponding to secondary reflection of amorphous halo through Bragg equation.....101
9.	Simha-Somcynsky equation of state.....119
10.	Simha-Somcynsky equation of state.....119
11.	Scaling parameters for the Simha-Somcynsky equation of state.....119
12.	Universal interpolation expression for Simha-Somcynsky equation of state .....119
13.	Tao-Eldrup equation relating o-Ps lifetime to radius of hole-size .....122
14.	Total specific volume related to hole-size and number density of holes .....133
15.	Number density of holes as defined by thermal expansivity of free volume and thermal expansivity of hole-size .....133

# CHAPTER I

## RESEARCH BACKGROUND

### Introduction

Pure dendrimers, as synthetic monodisperse macromolecules not only hold promise to replace many natural polymers but may also offer advantages over existing synthetic systems. One step away from pure dendrimers, random and irregularly branched hyperbranched polymers (HBPs) offer a middle ground between linear polymers and dendrimers, as their interior partially reacted linear units may lead to unique applications. For both pure dendrimers and HBPs, an inner core of free space is imperative for guest-host applications. Understanding the effect of the large number of end-groups as well as inter- and intramolecular end-group interactions on bulk physical properties is necessary for optimizing dendritic polymer applications. The pervasiveness of dendritic architectures as optimized structures compels an understanding of their fundamental nature by building a bridge between their structural aspects and physical properties, where it is anticipated that their unique non-linear structures may lead to advantages. Attempts have been made to characterize their hydrogen bonding (H-bonding) and structural order imposed by H-bond interactions, but the characterization is incomplete. Also, no thorough correlation has been made between the observed structural order imposed by H-bond organization and bulk thermal and volumetric properties. The main goal of this research dissertation was to elucidate the H-bond organization in relation to the thermal and free volume properties of bis-MPA based dendritic polymers, with an emphasis on developing a fundamental understanding to what extent HBPs of this type are similar or different as compared to perfect dendrimers.

## Dendritic Polymers

The universality of dendritic architectures in both the abiotic (lightning patterns, snow crystals) and biological realms (trees, neurons) was extended into the synthetic world only recently when three decades ago, Tomalia, Vögtle, and Newkome introduced the synthesis of nearly monodisperse, perfectly branched, unique core-shell architectures—called dendrimers.<sup>1,2</sup> Since then, important contributions such as the advent of convergent dendrimer synthesis by Fréchet and coworkers,<sup>3,4</sup> expanded the range of available dendrimers for specialty applications such as drug delivery<sup>5,6</sup> and light harvesting.<sup>7,8</sup> The key structural features of dendrimers, such as a multitude of end-groups, core-shell architecture, high branching density, and globular macromolecular shape, have resulted in unique physical properties as compared to linear polymers.<sup>2-4</sup> Dendritic polymers may therefore represent a class of novel materials with untapped potential for emerging technologies.

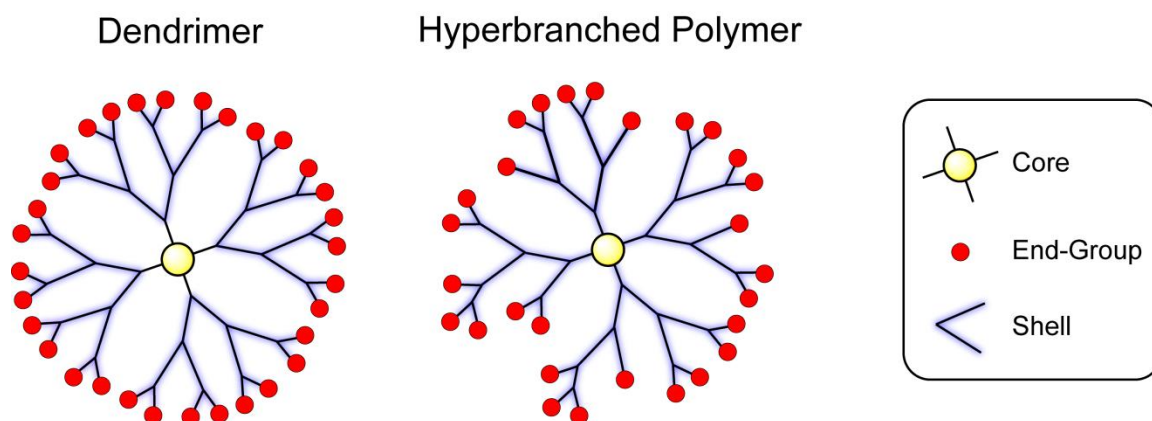


*Figure 1.* Schematic of the structure of a third generation, AB<sub>2</sub>-tetrafunctional core dendrimer and hyperbranched polymer. The main structural components, such as the central core, shell, and end, or ‘terminal’-groups are highlighted.

Today, dendritic polymers are known as highly branched, starburst-shaped macromolecules with nanometer-scale dimensions, similar in size to many biological

molecules. Three major components, shown in Figure 1, define their structure: a central core, an interior branched shell, and an exterior surface composed of numerous functional groups.<sup>9</sup> The interior structure of a dendritic polymer is typically characterized by the number of generations, or layers of repeat units, where dendrimers contain an exact number of generations and hyperbranched polymers (HBPs) are characterized by pseudo-generations (Figure 1). Together these structural components yield products of different shapes and sizes with shielded interior cores, where dendrimers are useful for precision oriented application such as target drug-delivery, catalysis, sensors, light harvesting, and as biomimetic materials, and HBPs find use in many large-scale applications such as rheology modifiers, in specialty coatings, as macromolecular initiators, and as crosslinking agents.<sup>9-15</sup> Considering an AB<sub>2</sub> dendritic system, three distinct structural units termed dendritic, linear, and terminal can be defined as having two, one, and zero reacted B groups. Two formulas for the degree of branching (DB) have been proposed by Frey and Frèchet respectively<sup>16, 17</sup>

$$DB_{Frey} = \frac{2\sum D}{2\sum D + \sum L} \quad DB_{Frèchet} = \frac{\sum D + \sum T}{\sum D + \sum T + \sum L} \quad (1)$$

where  $D$ ,  $L$ , and  $T$  are the mole fractions of dendritic, linear, and terminal units respectively.

As synthesizing larger quantities of pure dendrimers is difficult, academic literature regarding bulk property differences between pure dendrimers and HBPs is currently lacking. Since the structure of HBPs is considered intermediate between that of linear polymers and dendrimers, whether the physical properties of HBPs are more similar to the former or latter system needs exploration. In solution, differences have been highlighted as only pure dendrimers show a maximum in the intrinsic viscosity with

increasing molecular weight, which was attributed to a structural transition upon approaching a critical generation number.<sup>18, 19</sup> In the bulk, polybenzylether dendrimers exhibited a similar structural transition, whereas their linear analogues did not.<sup>20, 21</sup> Thus, bulk HBPs may display intermediary behavior, as they do in solution, but this matter needs further assessment.

Currently under debate, the origin of the glass transition for dendritic systems has been attributed to translational motion rather than long-range segmental motion,<sup>22, 23</sup> which is the proposed mechanism for linear polymers. Due to the absence of a sharp increase in the slope of complex viscosity-molecular weight profiles, chain entanglements are not a dominant feature in dendritic systems, leading to lower mechanical strength and lower solution and melt viscosities.<sup>24</sup> The high number of chain-ends play a pivotal role in determining physical properties by enhancing solubility, dramatically altering viscosity and the glass transition temperature ( $T_g$ ), and even causing crystallization.<sup>25-27</sup>

Depending on their strength, secondary interactions between terminal groups can cause significant changes in the physical properties of dendritic polymers such as  $T_g$ , rheological behavior, and thermal and mechanical properties in the bulk state. For a fourth generation polyether dendrimer, increasing chain end polarity from hydroxyl to bromo to cyano, increased  $T_g$  from 315 to 325 to 349 K respectively.<sup>19</sup> An even more dramatic effect due to H-bonding was seen as an increase in  $T_g$  of approximately 128 K transitioning from a benzyl ether terminated HBP to an analogous phenolic terminated HBP.<sup>26</sup> Similarly, an increase in chain end polarity led to a viscosity increase of several orders of magnitude in a hyperbranched polyester series.<sup>25</sup> Thus, the degree and type of

interaction between terminal groups has led to a decrease in free volume, seen through the increase in  $T_g$ , and an increase in mechanical strength which was observed as a dramatic alteration of viscosity.

### Hydroxylated Bis-MPA Dendrimers and Hyperbranched Polymers

One of the most popularly employed families of dendritic polymers utilizes 2,2-bis(hydroxymethyl)propionic acid or “bis-MPA” as a branching monomer (Figure 2), which is a simple aliphatic, pro-chiral molecule with a molecular weight of 134.06 g/mol.<sup>28</sup> Bis-MPA has been extensively utilized as a viable monomer due to its availability and chemical stability with respect to decarboxylation and dehydration. The commercial availability of these highly functional bis-MPA dendritic polymers renders them ideal candidates for potential use in a wide-array of applications spanning the milligram to multi-ton scale.<sup>29</sup> Several reviews regarding the synthesis, properties, and applications of bis-MPA dendritic polymers are currently available.<sup>22, 28, 30</sup>

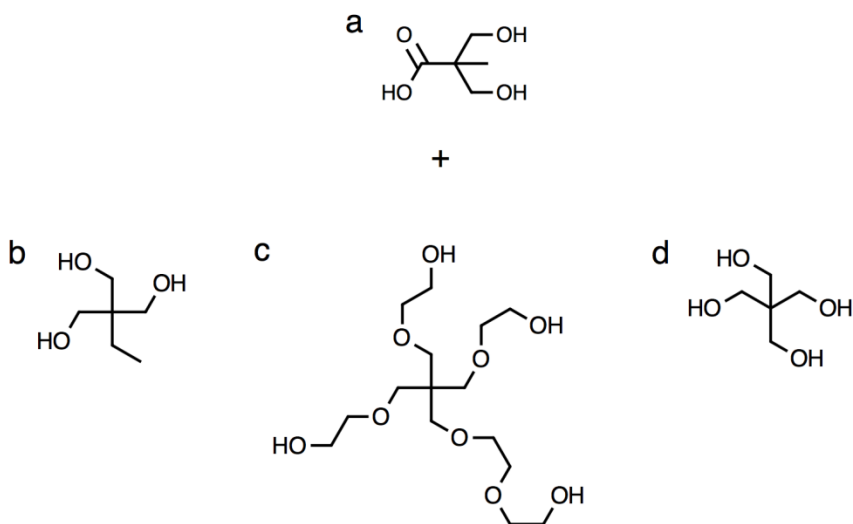
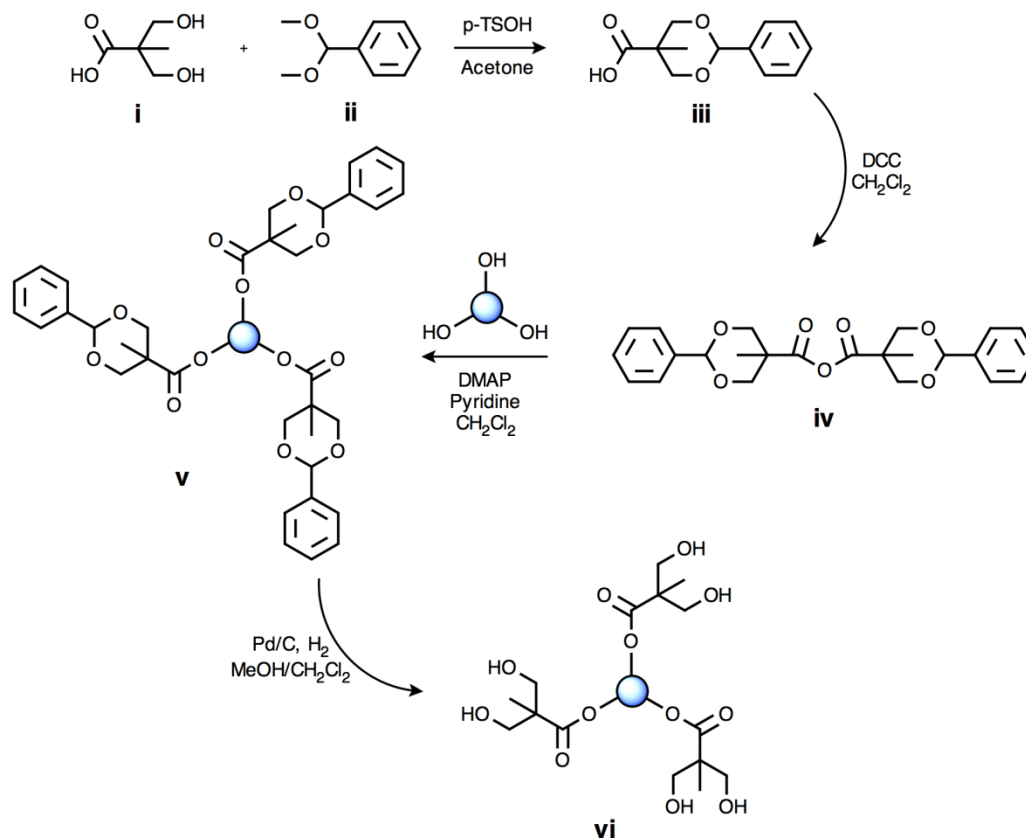


*Figure 2.* Structures of (a) 2,2-bis(hydroxymethyl)propionic acid (bis-MPA) branching monomer and commonly used core molecules: (b) tri-functional, tris(methylol)propane (TMP), and tetra-functional (c) asymmetric ethoxylated pentaerythritol (PP50) and (d) symmetric pentaerythritol (PE).



### *Synthesis and Applications*

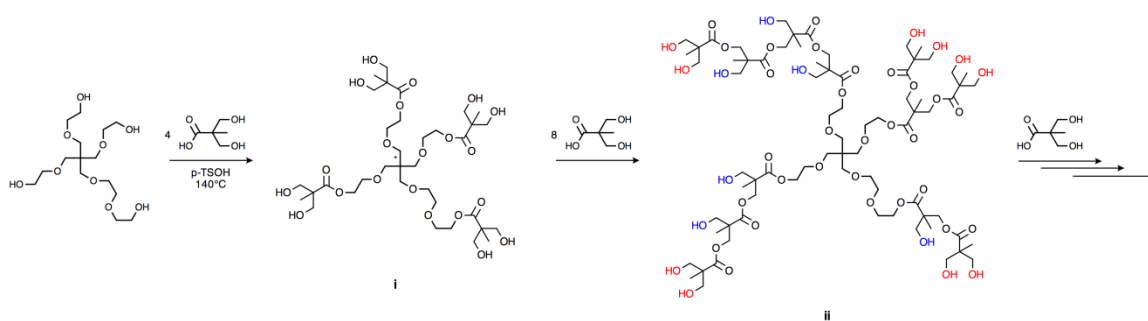
Efficient syntheses have been reported for both “perfectly branched” dendrimers via convergent and divergent iterative methods<sup>31, 32</sup> and “randomly branched” bis-MPA based HBPs via one pot syntheses.<sup>33</sup> Shown in Scheme 1, the divergent synthesis of aliphatic ester dendrimers utilizes an acetal protected anhydride derivative of bis-MPA (iii) as the acylating agent. The diol group of bis-MPA (i) is protected by reaction with benzaldehyde dimethyl acetal (ii) and a catalytic amount of p-toluenesulfonic acid (TSOH) in dry acetone. The anhydride (iv) is then obtained by self-condensation of the acetal building block (iii) in CH<sub>2</sub>Cl<sub>2</sub> using *N,N'*-dicyclohexylcarbodiimide (DCC) as the dehydrating agent. Coupling of iv with the polyol core to produce the benzylidene protected first generation dendrimer (v) is readily accomplished through esterification in a mixture of pyridine and CH<sub>2</sub>Cl<sub>2</sub> using DMAP as the acylating catalyst. The benzylidene protecting groups are removed using a Pd catalyst, producing the first generation hydroxylated dendrimer (vi). To prepare larger dendrimers, the sequence of the anhydride coupling step and the subsequent deprotection by hydrogenolysis is repeated until a dendrimer of the desired size is obtained.<sup>32</sup>



*Scheme 1.* Divergent synthesis of aliphatic ester dendrimers based on bis-MPA.<sup>32</sup>

Since the early 1990s, Perstorp<sup>®</sup> has taken the lead in bringing cost-effective bis-MPA based HBPs, sold under the trade name Boltorn<sup>®</sup>, to the market for a number of industrial applications, in particular for coatings. Boltorn HBPs are synthesized utilizing the pseudo one-pot approach where stoichiometric amounts of bis-MPA, corresponding to each theoretical dendrimer generation, are added in succession. As shown in Scheme 2, the portion of monomer corresponding to the B<sub>f</sub> core molecules is added, and next, the portion corresponding to each successive generation is added to the resulting reaction mixture. The use of a polyfunctional core, B<sub>f</sub>, became popularized in order to preclude gelation and control polydispersity. Two cores with relatively low melting points are commonly used: ethoxylated pentaerythritol (PP50, B<sub>4</sub>), which is liquid at room

temperature, and tris(methylol)propane (TMP, B<sub>3</sub>) which melts at approximately 60-62°C (Figure 2). The two most important parameters in HBP synthesis are the melting temperature of the polyol core and the miscibility of the polyol with bis-MPA. Malmstrom and Hult observed enhanced reaction control when the less polar PP50 core was used, instead of TMP, because the reaction remained phase-separated longer, leading to slower monomer addition.<sup>34</sup> Considering the favorable reaction attributes, the choice of the bis-MPA/PP50 combination is intuitive for large scale, cost-efficient production.



*Scheme 2.* Pseudo-one pot synthesis of Boltorn<sup>®</sup> hyperbranched polymers based on an ethoxylated pentaerythritol (PP50) core and bis-MPA repeat unit. The first (i) and second (ii) generation HBP products are shown. Terminal and linear hydroxyls are highlighted in red and blue respectively.

Due to a multitude of reactive end-groups, high solubility, low solution and melt viscosities, and lack of entanglements, Boltorn type HBPs are commonly employed as crosslinkers, viscosity modifiers, and reactive precursors.<sup>35, 36</sup> Being water soluble, biocompatible and degradable, both the bis-MPA based HBPs and their dendrimer analogues have been studied and proposed for a range of biomedical applications.<sup>37-40</sup> Most recently, novel bis-MPA based HBP/clay nanocomposites were prepared via a solution intercalation method using unmodified sodium montmorillonite clay with water as the solvent.<sup>41</sup> These nanocomposite structures exhibited unusual stepwise intercalation behavior.<sup>42</sup>

### *Hydrogen Bond Organization and Structure-Property Relationships*

While bis-MPA based dendritic polyesters have rapidly become academically and commercially important materials, many of the critical factors that define the relationship between their structure and bulk physical properties have yet to be fully understood. The bulk properties of bis-MPA dendritic polymers are largely governed by the ability of these molecules to form H-bonds both intra- and intermolecularly. This was most vividly demonstrated in the past by functionalizing the hydroxyl groups of bis-MPA based HBPs with non-hydrogen bonding moieties. The  $T_g$  of HBPs modified either with propionate, benzoate, or aliphatic end-groups were dramatically lower than those of the unmodified, hydroxylated HBPs.<sup>25</sup> Amusingly, being solids at room temperature, Boltorn HBPs can be turned into viscous fluids by functionalization with short fatty acids (Figure 3).<sup>27</sup>

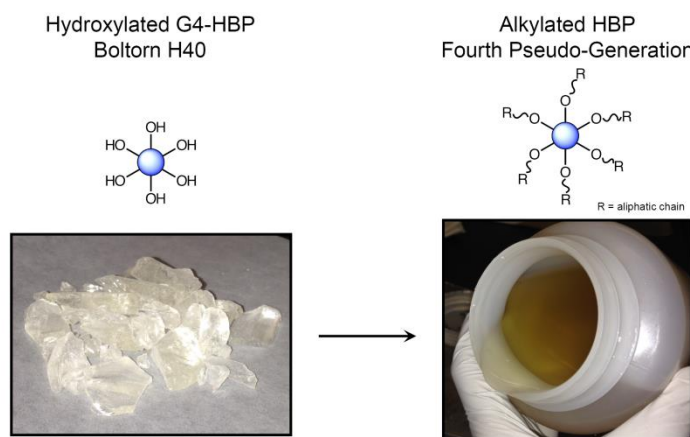


*Figure 3.* Decrease in viscosity upon alkylation of solid, hydroxylated Boltorn HBP (left) to a viscous liquid HBP with aliphatic chain ends (right).

Although scant bulk state comparisons exist between dendrimers and HBPs, a study performed on a fourth generation bis-MPA HBP and its analogous dendrimer unveiled an ordering phenomenon caused by linear units, thus being unique to irregular hyperbranched systems only.<sup>43</sup> Through wide-angle X-ray diffraction, the fourth

generation bis-MPA dendrimer proved impervious to annealing treatments as it showed no change in the shape of its amorphous halo peak. The amorphous halo for the HBP showed an obvious sharpening, which was attributed to structural ordering upon annealing. That the structural ordering was due to H-bonding between linear sequences specifically provides evidence that the different structures of dendrimers and HBPs lead to different H-bond organizations which may further result in varying physical properties.

### Hydrogen Bonding

Hydrogen bonding is a formidable force that can be fine-tuned to alter structure-property relationships and leads to self-assembly, specific interactions during blending, and excellent barrier properties, thus, playing a critical role in a wide range of areas such as medicine, chemical engineering, and biology.<sup>44-48</sup> A hydrogen bond is an attractive interaction between an electropositive donor hydrogen atom from a moiety, X-H, in which X is more electronegative than H, and an electron-rich acceptor atom, Y, from a moiety Y-Z.<sup>49</sup> Through a lapse in electronegativity, electron density is effectively withdrawn from the proton, in X-H, leaving it unshielded and available for H-bonding. The acceptor, Y, must have either polarizable,  $\pi$ , or lone-pair electrons to bond with the proton. In bis-MPA dendritic polymers, hydroxyl groups serve as H-bond donors and ester, carbonyl, ether, and hydroxyl moieties as the acceptors. H-bond strengths can vary from being as strong as covalent bonds and as weak as van der Waals interactions, where their strengths are critically dependent on directionality and the distance between donor and acceptor. Due to the neutral charge but moderate electronegativity of the H-bond acceptors, the H-bonds in bis-MPA HBPs may be classified as ‘moderate’ in strength according to the definition by Jeffrey.<sup>50</sup> Given the high concentration and unique spatial

orientation of end-groups, a set of distinct H-bond organizations may be observed for dendritic systems.

Despite a marked lack of long range ordering, short-range structures abound in the well-defined coordination shells of the constituent atoms, ions, or molecules in liquids and glasses.<sup>51</sup> This ordering is more pronounced in liquids that exhibit particularly strong intermolecular forces or favorable molecular shapes such as the most abundant molecule on earth's surface, water.<sup>52</sup> Interacting via H-bonds in which the partial positive charged hydrogen atoms of one molecule bond to the partial negative charged oxygen atom of another, water exhibits unique tetrahedral or string-like ordering even in the liquid state, where the unusual physical properties of water are caused by this pervasive H-bond network.<sup>53-56</sup> Pronounced structures have been seen in liquid ammonia and hydrogen fluoride as well where H-bonding serves as a bolstering force by stabilizing linear clusters of these molecules.<sup>57-59</sup> Whether a similar network of this type may be observed for dendritic polymers will be assessed in this dissertation.

### Molecular Dynamics Simulations

While experimental techniques continue to provide vital information regarding the structural characteristics of dendritic polymers, results from these are not always easily interpreted at the level of individual molecules or in relation to specific interactions associated to H-bonding. By synergistically complementing experimentally observed phenomena with computer simulations, detailed information regarding molecular-scale structural organizations may be obtained. By the use of a classical potential function, larger systems may be simulated through molecular dynamics (MD) methods. The potential function describes the terms by which the particles in the simulation will

interact. In MD simulations two assumptions are made which allow the calculation of physical properties on a feasible time-scale: (1) electrons may be treated separately if their dynamics are fast enough to be considered to react instantaneously to the motion of their nuclei, ‘the Born-Oppenheimer approximation’ and (2) atomic nuclei can be treated as a point particles that follow Newtonian dynamics.<sup>60</sup> Furthermore, through the stepwise integration of Newton’s second equation of motion for  $N$  interacting particles over a period of time, the force exerted on a particle,  $F = ma$ , can be computed directly from the derivative of the potential energy ( $V$ ) with respect to the change in position,  $r_i$ , of particle  $i$  as a function of time,  $t$

$$-(\partial V / \partial r_i) = m_i (\partial^2 r_i / \partial t^2) \quad (2)$$

where  $m_i$  is the mass of particle  $i$ , and the potential energy surface for a set of atoms is defined by interatomic potentials or “forcefields.” Equation 1 is numerically solved by the finite-difference method, where given the initial coordinates, velocities, and other dynamic information at time  $t$ , the positions and velocities at time  $t + \Delta t$ , where  $\Delta t$  is the time-step, are calculated.<sup>60, 61</sup>

Atomistic type MD simulations are limited in the range of system size and time-scale they can reach, where the upper limit is approximately up to 1000 nm and 100 ns respectively.<sup>62, 63</sup> Therefore, MD simulations are ideal for systems such as dendritic polymers, which have relative lower molecular weights, a lack of chain entanglements, and bond relaxation times comparable to the simulation time-scale. Insight into the structure and dynamics of dendrimers and HBPs can be gained by atomistic MD simulations, where molecular-level phenomena can be visualized in detail as long as simulations are validated by successful comparisons to available experimental results.

Several perfect dendrimer systems and HBPs have been modeled atomistically,<sup>64-69</sup> however the majority of these studies have been focused on solution behavior. Recently, MD simulations of bis-MPA based HBPs specifically have been conducted by Tanis et al., to gain insight into the H-bond organization.<sup>68</sup> It was established that the most abundant type of H-bonding exists between the hydroxyl groups, and H-bonding can alter the dynamics of secondary relaxation processes. The organization and topology of the H-bonds in bis-MPA dendritic polymers have not been identified and many of their bulk structural properties have yet to be simulated.

#### Research Overview

Although a small body of research exists depicting the H-bond organization and structural ordering in bis-MPA dendritic systems,<sup>43, 70, 71</sup> this schematic can only be considered a rough abridgment. Very limited information is available on bulk volumetric properties, free volume behavior, and to some extent thermal behavior of bis-MPA dendritic polymers and it is not clear to what extent the properties of HBPs and dendritic polymers are different or similar in the bulk. Unique structural features such as a multitude of end-groups, core-shell architecture, high branching density, and globular macromolecular shape may amount to unique physical properties and H-bond organizations as compared to linear polymers. The purpose of this dissertation was to elucidate the H-bond organizations in relation to the bulk thermal and free volume properties of bis-MPA dendritic polymers, with an emphasis on developing a fundamental understanding of the extent to which HBPs of this type compare to perfect dendrimers. The following research objectives were utilized to accomplish the main goal.



*Research Objectives*

- R.O.1 Elucidate the topology of hydrogen bond organizations related to the bulk physical properties of bis-MPA dendrimers and HBPs.
- R.O.2 Identify the geometric arrangement of atoms and/or molecules, composing the H-bond driven structural order in HBPs specifically and identify the changes in the structural order upon annealing as a function of time and temperature.
- R.O.3 Establish a relationship between the volumetric and thermodynamic parameters of bis-MPA based HBPs and their structure and hydrogen bond organizations.
- R.O.4 Model bis-MPA dendrimers and HBPs in the bulk to visualize the globular shape, hydrogen bond organization, structural ordering, and PVT behavior.
- R.O.5 Evaluate the extent to which MD simulations can predict the bulk volumetric and thermodynamic properties of bis-MPA based dendrimers and HBPs.

All experimental work was conducted using the commercially available Boltorn<sup>®</sup> HBPs, abbreviated as HX0, where X denotes the pseudo-generation number. In addition to HX0 HBPs, throughout the text their perfect dendrimer analogous will be similarly designated as DX0. In Chapter II generations two and four of both the bis-MPA/PP50 core dendrimers and HBPs were successfully simulated and the globular shape, and hydrogen bond organizations were analyzed (R.O.1, 4, and 5). By complementing an experimentally observed ordering phenomenon from X-ray diffraction with MD simulations, hydrogen bond assisted ‘chain-like’ clusters were identified as the main hydrogen bond organization for both dendrimers and HBPs in the bulk state (R.O.1). In Chapter III, a model was proposed to identify the arrangement of atoms and molecules which are involved in the hydrogen bond mediated structural ordering phenomenon of

HBP (R.O.2). The PVT behavior of the second and fourth pseudo-generation bis-MPA HBPs was experimentally probed and relevant volumetric and thermodynamic parameters were determined, and compared with simulated free and occupied volume in Chapter IV (R.O.3, 4, and 5).

#### References

1. Tomalia, D. A., Dendrimer Molecules. *Sci. Am.* 1995, pp 62-66.
2. Tomalia, D. A.; Fréchet, J. M. J. Discovery of dendrimers and dendritic polymers: A brief historical perspective\*. *J. Polym. Sci., Part A: Polym. Chem.* **2002**, *40*, 2719-2728.
3. Hawker, C. J.; Fréchet, J. M. J. Preparation of polymers with controlled molecular architecture. A new convergent approach to dendritic macromolecules. *J. Am. Chem. Soc.* **1990**, *112*, 7638-7647.
4. Hawker, C.; Fréchet, J. M. J. A new convergent approach to monodisperse dendritic macromolecules. *J. Chem. Soc., Chem. Commun.* **1990**, 1010-1013.
5. Liu, M.; Fréchet, J. M. J. Designing dendrimers for drug delivery. *Pharm. Sci. Tech. To.* **1999**, *2*, 393-401.
6. Esfand, R.; Tomalia, D. A. Poly(amidoamine) (PAMAM) dendrimers: from biomimicry to drug delivery and biomedical applications. *Drug Disc. To.* **2001**, *6*, 427-436.
7. Gilat, S. L.; Adronov, A.; Fréchet, J. M. J. Light Harvesting and Energy Transfer in Novel Convergently Constructed Dendrimers. *Angew. Chem. Int. Ed.* **1999**, *38*, 1422-1427.

8. Balzani, V.; Ceroni, P.; Maestri, M.; Vicinelli, V. Light-harvesting dendrimers. *Curr. Opin. Chem. Biol.* **2003**, *7*, 657-665.
9. Bosman, A. W.; Janssen, H. M.; Meijer, E. W. About Dendrimers: Structure, Physical Properties, and Applications. *Chem. Rev.* **1999**, *99*, 1665-1688.
10. Fréchet, J. M. J.; Hawker, C. J.; Gitsov, I.; Leon, J. W. Dendrimers and Hyperbranched Polymers: Two Families of Three-Dimensional Macromolecules with Similar but Clearly Distinct Properties. *J. Macromol. Sci., Part A* **1996**, *33*, 1399-1425.
11. Mintzer, M. A.; Grinstaff, M. W. Biomedical applications of dendrimers: a tutorial. *Chem. Soc. Rev.* **2011**, *40*, 173-190.
12. Abbasi, E.; Aval, S. F.; Akbarzadeh, A.; Milani, M.; Nasrabadi, H. T.; Joo, S. W.; Hanifehpour, Y.; Nejati-Koshki, K.; Pashaei-Asl, R. Dendrimers: synthesis, applications, and properties. *Nanoscale Res. Lett.* **2014**, *9*, 247-247.
13. Yates, C. R.; Hayes, W. Synthesis and applications of hyperbranched polymers. *Eur. Polym. J.* **2004**, *40*, 1257-1281.
14. Huang, Y.; Wang, D.; Zhu, X.; Yan, D.; Chen, R. Synthesis and therapeutic applications of biocompatible or biodegradable hyperbranched polymers. *Polym. Chem.* **2015**, *6*, 2794-2812.
15. Zheng, Y.; Li, S.; Weng, Z.; Gao, C. Hyperbranched polymers: advances from synthesis to applications. *Chem. Soc. Rev.* **2015**, *44*, 4091-4130.
16. Hawker, C. J.; Lee, R.; Frechet, J. M. J. One-step synthesis of hyperbranched dendritic polyesters. *J. Am. Chem. Soc.* **1991**, *113*, 4583-4588.

17. Hölter, D.; Burgath, A.; Frey, H. Degree of branching in hyperbranched polymers. *Acta Polym.* **1997**, *48*, 30-35.
18. Mourey, T. H.; Turner, S. R.; Rubinstein, M.; Frechet, J. M. J.; Hawker, C. J.; Wooley, K. L. Unique behavior of dendritic macromolecules: intrinsic viscosity of polyether dendrimers. *Macromolecules* **1992**, *25*, 2401-2406.
19. Turner, S. R.; Voit, B. I.; Mourey, T. H. All-aromatic hyperbranched polyesters with phenol and acetate end groups: synthesis and characterization. *Macromolecules* **1993**, *26*, 4617-4623.
20. Hay, G.; Mackay, M. E.; Hawker, C. J. Thermodynamic properties of dendrimers compared with linear polymers: General observations. *J. Polym. Sci., Part B: Polym. Phys.* **2001**, *39*, 1766-1777.
21. Simha, R.; Utracki, L. A. PVT properties of linear and dendritic polymers. *J. Polym. Sci., Part B: Polym. Phys.* **2010**, *48*, 322-332.
22. Žagar, E.; Žigon, M. Aliphatic hyperbranched polyesters based on 2,2-bis(methylol)propionic acid—Determination of structure, solution and bulk properties. *Prog. Polym. Sci.* **2011**, *36*, 53-88.
23. Kim, Y. H.; Webster, O. W. Hyperbranched polyphenylenes. *Macromolecules* **1992**, *25*, 5561-5572.
24. Hawker, C. J.; Farrington, P. J.; Mackay, M. E.; Wooley, K. L.; Frechet, J. M. J. Molecular Ball Bearings: The Unusual Melt Viscosity Behavior of Dendritic Macromolecules. *J. Am. Chem. Soc.* **1995**, *117*, 4409-4410.
25. Hult, A.; Johansson, M.; Malmström, E. Hyperbranched Polymers. *Adv. Polym. Sci.* **1999**, *143*, 1-34.

26. Wooley, K. L.; Hawker, C. J.; Pochan, J. M.; Frechet, J. M. J. Physical properties of dendritic macromolecules: a study of glass transition temperature. *Macromolecules* **1993**, *26*, 1514-1519.
27. Malmström, E.; Johansson, M.; Hult, A. The effect of terminal alkyl chains on hyperbranched polyesters based on 2,2-bis(hydroxymethyl)propionic acid. *Macromol. Chem. Phys.* **1996**, *197*, 3199-3207.
28. Carlmark, A.; Malmstrom, E.; Malkoch, M. Dendritic architectures based on bis-MPA: functional polymeric scaffolds for application-driven research. *Chem. Soc. Rev.* **2013**, *42*, 5858-5879.
29. Pettersson, B., *Properties and Applications of Boltorn, Dendritic Polymers*. Boltorn: 2001.
30. Zhang, X. Modifications and applications of hyperbranched aliphatic polyesters based on dimethylolpropionic acid. *Polym. Int.* **2011**, *60*, 153-166.
31. Ihre, H.; Hult, A.; Fréchet, J. M. J.; Gitsov, I. Double-Stage Convergent Approach for the Synthesis of Functionalized Dendritic Aliphatic Polyesters Based on 2,2-Bis(hydroxymethyl)propionic Acid. *Macromolecules* **1998**, *31*, 4061-4068.
32. Ihre, H.; Padilla De Jesús, O. L.; Fréchet, J. M. J. Fast and Convenient Divergent Synthesis of Aliphatic Ester Dendrimers by Anhydride Coupling. *J. Am. Chem. Soc.* **2001**, *123*, 5908-5917.
33. Malmstrom, E.; Johansson, M.; Hult, A. Hyperbranched Aliphatic Polyesters. *Macromolecules* **1995**, *28*, 1698-1703.

34. Malmström, E.; Hult, A. Kinetics of Formation of Hyperbranched Polyesters Based on 2,2-Bis(methylol)propionic Acid. *Macromolecules* **1996**, *29*, 1222-1228.
35. Lange, J.; Stenroos, E.; Johansson, M.; Malmström, E. Barrier coatings for flexible packaging based on hyperbranched resins. *Polymer* **2001**, *42*, 7403-7410.
36. Miao, H.; Cheng, L.; Shi, W. Fluorinated hyperbranched polyester acrylate used as an additive for UV curing coatings. *Prog. Org. Coat.* **2009**, *65*, 71-76.
37. Shi, Z.; Zhou, Y.; Yan, D. Facile Fabrication of pH-Responsive and Size-Controllable Polymer Vesicles From a Commercially Available Hyperbranched Polyester. *Macromol. Rapid Commun.* **2008**, *29*, 412-418.
38. Zeng, X.; Zhang, Y.; Nyström, A. M. Endocytic Uptake and Intracellular Trafficking of Bis-MPA-Based Hyperbranched Copolymer Micelles in Breast Cancer Cells. *Biomacromolecules* **2012**, *13*, 3814-3822.
39. Zeng, X.; Zhang, Y.; Wu, Z.; Lundberg, P.; Malkoch, M.; Nyström, A. M. Hyperbranched copolymer micelles as delivery vehicles of doxorubicin in breast cancer cells. *J. Polym. Sci., Part A: Polym. Chem.* **2012**, *50*, 280-288.
40. Paleos, C. M.; Tsiourvas, D.; Sideratou, Z.; Tziveleka, L. Multifunctional Dendritic Drug Delivery Systems: Design, Synthesis, Controlled and Triggered Release. *Curr. Top. Med. Chem.* **2008**, *8*, 1204-1224.
41. Plummer, C. J. G.; Garamszegi, L.; Leterrier, Y.; Rodlert, M.; Månson, J.-A. E. Hyperbranched Polymer Layered Silicate Nanocomposites. *Chem. Mater.* **2002**, *14*, 486-488.

42. Decker, J. J.; Chvalun, S. N.; Nazarenko, S. Intercalation behavior of hydroxylated dendritic polyesters in polymer clay nanocomposites prepared from aqueous solution. *Polymer* **2011**, *52*, 3943-3955.
43. Žagar, E.; Huskić, M.; Grdadolnik, J.; Žigon, M.; Zupančič-Valant, A. Effect of Annealing on the Rheological and Thermal Properties of Aliphatic Hyperbranched Polyester Based on 2,2-Bis(methylol)propionic Acid. *Macromolecules* **2005**, *38*, 3933-3942.
44. Montarnal, D.; Cordier, P.; Soulie-Ziakovic, C.; Tournilhac, F.; Leibler, L. Synthesis of Self-Healing Supramolecular Rubbers from Fatty Acid Derivatives, DiethyleneTriamine, and Urea. *J. Polym. Sci., Part A: Polym. Chem.* **2008**, *46*, 7925-7936.
45. Montarnal, D.; Tournilhac, F.; Hidalgo, M.; Couturier, J.-L.; Leibler, L. Versatile One-Pot Synthesis of Supramolecular Plastics and Self-Healing Rubbers. *J. Am. Chem. Soc.* **2009**, *131*, 7966-7967.
46. Cordier, P.; Tournilhac, F.; Soulie-Ziakovic, C.; Leibler, L. Self-healing and thermoreversible rubber from supramolecular assembly. *Nature* **2008**, *451*, 977-980.
47. Painter, P. C.; Graf, J. F.; Coleman, M. M. Effect of hydrogen bonding on the enthalpy of mixing and the composition dependence of the glass transition temperature in polymer blends. *Macromolecules* **1991**, *24*, 5630-5638.
48. Painter, P. C.; Pruthitkul, R.; Coleman, M. M.; Tan Beck, N. An infrared spectroscopic study of a hyperbranched, dendrimer-like, polyester and its blends with poly(4-vinyl phenol). *Macromol. Symp.* **1999**, *141*, 57-67.

49. Desiraju, G. R. A Bond by Any Other Name. *Angew. Chem. Int. Ed.* **2011**, *50*, 52-59.
50. Jeffrey, G. A., *An Introduction to Hydrogen Bonding*. Oxford University Press, Inc.: New York, 1997.
51. Benson, S. W.; Siebert, E. D. A simple two-structure model for liquid water. *J. Am. Chem. Soc.* **1992**, *114*, 4269-4276.
52. Hayes, R.; Warr, G. G.; Atkin, R. Structure and Nanostructure in Ionic Liquids. *Chem. Rev.* **2015**, *115*, 6357-6426.
53. Narten, A. H.; Thiessen, W. E.; Blum, L. Atom Pair Distribution Functions of Liquid Water at 25°C from Neutron Diffraction. *Science* **1982**, *217*, 1033-1034.
54. Head-Gordon, T.; Johnson, M. E. Tetrahedral structure or chains for liquid water. *Proc. Natl. Acad. Sci.* **2006**, *103*, 7973-7977.
55. Head-Gordon, T.; Hura, G. Water Structure from Scattering Experiments and Simulation. *Chem. Rev.* **2002**, *102*, 2651-2670.
56. Ball, P. Water: Water - an enduring mystery. *Nature* **2008**, *452*, 291-292.
57. Sarkar, S.; Karmakar, A. K.; Joarder, R. N. Molecular Clusters and Correlations in Liquid Ammonia. *J. Phys. Chem. A* **1997**, *101*, 3702-3706.
58. McLain, S. E.; Benmore, C. J.; Siewenie, J. E.; Urquidi, J.; Turner, J. F. C. On the Structure of Liquid Hydrogen Fluoride. *Angew. Chem. Int. Ed.* **2004**, *43*, 1952-1955.
59. Röthlisberger, U.; Parrinello, M. Ab initio molecular dynamics simulation of liquid hydrogen fluoride. *J. Chem. Phys.* **1997**, *106*, 4658-4664.



60. Baianu, I. C., *Molecular Modeling and Dynamics: Modeling Methods, Molecular Dynamics, Computational Models and Computer Simulations of Molecular Systems*. Free Software Foundation, Inc.: Boston, MA, 2002.
61. Tuckerman, M., Classical Mechanics. In *Statistical mechanics: theory and molecular simulation*, Oxford University Press: New York, 2010; pp 2-13.
62. Lee, H.; Larson, R. G. Molecular Dynamics Simulations of PAMAM Dendrimer-Induced Pore Formation in DPPC Bilayers with a Coarse-Grained Model. *J. Phys. Chem. B* **2006**, *110*, 18204-18211.
63. Makov, G.; Gattinoni, C.; Vita, A. D. Ab initio based multiscale modelling for materials science. *Modell. Simul. Mater. Sci. Eng.* **2009**, *17*, 084008.
64. Gorman, C. B.; Smith, J. C. Effect of repeat unit flexibility on dendrimer conformation as studied by atomistic molecular dynamics simulations. *Polymer* **2000**, *41*, 675-683.
65. Lee, I.; Athey, B. D.; Wetzel, A. W.; Meixner, W.; Baker, J. R. Structural Molecular Dynamics Studies on Polyamidoamine Dendrimers for a Therapeutic Application: Effects of pH and Generation. *Macromolecules* **2002**, *35*, 4510-4520.
66. Pricl, S.; Fermeglia, M.; Ferrone, M.; Asquini, A. Scaling properties in the molecular structure of three-dimensional, nanosized phenylene-based dendrimers as studied by atomistic molecular dynamics simulations. *Carbon* **2003**, *41*, 2269-2283.

67. Jena, K. K.; Raju, K. V. S. N.; Prathab, B.; Aminabhavi, T. M. Hyperbranched Polyesters: Synthesis, Characterization, and Molecular Simulations. *J. Phys. Chem. B* **2007**, *111*, 8801-8811.
68. Tanis, I.; Karatasos, K. Local Dynamics and Hydrogen Bonding in Hyperbranched Aliphatic Polyesters. *Macromolecules* **2009**, *42*, 9581-9591.
69. Tanis, I.; Tragoudaras, D.; Karatasos, K.; Anastasiadis, S. H. Molecular Dynamics Simulations of a Hyperbranched Poly(ester amide): Statics, Dynamics, and Hydrogen Bonding. *J. Phys. Chem. B* **2009**, *113*, 5356-5368.
70. Žagar, E.; Grdadolnik, J. An infrared spectroscopic study of H-bond network in hyperbranched polyester polyol. *J. Mol. Struct.* **2003**, *658*, 143-152.
71. Žagar, E.; Huskić, M.; Žigon, M. Structure-to-Properties Relationship of Aliphatic Hyperbranched Polyesters. *Macromol. Chem. Phys.* **2007**, *208*, 1379-1387.

CHAPTER II  
HYDROGEN BOND ASSISTED CHAIN-LIKE CLUSTERS IN BIS-MPA  
DENDRIMERS AND HYPERBRANCHED POLYMERS

Abstract

Given the high concentration and unique spatial orientation of end-groups, distinct hydrogen bond (H-bond) organizations may be observed for dendritic systems. Bulk studies of this kind however are lacking. In this chapter, ‘chain-like’ clusters of H-bonded O-H $\cdots$ O groups were identified in the second (D20) and fourth (D40) generation bis-MPA/PP50 dendrimers, and analogous HBPs, H20 and H40, respectively, as a potential H-bond topology which may control the physical properties of these 3-D globular polymers. This work highlights a major similarity between dendrimers and HBPs despite their different branching structure. Structural order was studied using X-ray diffraction, where the reflection at  $2\theta \approx 30^\circ$  was reminiscent of the main reflection in the X-ray pattern of liquid water, which represents inter-oxygen atom (O-O) correlations within the H-bonded clusters of water’s H-bond network.<sup>1</sup> Boltorn H40 was esterified to monitor the effect of H-bonding between hydroxyl groups on the X-ray pattern. The dendrimers and analogous HBPs were simulated, and the bulk structure was analyzed. Simulated X-ray patterns were generated for the hydroxylated dendrimers and HBPs, as well as for a fully esterified dendrimer, confirming that the origin of the reflection at  $2\theta \approx 30^\circ$  was related to H-bond interactions between the hydroxyl end-groups. A statistical hydrogen bond analysis of the simulated structures of D20 and D40 as well as H20 and H40 was utilized to characterize the number and length of the ‘chain-like’ clusters. In this

way, the role of key structural parameters (generation number and degree of branching) in the formation of these clusters was revealed.

### Introduction

Due to the multitude of hydroxyl end-groups and interior carbonyl, ester, and ether moieties, H-bond interactions are abundant in bis-MPA based dendritic systems. Although H-bond interactions have been shown to play a key role in determining the bulk physical properties of dendrimers and HBPs,<sup>2,3</sup> organizations related to H-bonding have not been investigated thoroughly. Recently, X-ray diffraction experiments of bis-MPA dendritic polymers have revealed unique hydrogen bond-mediated ordering phenomena in these relatively amorphous polymers.<sup>4-6</sup> The wide-angle X-ray diffraction (WAXD) patterns of Boltorn HBPs are quite complex where in addition to the peculiarly shaped main peak at  $2\theta \approx 17^\circ$ , all studied pseudo-generations (2-5) displayed two additional smaller and broader peaks at  $2\theta \approx 30^\circ$  and  $42^\circ$ .<sup>6</sup> Representative WAXD patterns of H20 and H40 are shown in Figure 4. The reflection at  $2\theta \approx 17^\circ$  was identified as the amorphous halo, and the peculiarly narrow shape of this peak was attributed to an ordering phenomenon related to the H-bonding of linear chain segments, thus being unique to irregular hyperbranched systems only.<sup>4,5,7</sup> In a WAXD study conducted on a fourth generation bis-MPA HBP and its analogous dendrimer by Žagar et al., the fourth generation bis-MPA dendrimer proved insensitive to annealing treatments as it showed no change in the shape of its amorphous halo peak at  $2\theta \approx 17^\circ$ .<sup>4</sup> In contrast, the amorphous halo for Boltorn<sup>®</sup> HBPs exhibited a noticeable sharpening, attributed to formation of a H-bond network and enhancing of the structural ordering upon annealing. The specific details of this ordering phenomenon have not been described though.

Chapter III of this dissertation will address the structural origin of the sharp nature of the amorphous halo peak. The low intensity and broad peak at  $2\theta \approx 42^\circ$  from the X-ray patterns was only briefly mentioned and assigned, without evidence, to a “weak” amorphous reflection.<sup>6</sup> The peak at  $2\theta \approx 30^\circ$  however has not been discussed at all. Since the reflection at  $2\theta \approx 30^\circ$  was also present in the WAXD pattern of the bis-MPA fourth generation dendrimer,<sup>4</sup> understanding the structural origin of this peak may shed light on the similarities between HBPs and dendrimers.

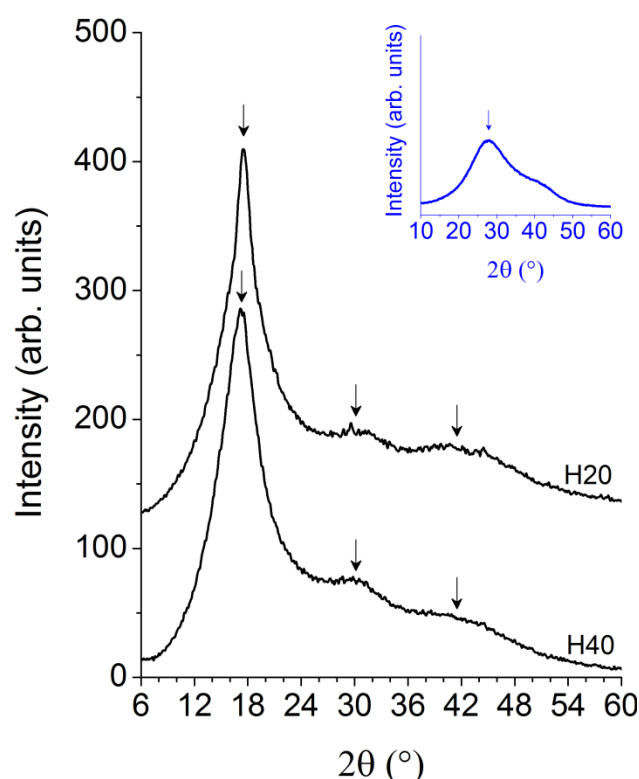


*Figure 4.* Wide-angle X-ray diffraction (WAXD) patterns of Boltorn H20 and H40. The inset displays the WAXD pattern for D.I. water. The pattern for H20 was shifted vertically by 100 units for clarity.

A clue that these dendritic polymers may form interesting H-bond organizations was provided by the observation that the X-ray patterns of the bis-MPA dendritic polymers displayed remarkable similarities with small molecule H-bond formers, such as liquid water. The 3-D hydrogen bond network of water is composed of tetrahedral

clusters of hydrogen bonded oxygen and hydrogen atoms.<sup>1, 8, 9</sup> The distance between the oxygen atoms in the clusters gives rise to a broad peak in the X-ray scattering pattern of water, centered at  $2\theta \approx 28^\circ$  corresponding to a d-spacing of  $\sim 0.31 \text{ nm}^1$  (inset in Figure 4). Furthermore, the unusual properties of water in the liquid state are attributed to the formation of these tetrahedral clusters. Because the d-spacing, 0.30 nm, and broad shape of the reflection at  $2\theta \approx 30^\circ$  in the WAXD patterns of the bis-MPA dendritic polymers was similar to that of water, it was hypothesized that the structural origin of the reflection at  $2\theta \approx 30^\circ$  may also be related to hydrogen bonded clusters of O-H $\cdots$ O groups, and that these clusters may encompass a considerable portion of the bulk of the polymer.

## Experimental

### *Materials and Sample Preparation*

The Boltorn<sup>®</sup> second, H20, and fourth, H40, pseudo-generation bis-MPA based hyperbranched polyesters were kindly donated by Perstorp Polyols Inc., Sweden. In abbreviation HX0, X denotes the pseudo-generation number. In addition to HX0 HBPs, throughout the text their perfect dendrimer analogous will be similarly designated as DX0. The theoretical molecular weights of D20 and D40 are 1749 and 7323 g/mol, respectively. The molecular weight of H20 and H40 determined by SEC and as reported by Perstorp, are 2100 and 5100 g/mol, respectively. Perstorp reported 0.45 and 0.44 for the degree of branching (DB) of H20 and H40 which have been calculated from the corresponding NMR spectra according to the Fréchet method.<sup>11</sup> Unless otherwise noted, all other materials were obtained from Sigma Aldrich. All received materials were dried under vacuum and stored in a desiccator prior to use.

The fourth pseudo-generation hydroxylated hyperbranched polyester, H40, was functionalized (esterified) with acetyl chloride,  $\text{COCH}_3\text{Cl}$ , according to the method described elsewhere.<sup>12</sup> Acetylation of H40 was carried out to 10, 25, 50, 75, and 100%. H40 (5.0 g, 0.98 mmol) was dissolved in 40 ml of acetone in a 500 ml round bottom flask. Triethylamine (8.0 g, 79.1 mmol) and 4-(dimethylamino)pyridine (0.30, 2.4 mmol) were added. The flask was cooled in an ice-bath. Acetyl chloride (0.39 g, 5 mmol; 0.94 g, 12 mmol; 1.88 g, 24 mmol; 2.83 g, 36 mmol; according to 10%, 25%, 50%, and 75% esterification respectively) was diluted with 50 ml acetone and added dropwise over 3 h. The ice-bath was continuously refreshed during the addition. The organic phase was extracted twice with  $\text{NaHCO}_3$  (10%), twice with HCl (2 M), and dried with  $\text{MgSO}_4$ . The final product, designated thereafter as H40-CH<sub>3</sub>, was obtained after evaporation of the solvent. With increasing degree of esterification, the product became more yellow in color, and less solid-like, where at 100% esterification the product resembled a highly viscous liquid. The structure of each H40-derivative was analyzed by WAXD, FTIR spectroscopy, and differential scanning calorimetry (DSC).

The Carver Melt Press was used to prepare thin sheets of H20 and H40. Pellets of H20 and H40 were dried under vacuum for at least 24 hours at 80°C prior to compression molding. The appropriate amount of each polymer was placed in a mold of approximately 1 mm thickness, which was sandwiched between two Teflon sheets, with two metal platens on each side. The platens were placed in the press at 120°C and held for about 10 min without pressure. Then the pressure was first increased to 2,500 psi, followed by a release of pressure to remove air bubbles, then increased to 5,000 psi, released again, and finally molded at 7,500 psi. The mold was cooled at a rate of approximately 10°C per

minute by flowing water through the press platens. The molded samples were then removed and placed in a desiccant chamber until further testing.

WAXD spectra were collected on a Rigaku Ultima III diffractometer ( $\text{CuK}\alpha$  radiation,  $\lambda = 1.542\text{\AA}$ ) at room temperature using Bragg-Brentano parafocusing geometry (reflection mode XRD). X-ray information was obtained from samples powdered in an analytical mill. Powdered samples were placed onto the sample stage and examined at angles from  $2\theta=1-60^\circ$  at a step rate of  $1^\circ/\text{s}$ .

Thermal behavior was investigated by differential scanning calorimetry (DSC) using a TA Instruments DSC Q-100. The calibration was carried out using indium and sapphire standards. Samples were first heated to  $200^\circ\text{C}$  at a rate of  $10^\circ\text{C}/\text{min}$  to erase thermal history, quenched to  $-50^\circ\text{C}$  at  $30^\circ\text{C}/\text{min}$ , and then heated to  $200^\circ\text{C}$  at  $10^\circ\text{C}/\text{min}$ . The final scan was taken as the second heating run.

FTIR spectra were recorded at a resolution of  $4\text{ cm}^{-1}$  using a Bruker Tensor 37 FTIR spectrometer using the KBr pellet method. Spectra were collected in the mid-range.

The density of H20 and H40 were determined using a toluene/carbon tetrachloride solution based density gradient column prepared according to ASTM-D 1505 (Method B). It was confirmed that the selected combination of solvents does not lead to measurable swelling of hyperbranched polyol samples. The column was calibrated with glass floats of known density. Experimental error of density measurements did not exceed  $0.0005\text{ g}/\text{cm}^{-3}$ . Several small pieces were cut from each film or thin sheet, and the final density was taken as the average of five measurements. The density of the 100% acetylated H40 product, 100% H40-CH<sub>3</sub>, was determined using a pycnometer and was therefore only accurate to the first decimal place. The material was heated to  $100^\circ\text{C}$ ,



poured into the pycnometer, and the weight of the added product was recorded. The material was allowed to cool to room temperature over 10 minutes and then D.I. water was added to the pycnometer till it was full. Water was chosen as the filling solvent since it was immiscible with the product. The weight of the amount of water added was recorded. The density of the acetylated material was back-calculated.

The pressure-volume-temperature (PVT) measurements were conducted by a fully automated Gnomix-PVT-apparatus (Boulder, Col. USA) with mercury employed as a confining fluid. Specific volumes were recorded with accuracy  $\pm 0.002 \text{ cm}^3/\text{g}$ . All reported here PVT data were collected in isothermal mode. The pressure at each selected temperature was increased incrementally using 10 MPa steps within the range 10-160 MPa. Volume thermal expansion behavior, V-T, at atmospheric pressure was generated via extrapolation of PVT data obtained at elevated pressures by fitting data to Tait equation of state<sup>13</sup>

$$v(P, T)/v(0, T) = 1 - C \ln(1 + P/b(T)) \quad (3)$$

where  $b(T) = b_1 \exp(-b_2 T)$ ,  $v$  is the molar volume as a function of pressure ( $P$ ) along an isotherm (given by the temperature,  $T$ ) and  $v(0, T)$  is the molar volume for the isotherm at zero (ambient) pressure. The three parameters for this model are  $C$ ,  $b_1$ , and  $b_2$ . The Tait equation parameters were determined by a fit to the volume data along an isotherm for different pressures. This routine is directly built in to Gnomix-PVT-apparatus software.

#### *Molecular Dynamics (MD) Simulations*

Five bis-MPA dendritic systems were modeled: (1) second generation perfect dendrimer, 'D20'; (2) fourth generation perfect dendrimer, 'D40'; (3) second generation

hyperbranched polymer, 'H20'; (4) fourth generation hyperbranched polymer, 'H40'; and (5) 100% acetylated fourth generation perfect dendrimer, 'D40-CH3.' All computational results were obtained using software programs from Accelrys Software, Inc., San Diego, unless otherwise stated. The Amorphous Cell module was used to construct an initial amorphous packing structure of 50 molecules of D20, 12 molecules of D40, 50 molecules of H20, 12 molecules of H40, and 9 molecules of D40-CH3. The chemical structures of D20, D40, and D40-CH3 are shown in Figure 5. In order to model H20 and H40, five different bis-MPA based HBP isomeric structures with a PP50 core were drawn, each with Fréchet DB=0.44 (D=0.100; L=0.565; T=0.335) for H20 and DB=0.45 (D=0.165; L=0.570; T=0.265)<sup>6</sup> for H40. The molecular weight of each configuration was that corresponding to the theoretical molecular weight of the perfect dendrimer analogue, 1750 and 7323 g/mol for H20 and H40 respectively (Figures 6 and 7). The amorphous cell of H20 was loaded with 10 molecules of each configuration from Figure 8. The amorphous cell of H40 was loaded with 3 molecules of configurations 'a' and 'b' and 2 molecules of configurations 'c', 'd', and 'e' from Figure 7. The number of molecules in each amorphous cell for D20, D40, H20, and H40 was chosen to closely match the total number of oxygen atoms (2450 for D20 and H20, and 2316 for D40 and H40) and hydroxyl hydrogen atoms (800 for D20 and H20, and 768 for D40 and H40) in order to have comparable systems for the hydrogen bond analysis, described below.

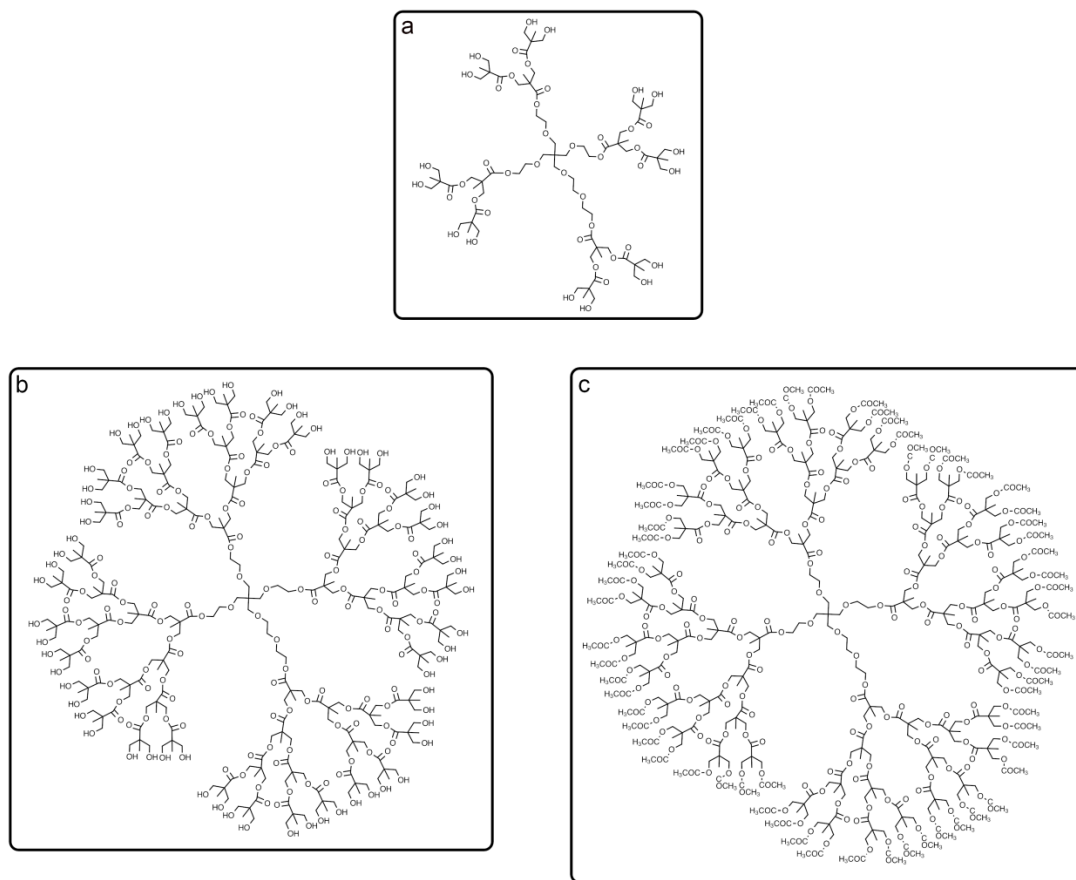
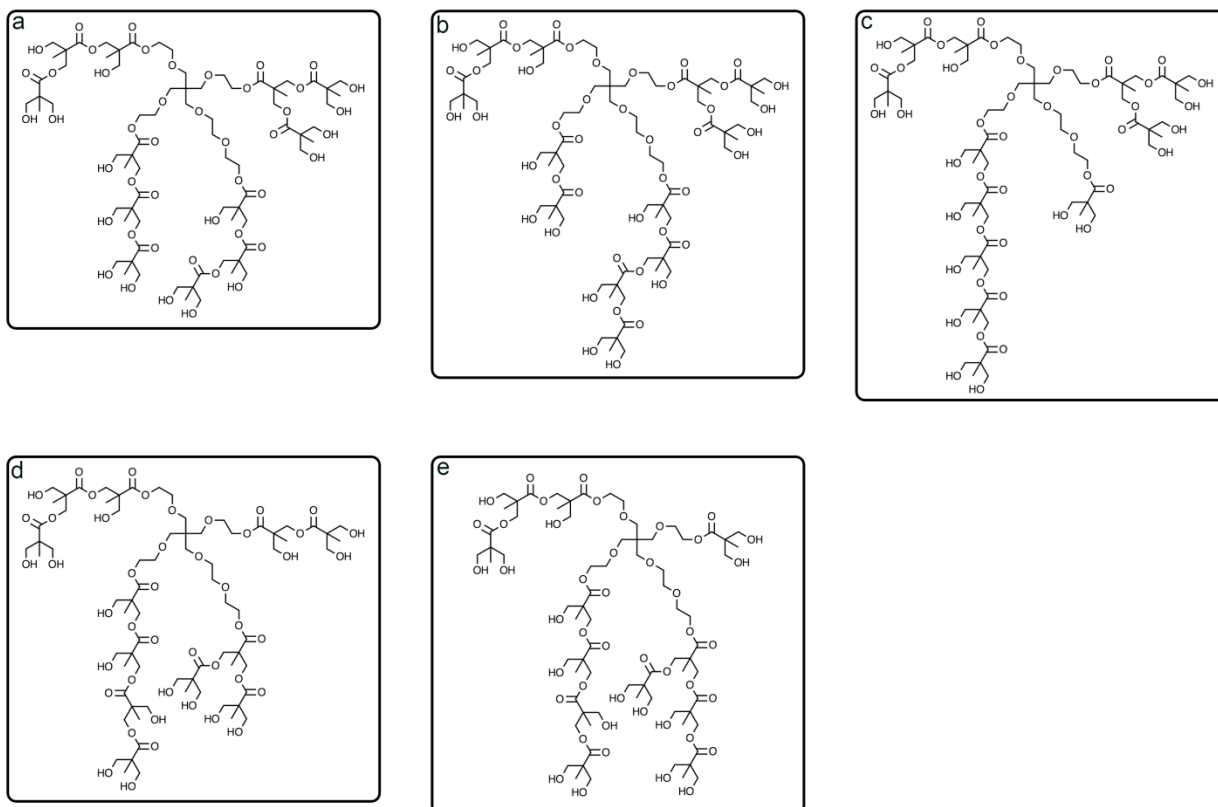
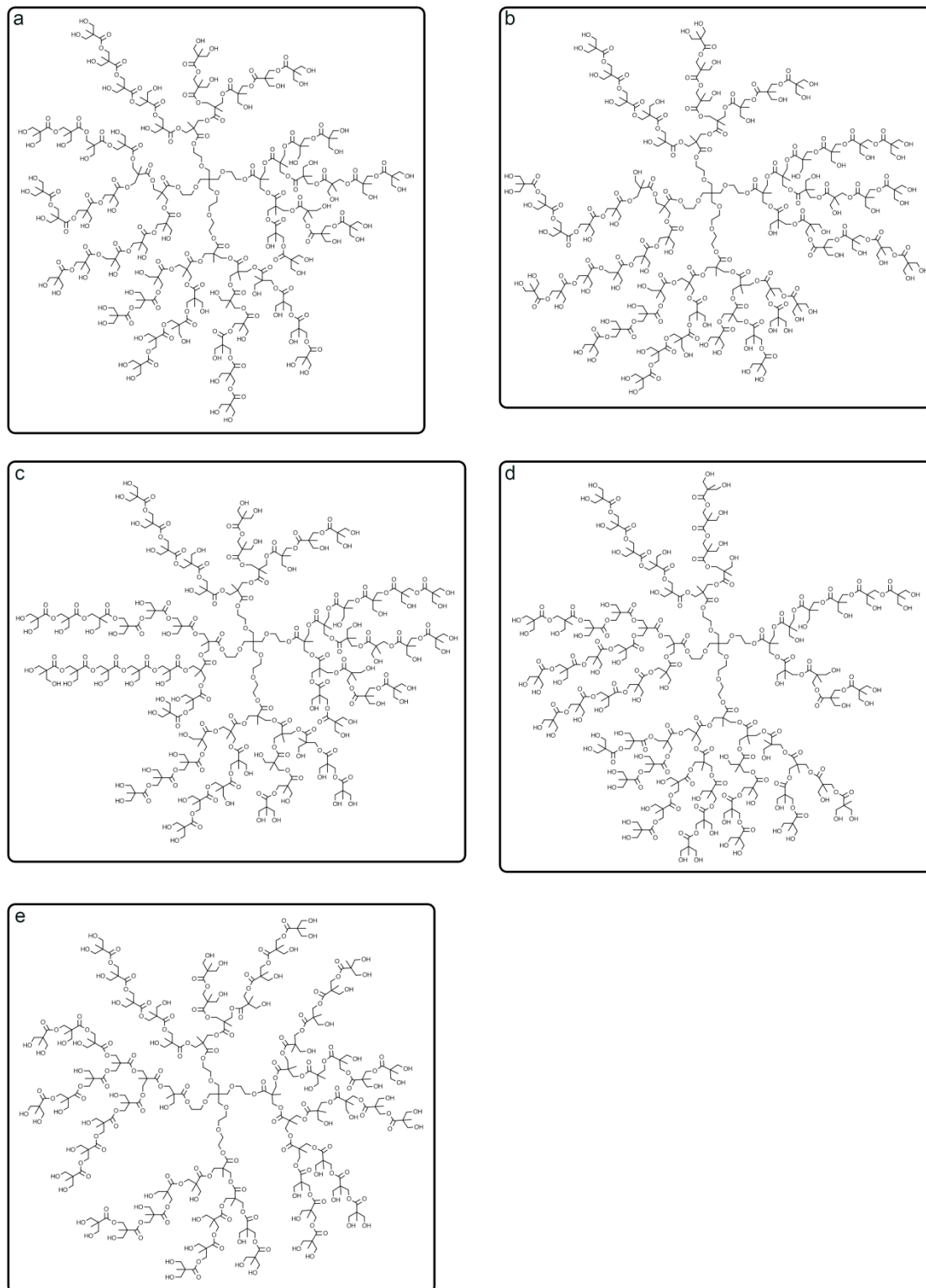


Figure 5. Chemical structures of the bis-MPA/PP50 dendrimers (a) D20, (b) D40, and (c) D40-CH<sub>3</sub>, which were used in molecular dynamics simulations.



*Figure 6.* Five configurational isomers of H20 used to construct the amorphous cell for the MD simulations. Each isomer had a molecular weight of 1749 g/mol and  $D = 0.100$ ;  $L = 0.565$ ;  $T = 0.335$ .<sup>5</sup>



*Figure 7.* Five configurational isomers of H40 used to construct the amorphous cell in MD simulations. Each isomer had a molecular weight of 7323 g/mol and  $D = 0.165$ ,  $L = 0.570$ ,  $T = 0.265$ .<sup>5</sup>

Each amorphous cell was constructed with a starting density of  $0.6 \text{ g/cm}^3$  whereby each system was atomistically modeled using the Discover program and the COMPASS forcefield. Each atom and molecule in the amorphous cell was assigned a unique name, e.g. O22, Molecule5, H5876. The Ewald summation method was used for all energy calculations, unless otherwise stated. Following minimization, MD runs of alternating NVT and NPT ensembles, between 650 K and 298 K and 1000-0.1 MPa were performed to obtain a relaxed amorphous cell at 298 K and 1 atm. The MD runs in the NVT ensembles utilized an atom-based summation method, with a cutoff distance of 9.5 Å, in order to reduce the simulation time. Utilizing the atom-based summation method for the NVT ensembles, as opposed to the Ewald method, was found to not change the final simulated density.

The final relaxed amorphous cells of D20, D40, H20, H40, and D40-CH<sub>3</sub> are shown in Figure 8. The computer-generated structures were validated through simulating the bulk properties, such as the density of the fully relaxed amorphous cell at ambient temperature and volume thermal expansion behavior, V-T, in the melt state at atmospheric pressure that were compared with the corresponding experimental data. The experimental densities were determined using a density column, and V-T data was obtained from PVT dilatometry, described above. While the final structures for D20, D40, H20, and H40 were validated through both the density of the amorphous cell and the melt state volumetric properties, the structure for D40-CH<sub>3</sub> was validated solely through the density since experimental V-T data for this particular system were not available. Moreover, because bulk experimental density and volume data were not available for the perfect dendrimers, the densities and volumes of these systems were

verified against the analogous HBPs. We were especially concerned with the agreement of the simulated H<sub>2</sub>O data with the experimental set because this was the only system of which we had both experimental and simulated data for.

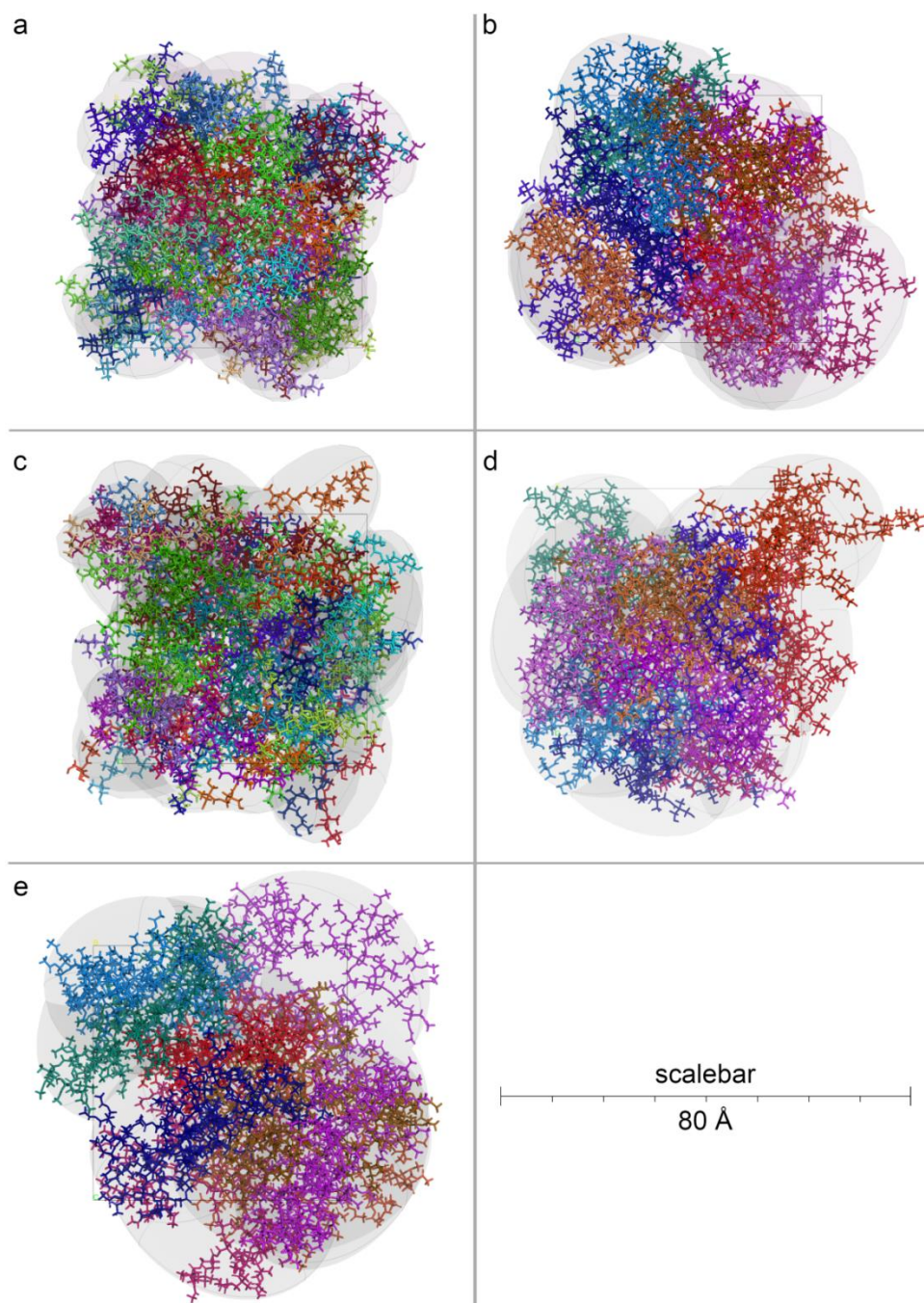


*Figure 8.* Final relaxed amorphous cells of (a) 50 molecules of D20, (b) 12 molecules of D40, (c) 50 molecules of H20, (d) 12 molecules of H40, and (e) 9 molecules of D40-CH<sub>3</sub>. Within each amorphous cell, different colors indicate different molecules, and each cell was on the same scale, indicated by the scale bar.

The density agreement was within  $\pm 6\%$  for each system as (1) the simulated density of D20,  $1.276 \text{ g/cm}^3$ , was only 0.6% lower than the experimental density of H20,



1.284 g/cm<sup>3</sup>, (2) the simulated density of D40, 1.314 g/cm<sup>3</sup>, was only 1.2% higher than the experimental density of H40, 1.299 g/cm<sup>3</sup>, (3) the simulated density of H20, 1.274 g/cm<sup>3</sup>, was only 0.8% lower than the experimental density of H20, (4) the simulated density of H40, 1.328 g/cm<sup>3</sup> was only 2.2% higher than the experimental density of H40, and (5) the simulated density of D40-CH<sub>3</sub>, 1.224 g/cm<sup>3</sup>, was 5.8% lower than the experimental density of 100% H40-CH<sub>3</sub>, 1.3 g/cm<sup>3</sup>. To simulate volume thermal expansion, after obtaining a relaxed structure at ambient temperature and pressure, NPT ensembles were performed for 0.2 ns at each temperature. The simulated V-T data for D20, D40, and H20 are plotted against the experimental V-T trends for Boltorn H20 and H40, in Figure 6. The simulated V-T data were in good agreement with the experimental trends. The melt thermal expansivity ( $E_m = (dV/dT)_P$ ) of simulated H20,  $(4.6 \pm 0.4) \cdot 10^{-4} \text{ cm}^3 \cdot \text{g}^{-1} \cdot \text{K}^{-1}$ , was only 3% greater than the experimental  $E_m$ ,  $(4.46 \pm 0.04) \cdot 10^{-4} \text{ cm}^3 \cdot \text{g}^{-1} \cdot \text{K}^{-1}$ , thus validating the structures obtained from our simulations.

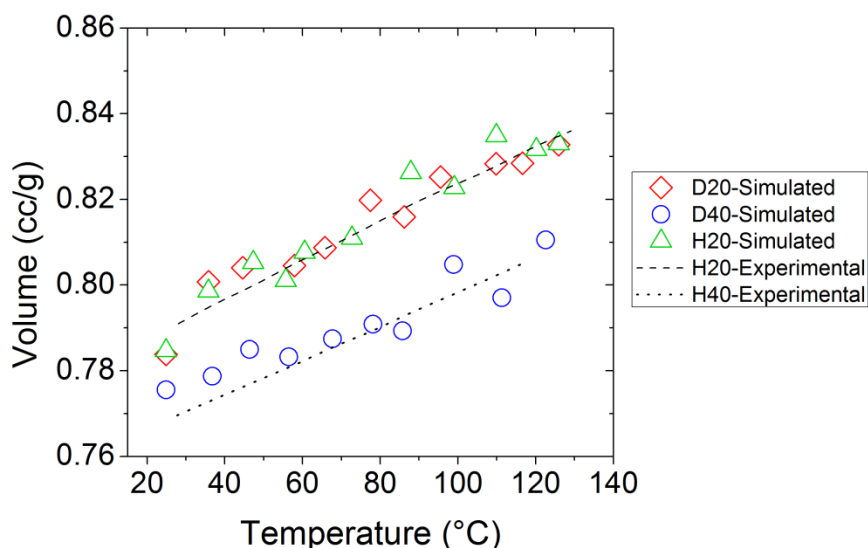


*Figure 9.* Simulated volume-temperature (V-T) points at atmospheric pressure for simulated D20, D40 and H20 systems. The experimental V-T curves at ambient pressure are shown as a dashed line for Boltorn H20 and a dotted line for Boltorn H40.

After verifying the final structure, production runs of 0.1 ns of the relaxed amorphous cell in the NVE ensemble were performed with a time step of 1 fs and a frame saving frequency of 0.1 ps, creating a final trajectory file of 1000 frames, which was used for further analysis.

The structure of each system was analyzed using the Forcite program to calculate the pair correlation function, the X-ray scattering pattern, and the radius of gyration of dendritic molecules in the bulk. The final trajectory file was used for each of these calculations. The pair correlation function, or  $g(r)$ , is the probability of finding a pair of atoms at a distance  $r$  apart, relative to the probability expected for completely uncorrelated atoms, i.e. an ideal gas

$$g(r) = \frac{1}{4\pi r^2} \frac{1}{N\rho} \sum_{i=1}^N \sum_{k \neq i}^N \langle \delta(r - |r_k - r_i|) \rangle \quad (4)$$

where  $N$  is the total number of atoms,  $\rho$  is the number density of atoms in the cell  $N/V$ , and the angle brackets indicate an ensemble average.<sup>10</sup> For each of the simulated systems the total, and inter and intramolecular  $g(r)$  was calculated using a bin interval of 0.1 Å. Periodic self-interactions were included in the calculations.

X-ray scattering patterns were generated using  $\lambda = 0.154178$  nm and plotted for values of  $2\theta$  between 1 and 60°. The scattering intensity was calculated based on the Debye scattering equation<sup>11</sup>

$$I(Q) = \sum_i \sum_j f_i(Q) f_j(Q) \frac{\sin(Qr_{ij})}{Qr_{ij}} \quad (5)$$

where  $Q$  is the scattering vector ( $Q = |Q| = 4\pi \sin(\theta)/\lambda$ , where  $\theta$  is the half-angle of scattering and  $\lambda$  is the wavelength of X-ray radiation),  $r_{ij}$  is the vector joining atoms  $i$  and  $j$  ( $r_{ij} = |r_i - r_j|$ ), and  $f_i(Q)$  and  $f_j(Q)$  are the atomic scattering factors of atoms  $i$  and  $j$  respectively. The Forcite script utilized a binning function to calculate atom pair

separations,  $r_{ij}$ , for each atomic pair, which were averaged over all atoms in the amorphous cell and all frames in the trajectory file.<sup>12</sup> Atom pair separations greater than the cutoff distance were not included in the calculation. For all simulations, the cutoff distance was set to half the length of each respective amorphous cell.

The average global configuration of each dendritic polymer was described by the radius of gyration,  $R_g$ , which is the root mean square distance of the atoms in the molecule from their common center of mass

$$R_g^2 = \frac{\sum_{i=1}^N m_i s_i^2}{\sum_{i=1}^N m_i} \quad (6)$$

where  $m_i$  denotes the mass of atom  $i$ ,  $s$  denotes the distance of atom  $i$  from the center of mass, and  $N$  denotes the total number of atoms.<sup>13</sup> The  $R_g$  was calculated for all molecules in the amorphous cell and over all frames in the trajectory file. A bin interval of 0.1 Å and mass weighting were used.

A custom-made script was used to identify all hydrogen bonds in the amorphous cell for each simulated system. A hydrogen bond, depicted as X-H...Y-Z, was defined as an attractive interaction between an electropositive donor hydrogen atom from a moiety, X-H, in which X is more electronegative than H, and an electron-rich acceptor atom, Y, from a moiety Y-Z. In this definition, X and Y can be the same element and H and Z can be the same element<sup>14</sup> (Figure 10). For the dendritic polymer systems, the hydrogen bond donor atom was always the hydrogen from the hydroxyl group, and the hydrogen bond acceptor atom was an oxygen atom belonging to the hydroxyl, carbonyl, ester, and ether groups. Two parameters were used to describe a hydrogen bond in the simulations: (1) the length of the hydrogen bond,  $r_{\text{OH}\cdots\text{O}}$ , which was the distance between the hydrogen atom donor and oxygen atom acceptor, and (2) the angle of the hydrogen bond,  $\theta_{\text{OH}\cdots\text{O}}$ ,

which was the angle between the covalent hydroxyl bond (X-H), and the hydrogen bond between the hydrogen donor and oxygen acceptor atom (H···Y) (Figure 10). The hydrogen bond criteria were a maximum hydrogen bond length of 2.5 Å and a minimum hydrogen bond angle of 90°. The script was run through the Discover program on the final trajectory file for each simulated dendritic polymer system.

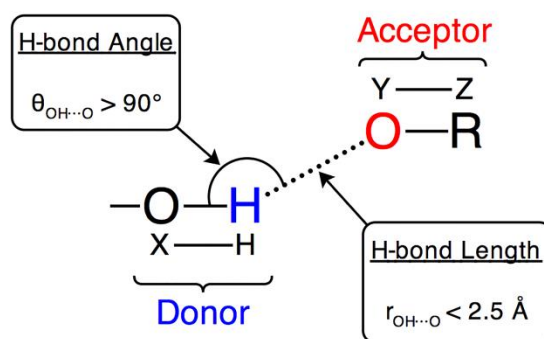


*Figure 10.* Schematic of a hydrogen bond between a donor hydroxyl group, X-H, and an acceptor group, Y-Z. The dotted line (···) represents the hydrogen bond. The hydrogen donor atom is highlighted in blue and the oxygen acceptor atom in red. The hydrogen bond length and angle are indicated with arrows.

## Results and Discussion

### *Esterification of Boltorn H40*

Boltorn H40 was esterified with acetyl chloride to varying degrees of 10, 25, 50, 75 and 100% in order to incrementally decrease the hydroxyl group concentration. Because hydroxyl groups are the only hydrogen bond donors in the dendritic structure, as more hydroxyl groups were converted to non-hydrogen bonding acetyl groups, the hydrogen bonding potential of the entire system was expected to decrease.

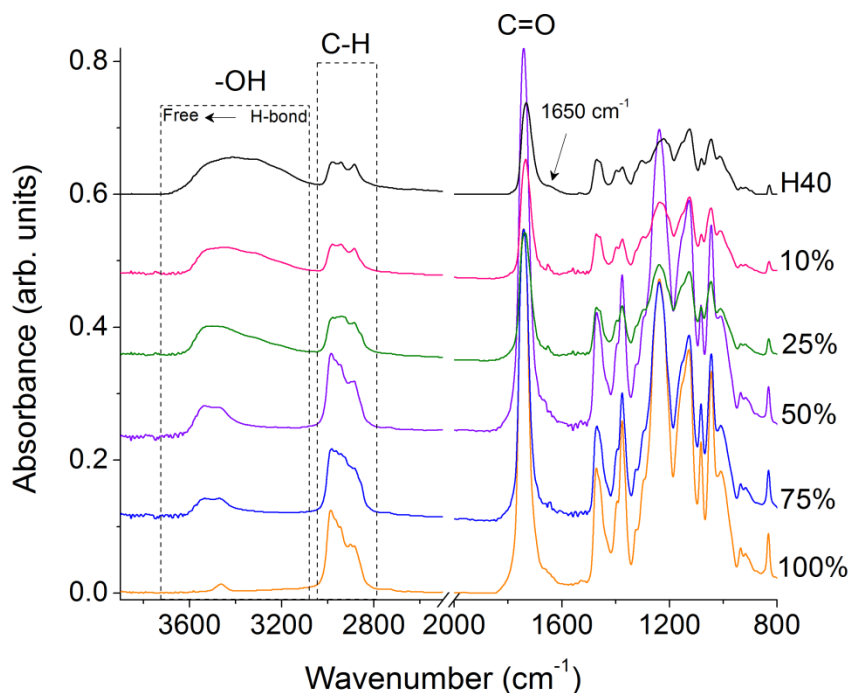


Figure 11. Characterization of esterified H40 showing FTIR spectra for Boltorn H40, and 10, 25, 50, 75, and 100% esterified H40.

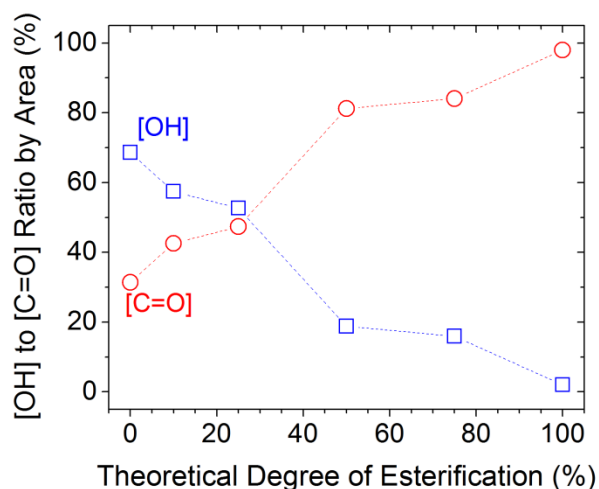
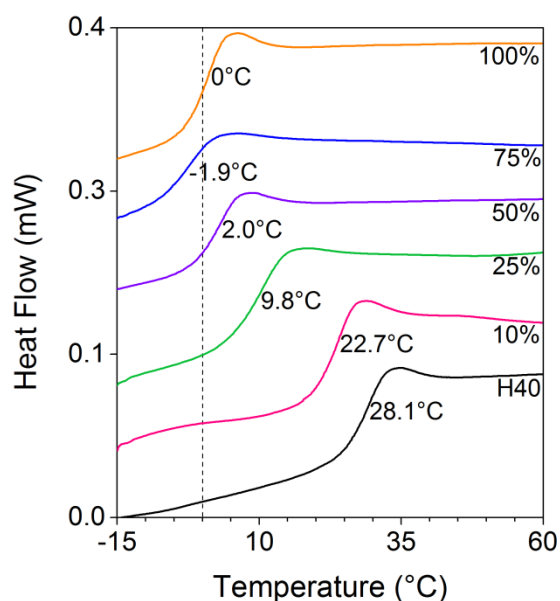


Figure 12. Calculated ratio of [OH] to [C=O] peak areas as a function of the degree of esterification.

The FTIR spectrum of each esterified H40 product is shown in Figure 11, where the reported degree of esterification is the theoretical value. The FTIR spectrum of H40 consisted of a broad and asymmetric hydroxyl stretching vibration ( $\nu_{\text{OH}}$ ) near  $3450\text{ cm}^{-1}$ , overlapping methyl and methylene stretching vibrations ( $\nu_{\text{CH}_3}$  and  $\nu_{\text{CH}_2}$ ) near

approximately 2974 and 2884  $\text{cm}^{-1}$  respectively, a carbonyl stretching vibration ( $\nu\text{C}=\text{O}$ ) near 1732  $\text{cm}^{-1}$ , and a number of vibrations in the fingerprint region that have been identified in the literature (Figure 11).<sup>15</sup> The shoulder near the  $\text{C}=\text{O}$  stretching band, 1650  $\text{cm}^{-1}$ , was assigned to the bending vibration of water, indicating that samples were not completely dry.<sup>15, 16</sup> When a hydroxyl group was esterified it was replaced by an acetyl ( $-\text{OCCH}_3$ ) group, containing one carbonyl moiety. Theoretically then, the concentration of the total number of hydroxyl and carbonyl groups remained constant from sample to sample, i.e. between each esterified product. The extent of esterification was qualitatively related to the ratio of areas of the hydroxyl and carbonyl peaks,  $[\text{OH}]:[\text{COOH}]$ , as shown in Figure 12. As the degree of esterification increased, the area of the  $\nu\text{OH}$  band decreased, whereas the area of  $\nu\text{C}=\text{O}$  increased, and the  $[\text{OH}]:[\text{COOH}]$  ratio decreased from 0.7 : 0.3 at 0% esterification to 0.02 : 0.98 at 100% esterification. In the C-H region, an increase in the intensity and blue-shift of  $\nu\text{CH}_3$  was observed, indicating an increase in the population of methyl esters ( $\text{CH}_3\text{-O-CO-}$ ) belonging to acetyl groups. The asymmetry of the  $\nu\text{OH}$  band increased in the direction of free hydroxyls ( $\nu\text{OH}_{\text{free}} = 3560 \text{ cm}^{-1}$ )<sup>15</sup>, and a blue-shift for  $\nu\text{OH}$  and  $\nu\text{C}=\text{O}$  was observed, indicating a decrease in H-bonding with increasing esterification. For example, the band for  $\nu\text{C}=\text{O}$  shifted from hydrogen bonded  $\text{C}=\text{O}$  groups at 1731  $\text{cm}^{-1}$  for 0% esterified to free  $\text{C}=\text{O}$  groups at 1741  $\text{cm}^{-1}$  for 100% esterified. At 100% esterification, the majority of hydroxyl groups were functionalized as only a very small  $\nu\text{OH}$  band was observed, which in relation to the  $\nu\text{C}=\text{O}$  band was only 2% of the total area of  $\nu\text{OH}$  and  $\nu\text{C}=\text{O}$  (Figure 11). The position of the remaining hydroxyl groups at 100% esterification, 3464  $\text{cm}^{-1}$ , was indicative of H-bonded

hydroxyls. However, this band may also have been caused by residual water in the sample, indicated by the peak at  $1650\text{ cm}^{-1}$ , or by a carbonyl overtone.<sup>16</sup>



*Figure 13.* DSC thermograms for Boltorn H40 and the 10, 25, 50, 75, and 100% esterified H40 samples. The glass transition temperature is indicated for each curve.

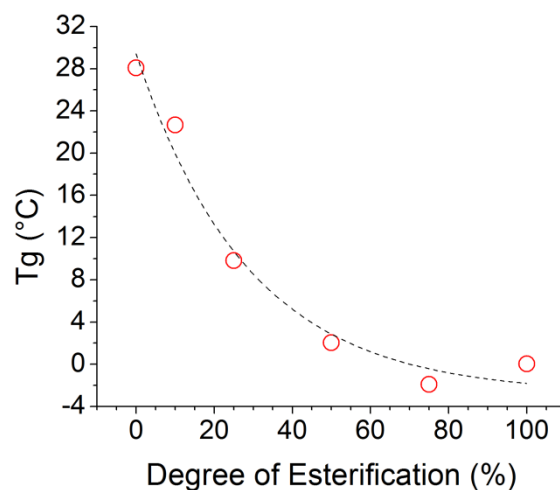


*Figure 14.* Glass transition temperature ( $T_g$ ) as a function of degree of esterification of Boltorn H40.

The trend from FTIR spectroscopy displaying a decrease in hydrogen bonding as esterification increased, was also reflected in the thermal behavior of H40, as the  $T_g$  decreased by approximately  $30^\circ\text{C}$  after approximately all hydroxyl groups were

functionalized (Figures 13 and 14). This dramatic decrease in  $T_g$  indicated a strong influence of hydrogen bonding on the long-range polymer segmental and/or translational mobility. From Figure 14 it was observed that as hydroxyl groups were converted to non-hydrogen bonding acetyl moieties, the  $T_g$  initially decreased linearly, and above 50% functionalization the decrease in  $T_g$  became marginal. Similarly from Figure 11 the wavenumber for C=O and O-H peaks blue-shifted with increasing esterification up till approximately 50% esterification, where after the wavenumber change was marginal. The hydrogen bond network may be weakened beyond some critical point above 50% functionalization of the hydroxyl moieties.

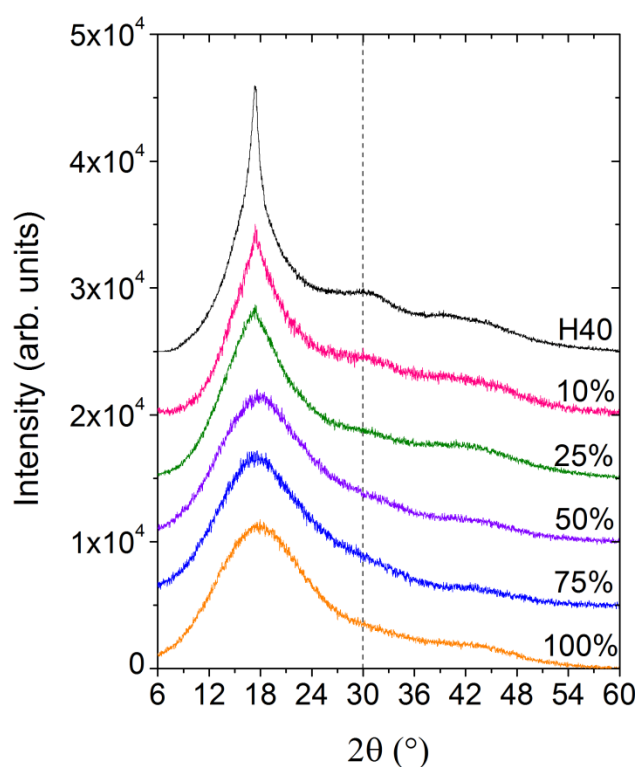


*Figure 15.* WAXD patterns of Boltorn H40, and 10, 25, 50, 75 and 100% esterified H40. The X-ray patterns were normalized and stacked vertically for clarity.

Boltorn H40 and each esterified H40 product, 'H40-CH3', were analyzed by X-ray diffraction to determine whether the peak at  $2\theta \approx 30^\circ$  was related to hydrogen bond



mediated-ordering of hydroxyl groups. The effect of incrementally reducing the number of hydroxyl groups on the X-ray pattern is shown in Figure 15 where the WAXD pattern for each acetylated-H40 product is plotted. As the degree of acetylation increased the sharpness and intensity of the amorphous halo decreased and the intensity of the reflection at  $2\theta \approx 30^\circ$  decreased, while the reflection at  $2\theta \approx 42^\circ$  remained unchanged. The amorphous halo became broader with the increasing degree of acetylation as linear chain segments lost the ability to order. The gradual disappearance of the peak centered at  $2\theta \approx 30^\circ$  with increasing functionalization confirmed that this peak was related to hydroxyl end-groups specifically. The small shoulder in the  $2\theta \approx 30^\circ$  region of the 100% H40-CH3 pattern may have been caused by a small population of unreacted, hydrogen bonded hydroxyls, which were observed in the FTIR spectrum (Figure 11).

#### *Molecular Dynamics Simulations of Bis-MPA Dendritic Polymers*

While the experimental esterification of H40 provided a clue regarding the structural origin of the peak at  $2\theta \approx 30^\circ$ , additional evidence was needed to understand in more detail the spatial arrangements of atoms that led to ordering. To this end, MD simulations were performed on D20, D40, H20, H40, and D40-CH3.

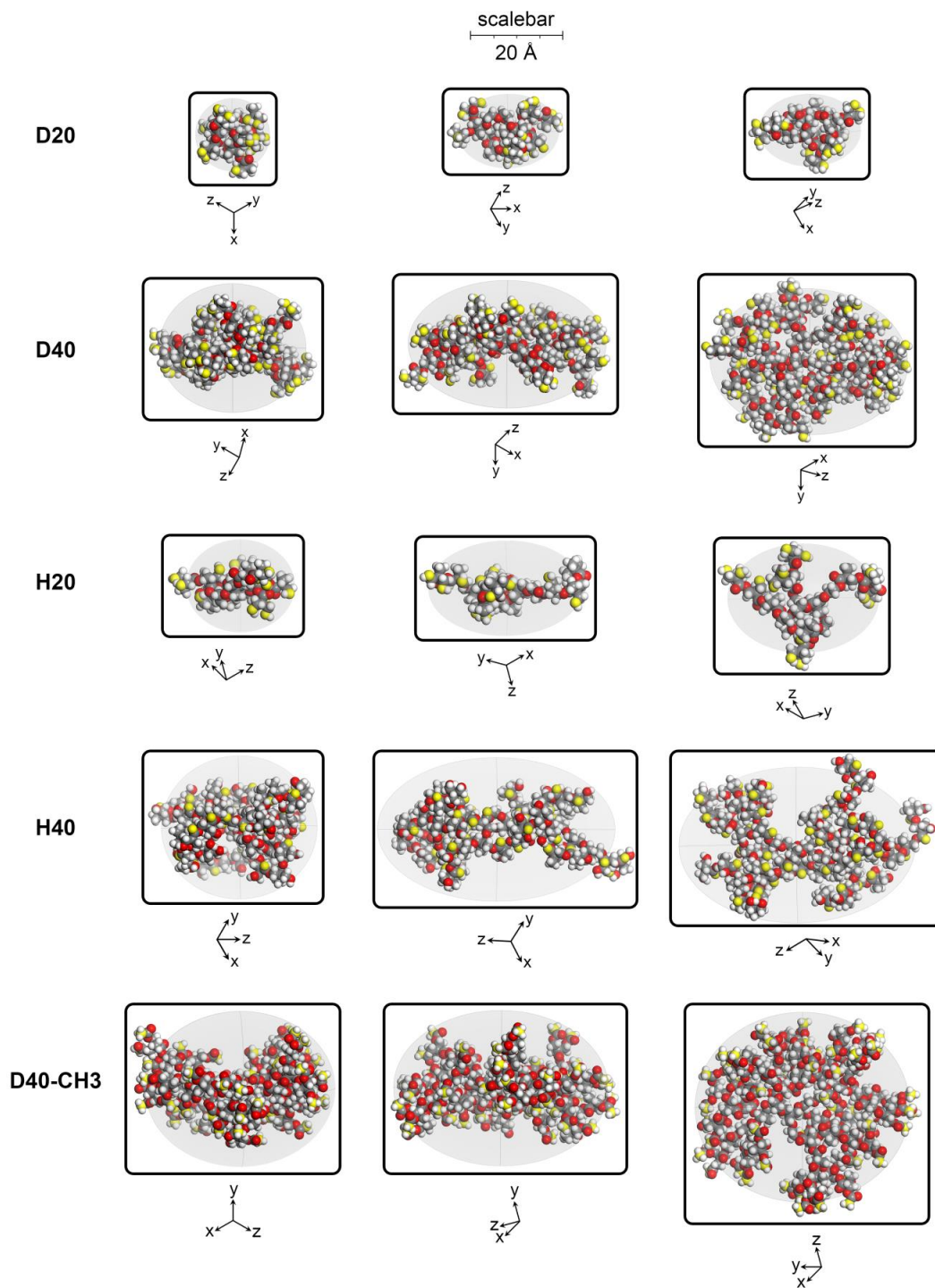


*Figure 16.* Three relatively orthogonal views of a representative molecule from the final amorphous cell of D20, D40, H20, H40, and D40-CH3. The three-dimensional orientation of each molecule is specified by the x,y,z-axes. Each molecule is on the same scale, specified by the scalebar. For D20, D40, H20, and H40 hydroxyl oxygen atoms are highlighted in yellow. For D40-CH3 the terminal methyl carbon atoms are highlighted in yellow. For H20 and H40, the molecules shown are representative of the isomer (a) from Figure 6 and isomer (c) from Figure 7 respectively.

Although it was proposed that bis-MPA HBPs have compact structures, similar to those of globular proteins,<sup>15</sup> an illustration of the bulk globular shape has not been presented in the literature as of yet. The globular configuration of each dendritic species was visualized (Figure 16) in order to understand the 3-D molecular shape and end-group distribution of these non-linear architectures. More specifically, this comparison of molecular shape and end-group distribution between different generations, as well as between perfectly branched vs. irregularly branched systems, provided a structural explanation of the H-bonding organizations. Three approximately orthogonal views of a representative molecule from the final amorphous cell of D20, D40, H20, H40, and D40-CH<sub>3</sub> are shown in Figure 16. For H20 and H40, the molecule shown is representative of the most symmetrical isomer from Figure 6a and Figure 7c respectively. The globular configuration of D40-CH<sub>3</sub> will be discussed in a different section. Readily apparent, the molecular shape for each system resembled a prolate ellipsoid rather than a perfect sphere, where D20 was perhaps the most spherical out of all three systems, and the dendrimers were generally more spherical than their analogous HBPs. The asymmetry of the PP50 core affected the final shape as each molecule was slightly more elongated in the direction of the ethoxylated arm. As expected, D40 and H40 were larger in size compared to D20 and H20, and D40 and H40 appeared to be roughly the same size. When comparing the effect of generation number on shape, for the dendrimers the lower generation, D20, was closer to a sphere while the higher generation, D40, was more spread-out, resembling a pancake-shape. The HBPs were more irregular in shape, and the linear arms could be distinguished. The lower generation H20 seemed to have a more open structure compared to H40. The HBP,

H20, displayed a more elongated ellipsoid, flatter shape and consequently larger  $R_g$ ,  $10.3 \pm 0.2 \text{ \AA}$ , than the analogous perfect dendrimer D20,  $8.8 \pm 0.2 \text{ \AA}$ . Although a similar trend was visually observed for the higher generations, the  $R_g$  of H40,  $14.3 \pm 0.4 \text{ \AA}$ , was very similar to that of D40,  $14.7 \pm 0.5 \text{ \AA}$ . For the dendrimer D40, the atoms were evenly distributed from the center of the molecule. While for the HBP, H40, the atoms were either very close to the center of mass or very far. As a result, the width of the H40 molecule was much smaller than that of D40 in certain segments of the molecule. Thus for H40, by averaging the two extreme locations of atoms with respect to the center of mass, a  $R_g$  value may be obtained which is similar to that of D40. From Figure 16 it was apparent that the molecular shapes of dendrimers as compared to HBPs were different. The linear regions caused the HBP shapes to be less spherical, promoting chain interactions between molecules. The inherently different shapes of dendrimers and HBPs may result in different physical property-molecular weight profiles, where for example, dendrimers have shown a non-monotonic relationship between intrinsic viscosity and generation number<sup>17, 18</sup>, while HBPs displayed a monotonic one.<sup>2, 19</sup>

Besides illustrating the variability in shape of these molecules, in Figure 16, the relative distribution of the end-groups is highlighted by coloring the hydroxyl oxygen atoms in yellow. The majority of the end-groups were visible at the periphery of the molecule for each system, indicating their availability for hydrogen bonding and a lack of backfolding of chain-ends. Compared to D20 and D40, the hydroxyl end-groups of H20 and H40 were distributed more evenly throughout the structure, since they were prevalent within the interior of the structure as well.

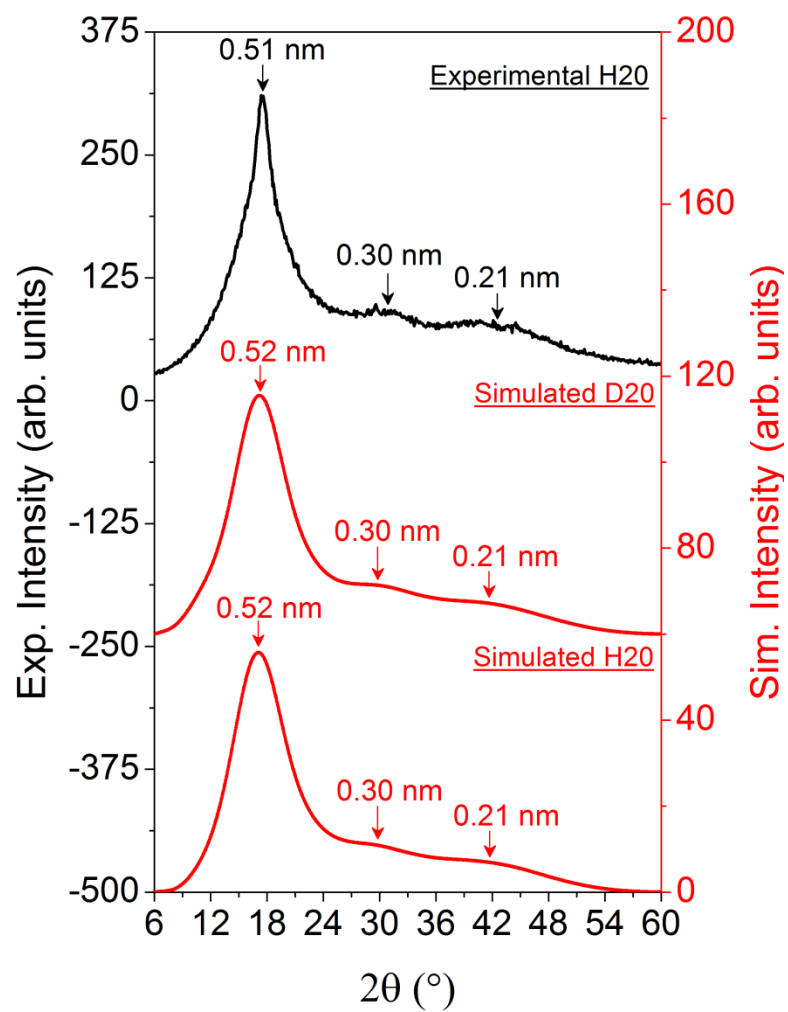


Figure 17. Simulated X-ray scattering patterns for D2O and H2O and experimental WAXD pattern of Boltorn H2O.

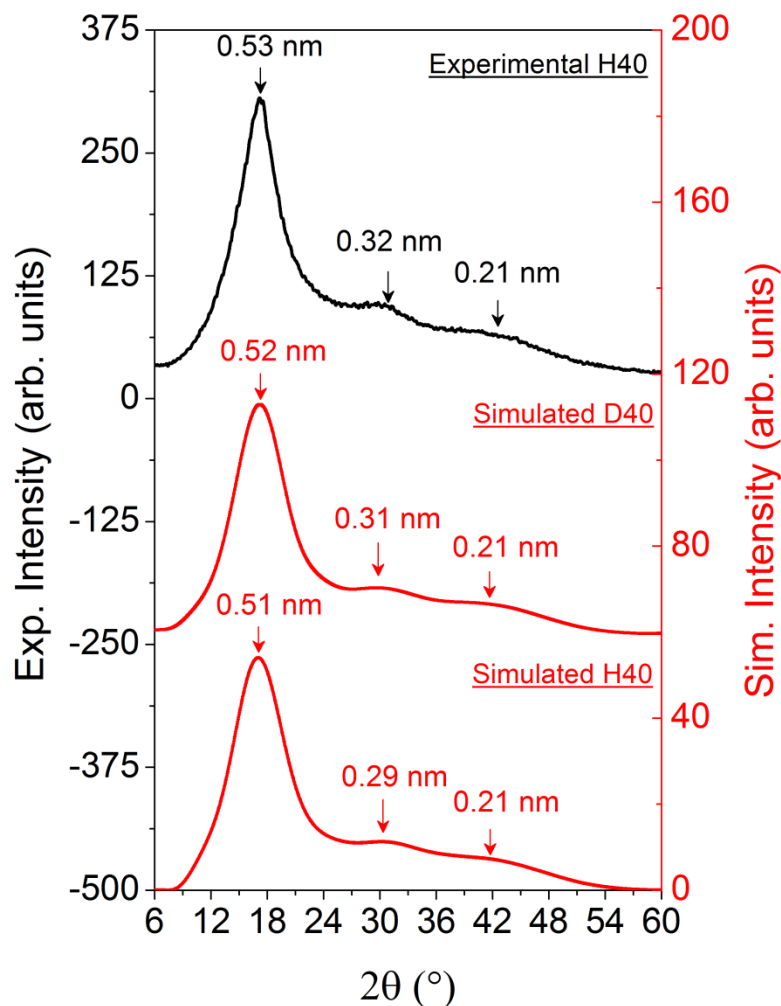
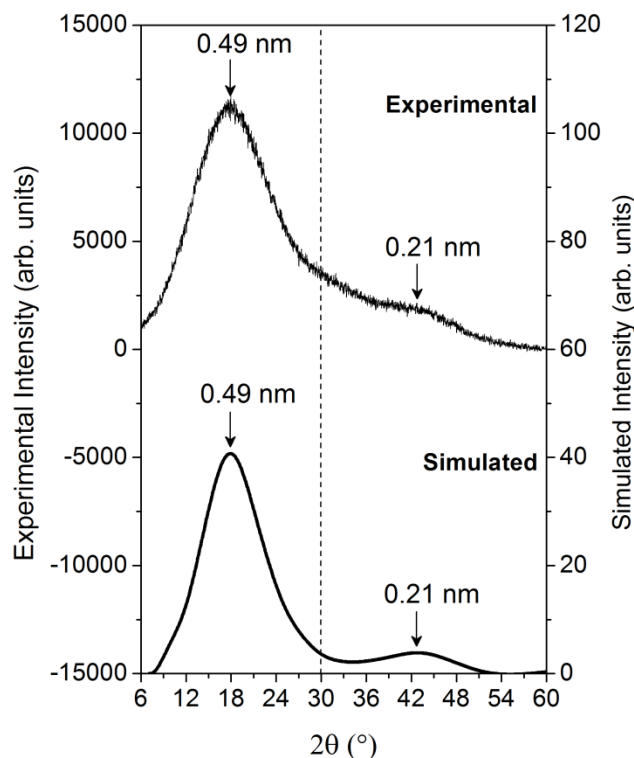


Figure 18. Simulated X-ray scattering patterns of D40 and H40 compared with analogous experimental patterns WAXD pattern of Boltorn H40.

X-ray scattering patterns for D20, D40, H20, and H40 were simulated and compared with the analogous experimental patterns (Figures 17 and 18). The simulated X-ray patterns of D20, D40, H20, and H40 were all in remarkable agreement with the analogous experimental WAXD patterns as each simulated pattern displayed three main peaks: a relatively intense reflection at approximately  $2\theta \approx 17^\circ$  and two small and broad reflections at  $2\theta \approx 30^\circ$  and  $42^\circ$ . The d-spacing values corresponding to each respective peak, indicated with an arrow in Figures 17 and 18, were in good agreement,  $\pm 1\%$ , with

the analogous experimental d-spacing values. The amorphous halo in the simulated patterns of D20 and D40 was broader than that of the experimental H20 and H40 patterns because the perfect dendrimers did not contain linear units. The amorphous halo was broader in the simulated H20 and H40 patterns than in the analogous experimental pattern because ordering of the linear chain segments was unachievable during the relatively short time-scale of the MD simulations. Importantly, the prevalence of a small and broad peak at  $2\theta \approx 30^\circ$  in the simulated X-ray patterns of each polymer confirmed that the origin of this peak was due to ordering of the dendritic structure specifically.

Although the esterification experiments revealed that the intensity of the peak at  $2\theta \approx 30^\circ$  decreased with increasing hydroxyl group consumption, at 100% esterification, this peak did not completely disappear as a small shoulder was observed at  $2\theta \approx 30^\circ$ , which may have been caused by residual unreacted, H-bonded hydroxyl groups evident by a small peak at  $3464\text{ cm}^{-1}$  in the FTIR spectrum (Figure 11). To confirm that the peak at  $2\theta \approx 30^\circ$  was related to the ordering of H-bonded hydroxyl groups, a control system was modeled, which mirrored the 100% acetylated H40, but definitely consisted of no hydroxyl groups and consequently no hydrogen bonds. This control system was the 100% acetylated perfect dendrimer D40, called D40-CH<sub>3</sub>. Three relatively orthogonal views of a representative molecule of D40-CH<sub>3</sub> are shown in Figure 16. Replacing the hydroxyl end-groups with acetyl moieties resulted in a larger and less compact molecule, exhibited by the higher  $R_g$  of D40-CH<sub>3</sub>,  $16.6 \pm 0.9\text{ \AA}$ , compared to D40,  $14.7 \pm 0.5\text{ \AA}$ . No considerable difference was observed in the location of the end-groups of D40-CH<sub>3</sub> compared to D40, i.e. for both molecules end-groups seemed to be located at the periphery of the molecule and not backfolded into the structure.



*Figure 19.* Experimental WAXD pattern of 100% acetylated H40 (top) compared with the simulated X-ray pattern for D40-CH3 (bottom).

Shown in Figure 19, the X-ray scattering pattern for D40-CH3 was simulated and compared with the experimental WAXD pattern of 100% acetylated H40. The simulated X-ray pattern was in agreement with the experimental one as two main reflections were observed at  $2\theta \approx 17^\circ$  and  $42^\circ$  and the d-spacings corresponding to these peaks were in good agreement with the experimental d-spacing values. Furthermore, the same trend was observed for the simulated systems (D40 to D40-CH3) as for the experimental ones (H40 to 100% H40-CH3), that the amorphous halo was broader in the 100% esterified X-ray pattern compared to that of the pure, hydroxylated polymer X-ray pattern. The broadening of the amorphous halo upon esterification may be related to an increase in the heterogeneity of the short-range order, i.e. broader distribution of the correlations between C-C and C-O atoms in the bulk of the polymer. The simulated pattern in Figure



19 clearly displays the absence of a peak at  $2\theta \approx 30^\circ$ , which confirmed that the structural origin of this reflection was specifically related to hydrogen bond-mediated ordering of the hydroxyl end-groups. This finding also clarified that the shoulder from the experimental WAXD pattern was probably caused either by unreacted hydroxyl groups or residual water in the sample.

A preliminary visual approach was applied to observe potential arrangements of hydrogen bonded hydroxyl groups in each respective amorphous cell. Using the Materials Studio program (Accelrys Software, Inc.: San Diego), H-bonds were calculated between all atoms in the amorphous cell, generating a blue-dashed line between H-bonded atoms only. All atoms except for the hydroxyl oxygen and hydrogen atoms were deleted (Figures 20 and 21). The amorphous cell was examined for any apparent organizations and multiple clusters of H-bonded O-H $\cdots$ O atoms were observed. The amorphous cell consisting of just hydroxyl oxygen and hydrogen atoms for each dendrimer (Figure 20) and for each hyperbranched polymer (Figure 21) is shown to the left. Representative examples of H-bonded clusters are highlighted in blue in the amorphous cell, and an isolated view of each respective cluster is shown. Clusters of varying length and shape, linear and cyclic, were observed. The length of each cluster was defined by the number of hydrogen bonds between the hydrogen atom donor and oxygen atom acceptor. It should be noted that in Figures 20 and 21 all of the atoms in the amorphous cell are not on the same plane and dimensionality of the clusters is lost. A 3-D view of these clusters is provided in Figure 22, which shows three views of the final D20 amorphous cell which only includes oxygen and hydrogen atoms involved in cluster formation. Figure 22 shows that a large number of clusters were prevalent in the amorphous cell, and most of the

clusters were between one and three hydrogen bonds in length. The analogous 3-D view was similar for D40, H20, and H40, as shown in the Appendix, Figure 56.

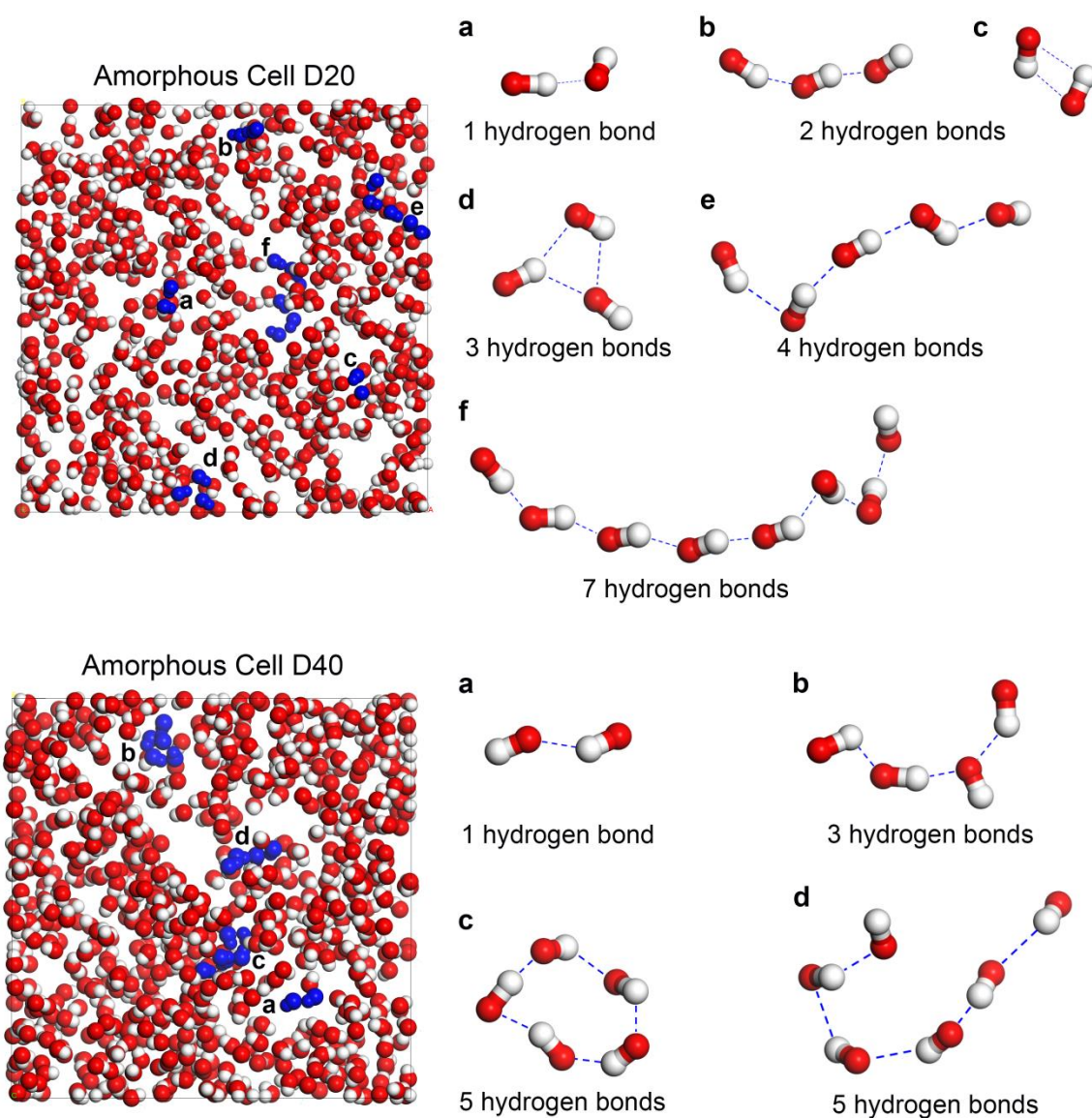


*Figure 20.* Visualization of linear and cyclic hydrogen bonded clusters of D20 and D40. For each simulated polymer, the amorphous cell containing hydroxyl oxygen and hydrogen atoms is shown to the left and representative clusters are highlighted in blue. Each respective isolated representative cluster, a-f for D20 and a-d for D40, is shown to the right, where blue dashed lines represent hydrogen bonds. The length of each cluster is indicated by the number of hydrogen bonds.

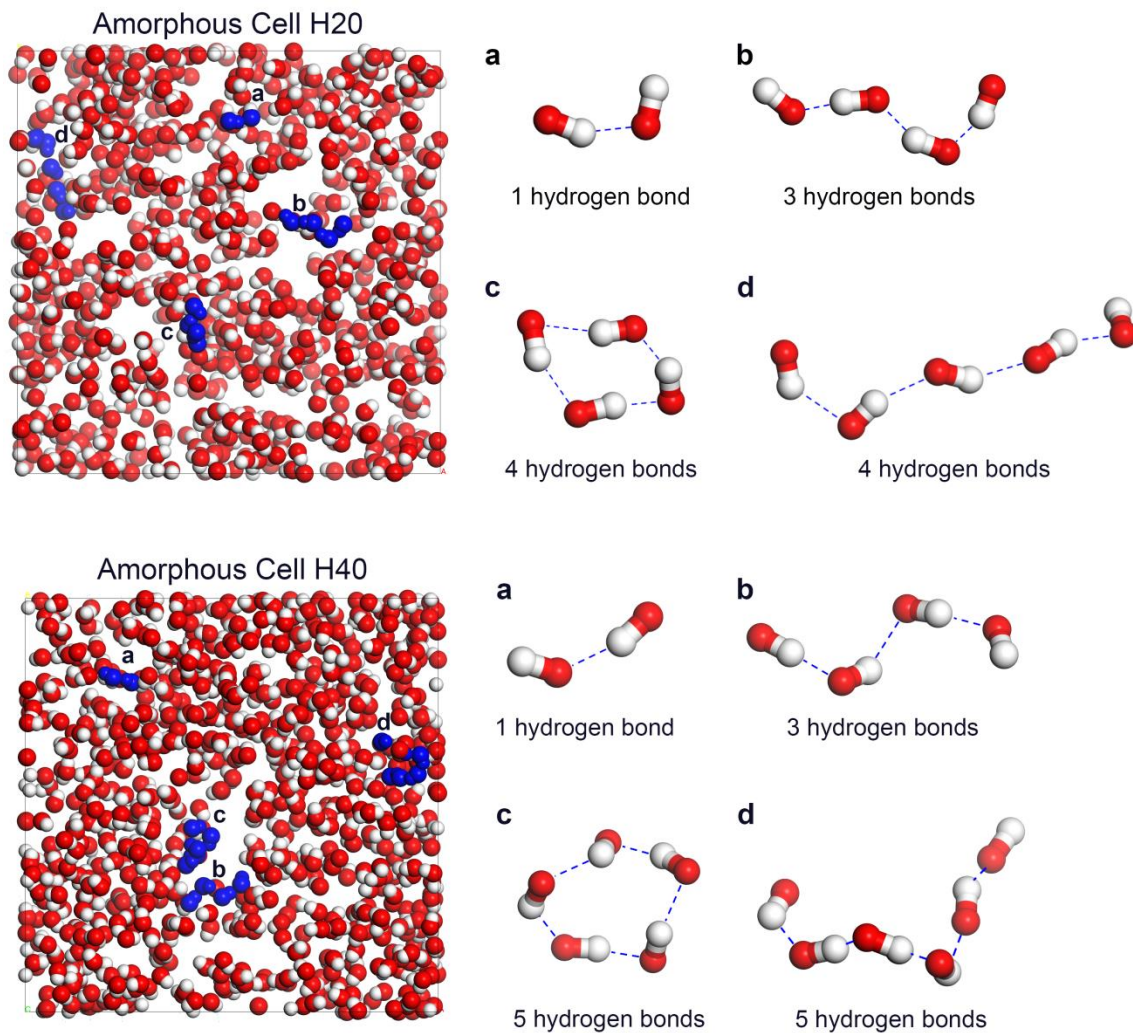


*Figure 21.* Visualization of linear and cyclic hydrogen bonded clusters of H2O and H4O. For each simulated polymer, the amorphous cell containing hydroxyl oxygen and hydrogen atoms is shown to the left and representative clusters are highlighted in blue. Each respective isolated representative cluster, a-d, for H2O and H4O, is shown to the right, where blue dashed lines represent hydrogen bonds. The length of each cluster is indicated by the number of hydrogen bonds.

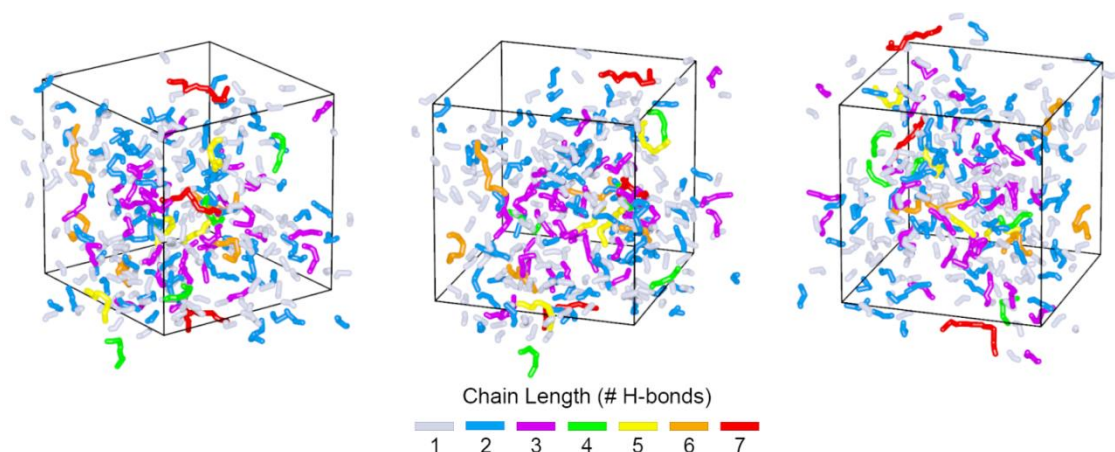


*Figure 22.* Three-dimensional view of “chain-like-clusters” in the final relaxed amorphous cell of D20. Three rotated views of the amorphous cell are shown. Hydrogen and oxygen atoms, as well as covalent and hydrogen bonds are represented by sticks, to form a continuous O-H $\cdots$ O representation of a cluster. The different colors represent clusters of different lengths. Hydroxyl hydrogen and all types of oxygen atoms were included in the clusters.

#### *Statistical Hydrogen Bond Cluster Analysis*

A statistical hydrogen bond analysis, over all 1000 frames of the final trajectory file, was conducted for each of the simulated, hydroxylated dendrimers and HBPs. A ‘chain-like’ cluster was defined as a group of O-H $\cdots$ O hydrogen bonded atoms interconnected consecutively by a chain of hydrogen bonds (Figure 23a). By this definition, the first and last atoms in a cluster were always oxygen atoms, and the total number of atoms in a cluster was always an odd number. The length of the cluster was defined by the number of hydrogen bonds constituting the chain. For example, the cluster shown in Figure 23a has a length of four hydrogen bonds. Single hydrogen bonds (Figure 23c,d) and free atoms (Figure 23\*) had a cluster length of one and zero respectively.

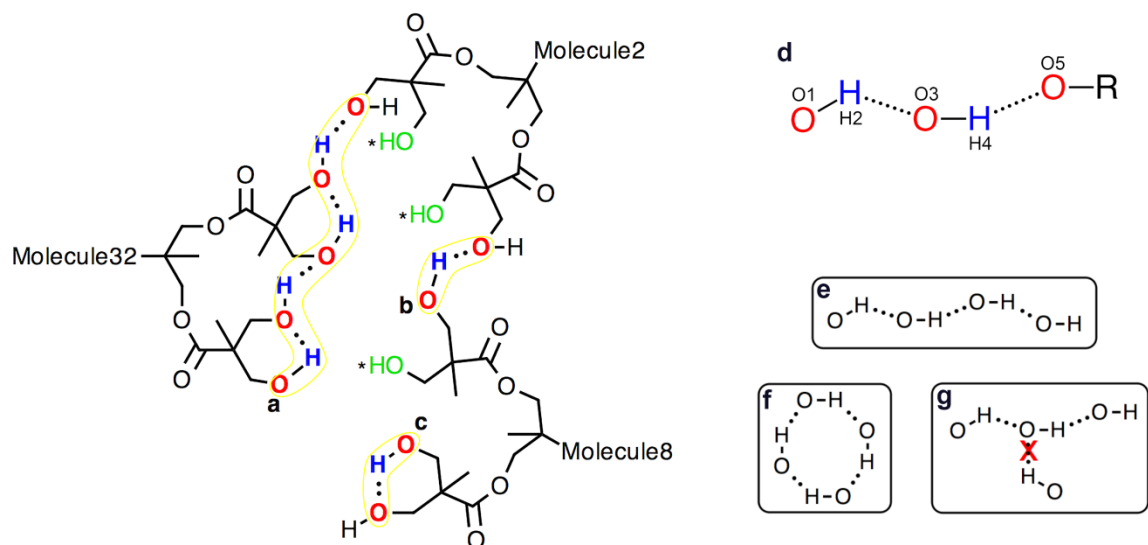


*Figure 23.* Schematic displaying an example of (a) cluster of hydrogen bonded O-H...O groups, (b) single hydrogen bond between two different dendritic molecules, and (c) single hydrogen bond on the same molecule. Free (non-hydrogen bonded) hydroxyls are highlighted in green and with an asterisk (\*). Three different dendritic molecules are depicted, where each molecule name is indicated. (d) Schematic of a hydrogen bonded cluster of O-H...O groups where acceptor oxygen atoms are highlighted in red and the donor hydrogen atoms are highlighted in blue. The ‘atom name’ is specified next to each oxygen and hydrogen atom in the chain. Examples of three potential cluster shapes (e) linear, (f) cyclic, (g) and branched. The red “x” in (g) denotes that branched clusters were not allowed according to the criteria of the hydrogen bond script. For all structures shown, dotted lines (•••) represent hydrogen bonds and solid lines (–) represent covalent bonds.

A custom-made program, ‘TracedHbonds’, was used to identify clusters in the amorphous cell of each simulated dendritic system. Elaborating on the definition of a cluster given above, a more technical definition is provided in the context of Figure 23d, which depicts a cluster with a length of two hydrogen bonds, where each ‘atom name’ is displayed next to its corresponding oxygen and hydrogen atom. The conditions that identify a cluster in ‘TracedHbonds’ were as follows:

- (1) Assuming that atom ‘O1’ and atom ‘H2’ are covalently bonded, and atom ‘O3’ is covalently bonded to atom ‘H4’

(2) If atom 'H2' is hydrogen bonded to atom 'O3', and atom 'H4' is hydrogen bonded to atom 'O5'

(3) Then the atoms 'O1', 'H2', 'O3', 'H4', and 'O5' are connected consecutively by alternating covalent and hydrogen bonds, forming a 'chain-like' cluster

The criteria for cluster formation also specified that a hydrogen bond donor could form only one hydrogen bond with an acceptor and vice versa, which restricted the shape of the resultant clusters to linear (Figure 23e) and cyclic (Figure 23f), as branching was not allowed, Figure 23g.

The total amount of clusters for each cluster length was tabulated separately for linear and cyclic clusters. For each individual cluster in the amorphous cell, the following parameters were obtained: (1) cluster length, in terms of the number of hydrogen bonds and atoms in the cluster, (2) x-y-z coordinates, atom name, molecule name, and specific forcefield of each atom within the cluster, and (3) the end-to-end distance, or distance between the first and last atom of the cluster. Specifying the forcefield of each atom was important for discerning the specific identity of the oxygen atom acceptor, i.e. hydroxyl, carbonyl, ester, or ether oxygen atom.

Characterization of the H-bond network pervasiveness revealed that approximately half of the oxygen atoms participated in H-bonding, where interestingly the amount of H-bonding oxygen atoms was very similar for D20, D40, H20, and H40 ( $45\pm 3$ ,  $45\pm 2$ ,  $45\pm 2\%$ , and  $45\pm 2\%$  respectively), indicating that molecular size and structure did not affect the degree of H-bonding. In terms of geometry, the majority of clusters were linear and less than 2% were cyclic for each dendritic polymer. The H-bond length (defined in Figure 10) was on average the same for D20, D40, H20, and H40, 2.0

$\pm 0.3$  Å. The average H-bond angle was also similar for D20, D40, H20, and H40  $139 \pm 20$ ,  $138 \pm 20$ ,  $138 \pm 21$ , and  $137 \pm 21^\circ$  respectively. Both the  $r_{\text{O-H}\cdots\text{O}}$  and  $\theta_{\text{O-H}\cdots\text{O}}$  values indicated that these dendritic polymers had H-bonds of moderate strength.<sup>20, 21</sup> Compared to liquid water, the H-bond network of the dendritic species was less extensive since for water, there were reportedly almost as many hydrogen bonds as covalent bonds.<sup>22</sup> The H-bond length and angles for the dendritic polymers were not very different from what has been reported in the literature for liquid water,  $r_{\text{O}\cdots\text{H}} \approx 1.83$ ,<sup>23</sup>  $1.86$ ,<sup>24</sup>  $1.74$ ,<sup>25</sup>  $1.85$ ,<sup>9</sup>  $1.8$  Å,<sup>26</sup> and  $\theta_{\text{O-H}\cdots\text{O}} \approx 162$ <sup>23</sup> and  $172^\circ$ .<sup>27</sup> Compared to liquid HF, the H-bonds in the dendritic polymers were less strong since  $r_{\text{H}\cdots\text{F}} \approx 1.45$ ,<sup>28</sup>  $1.6$ ,<sup>29, 30</sup> and  $1.6$ - $1.8$ <sup>31</sup> Å and  $\theta_{\text{F-H-F}} \approx 165$ ,<sup>29</sup>  $150$ - $180$ ,<sup>28</sup> and  $144$ - $170^\circ$ .<sup>31</sup>

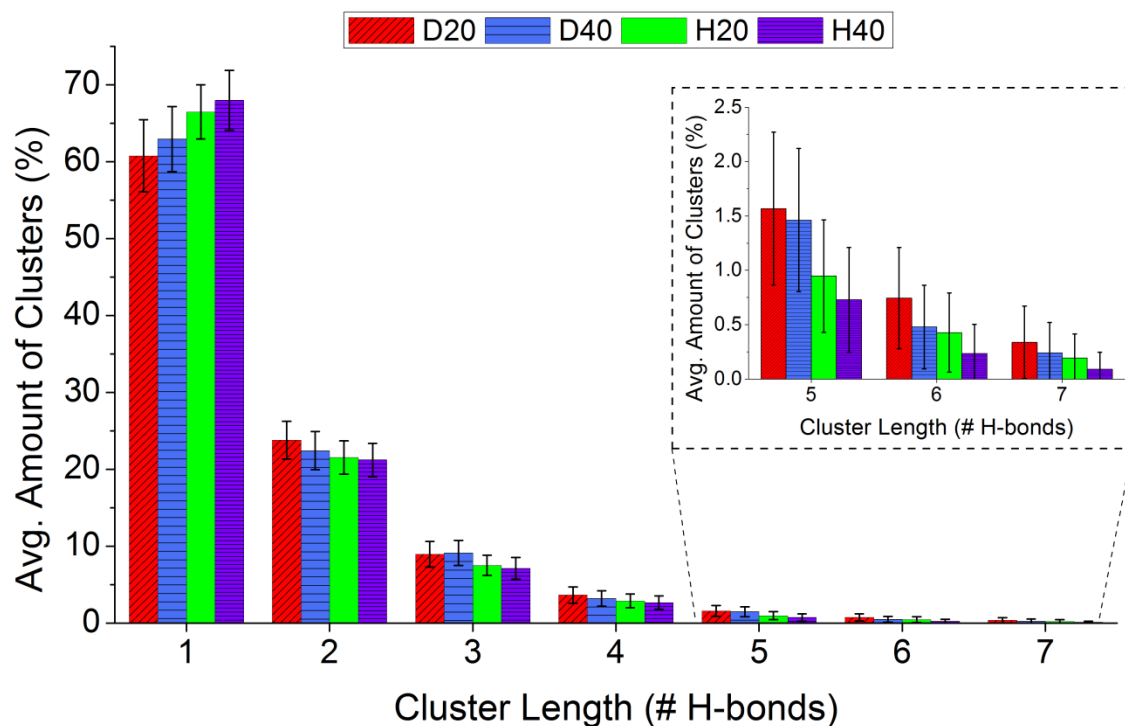


*Figure 24.* Average amount of clusters, as a percentage of the total number of clusters, for each cluster length, for D20, D40, H20, and H40. The cluster length is defined by the number of H-bonds in the cluster. Error bars indicate standard deviation over 1000 frames. The inset displays a zoomed-in view of the amount of clusters for a chain length of 5, 6, and 7 hydrogen bonds.

The total number of observed clusters was similar, within standard deviation, for each simulated system where H20 formed the most clusters,  $321 \pm 36$ , followed by H40,  $317 \pm 30$ , followed by D20,  $304 \pm 36$ , and D40 formed the least amount of clusters,  $289 \pm 33$ . The amount of clusters for each cluster length, calculated as a percent of the total number of clusters, is shown in Figure 24 for D20, D40, H20, and H40. The amount represents the average and standard deviation of the number of clusters over all 1000 frames of the final trajectory file. For all four systems, the majority of clusters were composed of only one H-bond and, the average cluster length was approximately two hydrogen bonds. As the chain length increased, the number of clusters exponentially decreased, a trend which was also observed for clusters in liquid HF.<sup>30</sup> Overall, D20, D40, H20, and H40 displayed similar characteristics, such as the amount of clusters per chain length, and a maximum chain length of seven H-bonds. When comparing the perfect dendrimers with each other, and the HBPs with each other, only a small difference was observed between the higher and lower generations, indicating that the degree of H-bonding was not considerably affected by generation number. D20 displayed 5% more total clusters than D40, and H20 displayed only 1% more clusters than H40. D40 displayed a slightly higher propensity to form single hydrogen bonds, 63%, than D20, 61% and similarly H40, 68%, formed slightly more H-bonds than H20, 66%. For clusters  $\geq 2$  hydrogen bonds, D20 and D40 showed almost the same amount of clusters for each cluster length, where D20 displayed only 1% more clusters for each cluster length as compared to D40. The same observation was made for clusters  $\geq 2$  hydrogen bonds for H20 compared to H40.



The more noticeable differences were between the perfect dendrimers and their analogous HBPs. Generally, the HBPs displayed a slightly higher propensity to form single H-bonds as compared to the dendrimers, 66% vs. 61% for H20 and D20, and 68% vs. 63% for H40 and D40 respectively. For clusters  $\geq 2$  H-bonds though, cluster formation was similar, where D20 displayed 1-2% more clusters per chain length compared to H20 and D40 displayed 1-2% more clusters per chain length compared to H40. Structures which contained H-bond donors (-OH) within the interior of the molecule, as opposed to solely at the periphery, displayed a higher propensity to form single H-bonds and a slightly lower propensity to form interconnected H-bonded chains.

The bis-MPA based dendritic structures contained four types of H-bond oxygen acceptors located in different parts of the structure. The hydroxyl groups existed at the periphery, carbonyl and ester oxygen atoms were located in the shell, and the ether oxygen atoms were located in the core of the structure. The number of H-bonds for each type of oxygen acceptor atom was calculated (Table 1) to infer (i) which parts of the dendritic structure were most available for hydrogen bonding and (ii) the effect of molecular size on hydrogen bonding.

Table 1

*Contribution of each oxygen acceptor type to cluster formation, and total number of hydrogen bonds for D20, D40, H20, and H40*

	Contribution to Clusters (# of H-bonds)				Total Number of H-bonds
	Hydroxyl	Carbonyl	Ester	Ether	
D20	347 (60%)	189 (32%)	22 (4%)	25 (4%)	583
D40	322 (60%)	192 (36%)	18 (3%)	5 (1%)	537
H20	306 (53%)	199 (35%)	45 (8%)	26 (5%)	575
H40	273 (49%)	225 (41%)	51 (9%)	6 (1%)	555

Note: Percentage was calculated out of the total number of hydrogen bonds.

The total number of H-bonds and the relative contribution of each type of oxygen acceptor atom to cluster formation are shown in Table 1. The degree of contribution of each type of oxygen atom to cluster formation was as follows: hydroxyl > carbonyl >> ester  $\geq$  ether. That OH $\cdots$ OH interactions were the main type of H-bond was in agreement with previous computer simulations<sup>32</sup> but in disagreement with FTIR experiments that postulated the in OH $\cdots$ O=C interactions to be most predominant.<sup>15</sup> In the literature experimental FTIR analysis, the degree of hydrogen bonding was indirectly inferred through a set of assumption. The approach employed in this analysis was more direct in that each atom involved in H-bonding was counted and no assumptions were needed to infer the degree of H- bonding.

For the dendrimers, generation number did not considerably affect the degree of hydrogen bonding, as the lower generation dendrimer, D20, formed only approximately 9% more H-bonds than that the higher generation dendrimer, D40. Although the contribution of OH $\cdots$ OH type bonds to cluster formation was similar for each of the dendrimers, 60%, D20 displayed  $\sim$ 8% more OH $\cdots$ OH bonds, 347, than D40, 322 (Table 1). This indicated that although D40 has 48 more hydroxyl end-groups per molecule than D20, D20's smaller, more compact shape placed end-groups in closer proximity to one another (increasing their hydrogen bond interactions). The relative contribution of OH $\cdots$ O=C bonds to cluster formation was slightly greater for D40, 36%, than for D20, 32%, which was expected because D40 has a greater fraction of dendritic-to-terminal units than D20 (0.47-to-0.53 and 0.33-to-0.67 respectively). The number of OH $\cdots$ O=C bonds was very similar between the generations though, as D20 displayed only  $\sim$ 2% fewer OH $\cdots$ O=C bonds, 189, than D40, 192.

For the HBPs, generation number also did not affect the degree of H-bonding since H20 displayed only 4% more H-bonds than H40. A larger disparity was seen between the contributions of hydroxyls vs. carbonyls for H20 vs. H40 as compared to D20 vs. D40. The contribution of OH $\cdots$ OH type bonds to cluster formation was higher for H20, 53%, than H40, 49%, and H20 displayed approximately 12% more OH $\cdots$ OH bonds, 306, than H40, 273, indicating that the hydroxyl groups were more available for H-bond participation in the lower generation HBP. This can be explained by considering that there is an even greater disparity in the distances between linear hydroxyls and terminal ones in H40 compared to H20 as the fourth generation is much larger than the second generation. Therefore, hydroxyls closer to the core may be unavailable for H-bonding. The relative contribution of OH $\cdots$ O=C bonds to cluster formation was greater for H40, 41%, than for H20, 35%, which was expected due to the higher dendritic-to-terminal ratio for the fourth generation. The number of OH $\cdots$ O=C bonds was greater by 14% for H40, 225, than for H20, 199.

The hyperbranched polymer, H20, and perfect dendrimer, D20, displayed a similar degree of hydrogen bonding, as D20 formed only ~2% more H-bonds than H20 (Table 1). The main difference between these two species was in the relative contributions of hydrogen bond acceptors to cluster formation. The carbonyl, ester, and ether oxygen atoms contributed more to cluster formation for H20 than for D20, and H20 displayed a smaller contribution from the hydroxyl groups to cluster formation, 53%, than D20, 60%. D20 displayed ~12% more OH $\cdots$ OH bonds, 347, than H20, 306 whereas H20 displayed ~5% more OH $\cdots$ O=C bonds, 199, than D20, 189. Placing end-groups at the periphery of the structure increased the number of end-group interactions and placing

the hydroxyl end-groups in the interior of the structure activated interior moieties, i.e. carbonyl and ester, for hydrogen bonding.

The hyperbranched polymer, H40, and perfect dendrimer, D40, also displayed a similar degree of hydrogen bonding, as D40 formed approximately 3% more H-bonds than H40 (Table 1). The contribution of carbonyl, ester, and ether oxygen atoms was even higher in the case of the fourth generation HBP as compared to the second generation HBP. H40 displayed an even lower contribution from hydroxyl groups to cluster formation, 49%, than D40, 60%. Thus the trends seen for D20 vs. H20 were slightly more exaggerated when comparing the higher generation dendrimer and HBP.

Only a very small percentage of ester and ether oxygen atoms,  $\lesssim 9\%$ , contributed to cluster formation (Table 1). This was generally expected due to relatively lower electronegativity of ester and ether oxygen atoms. D20 displayed more ester and ether H-bonds than D40. H40 displayed more ester but almost the same amount of ether bonds as D40. H20 displayed almost twice as many ester, and the same amount of ether H-bonds compared to D20, and almost the same amount of ester and slightly more ether bonds than H40. Therefore, H-bonding with these sterically hindered, interior acceptors increased with closer proximity of the end-groups to the interior of the structure.

The idea of a compact structure similar to globular proteins, which was proposed in the literature,<sup>15</sup> was visually observed from the MD simulations as each dendritic polymer displayed a three-dimensional ellipsoidal shape (Figure 16). The H-bond analysis from the MD simulations revealed that a considerable portion of the hydroxyl end-groups and carbonyl moieties were not H-bonded, which indicated that these dendritic polymers have unreachable, buried sites within the structure due to their

globular nature. Experimental esterification of H40 also displayed that a small portion of the hydroxyl groups may be unreachable for functionalization as the FTIR spectrum displayed a small  $\nu\text{OH}$  peak, approximately  $3464\text{ cm}^{-1}$ , even at 100% theoretical esterification (Figure 11).

#### *Oxygen-Oxygen Pair Correlation and Nearest Neighbor Analysis*

The pair correlation function for oxygen atoms,  $g(r)_{\text{O-O}}$ , was calculated for each dendritic species and compared with the  $g(r)_{\text{O-O}}$  of liquid water (Figure 25b) to analyze the short-range order within the dendritic polymers and to gain more supporting evidence of cluster formation. For each dendritic species,  $g(r)_{\text{O-O}}$  was calculated from hydroxyl and carbonyl oxygen atoms only, because these type of oxygen atoms constituted ~90% of the H-bonded clusters.

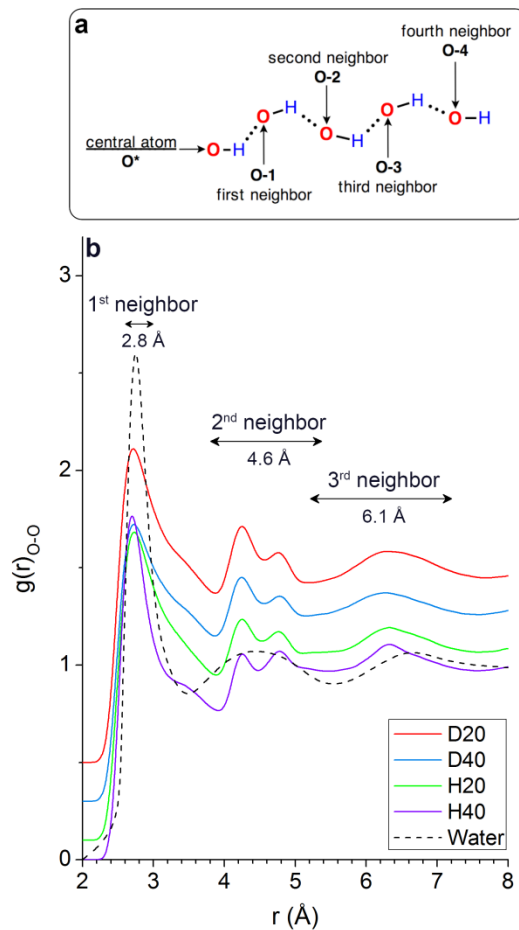


Figure 25. (a) Isolated hydrogen bonded cluster where dotted lines ( $\cdots$ ) represent hydrogen bonds and solid lines ( $-$ ) represent a covalent bonds. The central oxygen atom in the cluster is labeled as  $O^*$ . The first, second, third, and fourth oxygen atom neighbors are labeled as  $O-1$ ,  $O-2$ ,  $O-3$ , and  $O-4$  respectively. (b) Oxygen-oxygen radial distribution function,  $g(r)_{O-O}$ , calculated for carbonyl and hydroxyl oxygen atoms only, for D20, D40, H20, and H40. The dashed line represents the  $g(r)_{O-O}$  of water, replotted from the literature.<sup>1</sup> D20, D40, H20, and H40 curves were stacked vertically.

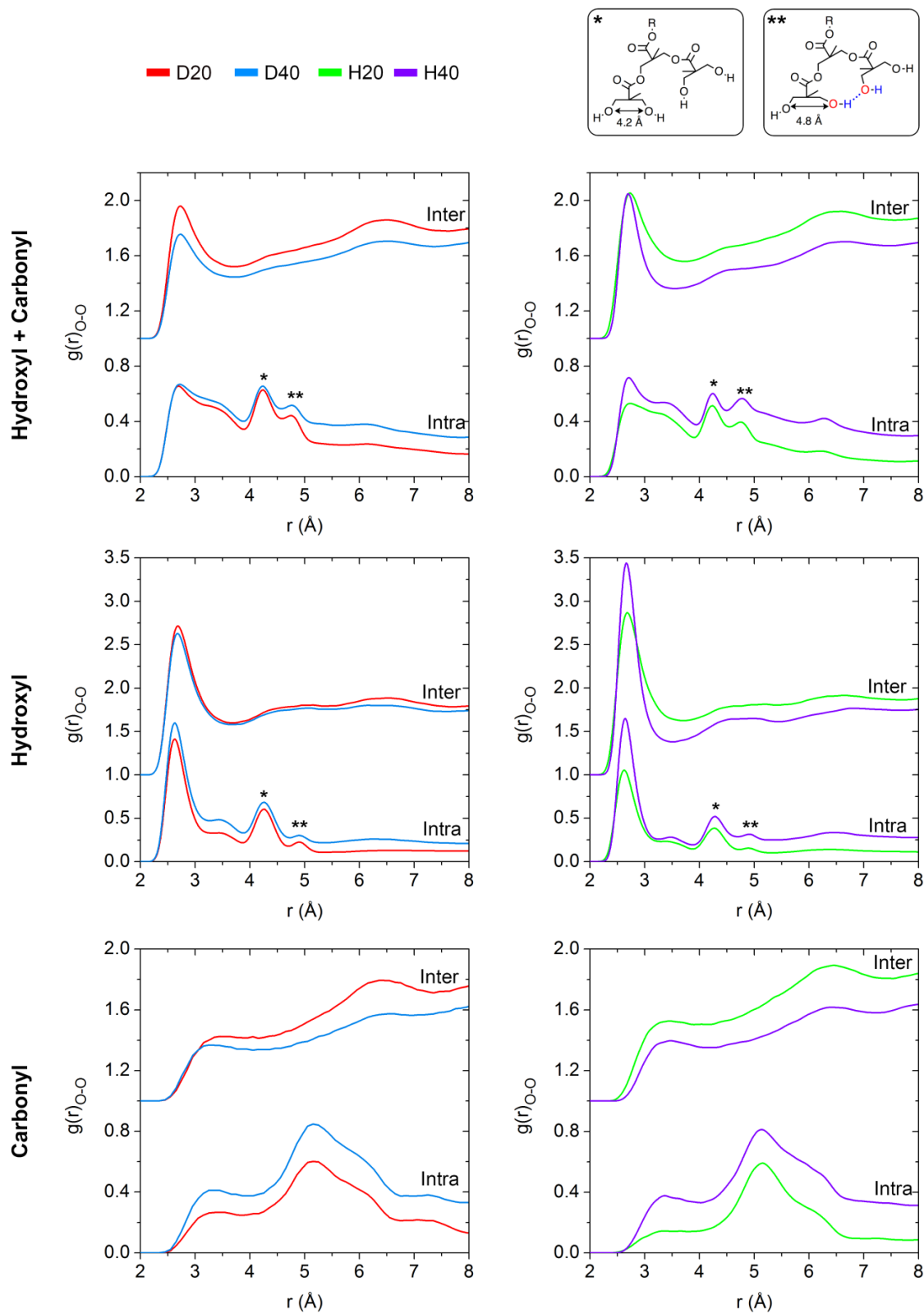


Figure 26. The inter and intramolecular  $g(r)_{\text{O-O}}$  for D20, D40, H20, and H40 calculated for carbonyl and hydroxyl oxygens, hydroxyl oxygens only, and carbonyl oxygens only.

The  $g(r)_{O-O}$  patterns of D20, D40, H20, and H40 were very similar to each other, and to the  $g(r)_{O-O}$  pattern of water (Figure 25b). Each pattern displayed evidence of short-range order through three coordination shells. The first shell was observed as a relatively narrow peak centered at  $\sim 2.8 \text{ \AA}$ , which was very similar in value to the d-spacing corresponding to  $2\theta \approx 30^\circ$ ,  $\sim 0.3 \text{ nm}$ , from X-ray pattern, indicating that the  $2\theta \approx 30^\circ$  peak was related to O-O atom correlations specifically. The second shell, centered at  $4.6 \text{ \AA}$ , was broader and displayed two maxima at  $4.3$  and  $4.8 \text{ \AA}$ . The third shell was the broadest, centered at  $\sim 6.3 \text{ \AA}$ . The maxima at  $4.3$  and  $4.8 \text{ \AA}$  arose from intramolecular O-O correlations between hydroxyl groups only (Figure 26), indicating that these two peaks were related to structural correlations unrelated to the H-bond clusters. Through further probing of the dendritic structure, the maximum at  $4.3 \text{ \AA}$  was assigned to distance between non-hydrogen bonded adjacent hydroxyl oxygen atoms (Figure 26\*), and the maximum at  $4.8 \text{ \AA}$  represented correlations between non-hydrogen bonded adjacent hydroxyl oxygen atoms in which one of the hydroxyls was involved in a H-bond (Figure 26\*\*). Structural correlations unrelated to hydrogen bonding were expected in pair correlation functions for the dendritic species since more than half of the oxygen atoms were not H-bonded, whereas for water, because the majority of oxygen atoms were hydrogen bonded,  $g(r)_{OO}$  mostly represented correlations related to hydrogen bonding. Because the coordination shells in  $g(r)_{OO}$  of analogous hydrogen bonding systems such as water, represented the displacements of the first, second, and third neighbors within the clusters,<sup>24, 26, 33</sup> it was hypothesized that the center of the first ( $2.8 \text{ \AA}$ ), second ( $4.6 \text{ \AA}$ ), and third ( $6.3 \text{ \AA}$ ) coordination shells in the dendritic  $g(r)_{OO}$  functions corresponded to the first, second, and third nearest oxygen neighbors within a chain-like-cluster (Figure 25).



Table 2

*O-O neighbor analysis of chain-like clusters for D20 and D40: Average number of nearest neighbors (count) and average displacement between nearest neighbors according to neighbor number,  $n_i$*

$n^{\text{th}}$ neighbor, $n_i$	D20		D40	
	Count (#)	Displacement (Å)	Count (#)	Displacement (Å)
1	505	$2.8 \pm 0.2$	466	$2.8 \pm 0.2$
2	202	$4.6 \pm 0.8$	177	$4.6 \pm 0.8$
3	83	$6 \pm 1$	70	$6 \pm 1$
4	36	$7 \pm 2$	28	$7 \pm 2$
5	16	$9 \pm 2$	12	$9 \pm 2$
6	7	$10 \pm 3$	5	$10 \pm 3$
7	3	$11 \pm 3$	2	$11 \pm 3$

Note: Displacement represented the average over 1000 frames of the final trajectory file. Values were calculated from all types of oxygen atoms.

Table 3

*O-O neighbor analysis of chain-like clusters for H20 and H40: Average number of nearest neighbors (count) and average displacement between nearest neighbors according to neighbor number,  $n_i$*

$n^{\text{th}}$ neighbor, $n_i$	H20		H40	
	Count (#)	Displacement (Å)	Count (#)	Displacement (Å)
1	491	$2.8 \pm 0.2$	470	$2.8 \pm 0.2$
2	170	$4.6 \pm 0.9$	153	$4.5 \pm 0.9$
3	63	$6 \pm 1$	51	$6 \pm 2$
4	24	$7 \pm 2$	17	$7 \pm 2$
5	9	$9 \pm 2$	5	$8 \pm 2$
6	4	$10 \pm 3$	2	$9 \pm 3$
7	2	$12 \pm 3$	1	$11 \pm 3$

Note: Displacement represented the average over 1000 frames of the final trajectory file. Values were calculated from all types of oxygen atoms

This hypothesis was checked by directly calculating the average displacement between the first oxygen atom in the clusters and consecutive neighboring oxygen atoms,

through a custom-made program, ‘TracedNeighbors’ (Tables 2 and 3 and Figure 25). The definition of neighboring oxygen atoms is provided in Figure 25a. The first oxygen atom in the cluster was identified as the central oxygen atom (O\*). The first oxygen (O-1) adjacent to the central oxygen atom is defined as the first nearest neighbor. Similarly, the second oxygen adjacent to the central oxygen atom is defined as the second nearest neighbor, etc. The displacement between O\* and the first (O-1), second, (O-2), third (O-3), and  $n^{\text{th}}$  adjacent oxygen atoms was calculated using the x-y-z coordinates of each respective atom,  $displacement = \sqrt{(x_{O^*} - x_n)^2 + (y_{O^*} - y_n)^2 + (z_{O^*} - z_n)^2}$ , where the subscript  $n$  denotes the  $n^{\text{th}}$  nearest neighbor.

The average displacement of each nearest neighbor up to the 9<sup>th</sup> neighbor is shown in Table 2 for D20 and D40 and up to the 8<sup>th</sup> neighbor is shown for H20 and H40 is shown in Table 3, where each polymer displayed almost the same values. The displacement corresponding to the first, second, and third nearest oxygen atom neighbors, which is plotted in Figure 25b using double arrows, displayed good agreement with the first, second, and third coordination shells in the  $g(r)_{O-O}$  of the dendritic polymers and water. The agreement between the separate calculations of  $g(r)_{O-O}$  and nearest oxygen neighbors within the clusters, supported the hypothesis that the structural origin of the peak at  $2\theta \approx 30^\circ$  was caused by O-O correlations within the ordered chain-like clusters of hydrogen bonded O-H $\cdots$ O groups.

The shape of the clusters was probed for each simulated dendritic polymer system by calculating the coordination number,  $CN$ , for the first coordination shell from the respective  $g(r)_{O-O}$  functions in Figure 25,

$$CN = 4\pi\rho \int_0^{r^{\min}} r^2 dr g_{oo}(r) \quad (7)$$

where  $\rho$  is the number density, and  $r_{\min}$  is the location of the first minimum in the  $g(r)_{\text{O-O}}$  function.<sup>1</sup> The  $g(r)_{\text{O-O}}$  was multiplied by  $4\pi\rho r^2$  and plotted against  $r$ .<sup>34</sup> Integration of this function produced the running coordination number. Each dendritic polymer displayed an  $r_{\min}$  value of 3.85 Å, and corresponding coordination numbers of 2.52, 2.56, and 2.47, and 2.45 for D20, D40, H20, and H40 respectively. These values indicated that the oxygen atoms had on average two nearest neighbors and formed predominantly linear and cyclic hydrogen bonded clusters with little to no branching. The *CN* values supported the assumption made in the hydrogen bond script that a hydrogen bond donor could form only one hydrogen bond with an acceptor and vice versa. Since regular, unstructured fluids, such as liquid Argon, displayed many nearest neighbors, e.g. *CN* of liquid Argon was 12,<sup>35</sup> the dendritic polymers displayed properties more similar to hydrogen bonding fluids which exhibit few nearest neighbors, such as water and liquid HF. Because the coordination numbers for D20, D40, H20, and H40 were more similar to those observed for liquid HF, *CN*  $\approx$  2,<sup>30</sup> 2.1,<sup>29</sup> and 2.5,<sup>28</sup> it was concluded that the clusters observed in the dendritic systems were more similar to the linear clusters in liquid HF than the tetrahedral clusters of water, *CN*  $\approx$  4.1,<sup>23</sup> 4.7,<sup>1</sup> 4.67,<sup>25</sup> and 5.4.<sup>9</sup>

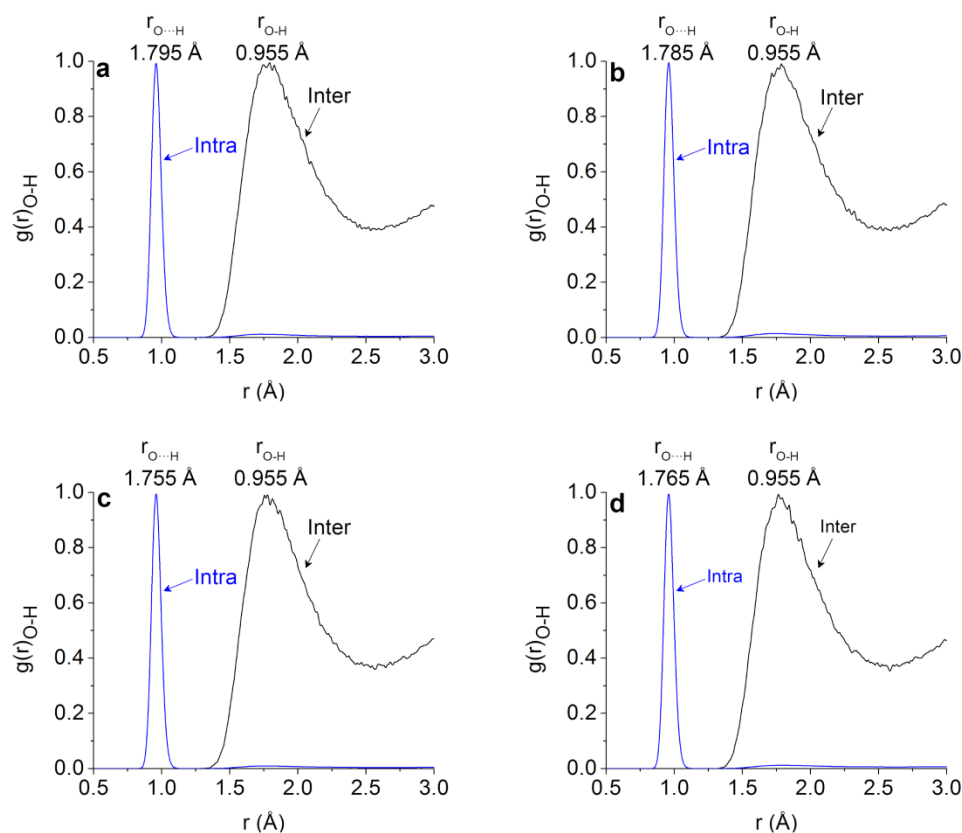


*Figure 27.* Normalized inter- and intramolecular pair correlation function for all oxygen atoms and hydroxyl hydrogen atoms,  $g(r)_{O-H}$ , for (a) D20, (b) D40, (c) H20, and (d) H40. The values for the H-bond length,  $r_{O...H}$ , and hydroxyl covalent bond length,  $r_{O-H}$ , are shown as the maxima of the inter- and intramolecular functions respectively.

The geometry of the clusters was probed from the normalized pair correlation function of all oxygen and hydroxyl hydrogen atoms,  $g(r)_{O-H}$ . The H-bond length ( $r_{O...H}$ ) and covalent hydroxyl bond length ( $r_{O-H}$ ) were calculated from the maxima of the inter- and intramolecular  $g(r)_{O-H}$  functions respectively (Figure 27). The  $r_{O...H}$  values calculated from the pair correlation function were all within error of the corresponding values from the H-bond script for each dendritic polymer. As compared with the  $r_{O...H}$  values from the H-bond script, reported above, the  $r_{O...H}$  values obtained from  $g(r)_{O-H}$  were more similar to the  $r_{O...H}$  values of liquid water,  $r_{O...H} \approx 1.83$ ,<sup>23</sup> 1.86,<sup>24</sup> 1.74,<sup>25</sup> 1.85,<sup>9</sup> 1.8 Å,<sup>26</sup> because the values reported for liquid water were also obtained from  $g(r)_{O-H}$ . Each dendritic

polymer displayed  $r_{\text{O-H}} = 0.955 \text{ \AA}$ , which was slightly smaller than the corresponding O-H covalent bond lengths observed in liquid water,  $r_{\text{O-H}} \approx 0.96,^{24} 0.98,^{25} 0.987,^{23}$  and  $0.992 \text{ \AA}.$ <sup>26</sup> Because the hydrogen bond length,  $r_{\text{O}\cdots\text{H}}$ , was slightly smaller, and covalent hydroxyl bond length,  $r_{\text{O-H}}$ , was slightly larger in liquid water than in the dendritic polymers, the hydrogen bonds in water were slightly stronger compared to those in the dendritic polymers.<sup>14</sup>

### Conclusions

A hydrogen bond organization common to both bis-MPA dendrimers and HBPs was elucidated in this chapter (R.O.1) through complementary experimental and simulation studies. Esterification of the hydroxyl end-groups of the fourth pseudo-generation hyperbranched polymer, H40, decreased hydrogen bond interactions of the system and showed that the peak at  $2\theta \approx 30^\circ$  in the X-ray scattering pattern was related specifically to ordering of hydroxyl end-groups. Computer simulations were performed on the second (D20) and fourth (D40) generation dendrimers, the analogous HBPs, H20 and H40 respectively, and a 100% acetylated fourth generation dendrimer (D40-CH<sub>3</sub>). The peak at  $2\theta \approx 30^\circ$  was observed in all of the simulated X-ray patterns of the hydroxylated dendritic polymers but not for the fully esterified dendrimer, D40-CH<sub>3</sub>, supporting that this peak was related to hydroxyl ordering. ‘Chain-like’ clusters of hydrogen bonded O-H $\cdots$ O groups were identified through a customized statistical hydrogen bond analysis in the final amorphous cell of each hydroxylated dendritic polymer where the O-O correlations within the clusters gave rise to the  $2\theta \approx 30^\circ$  reflection in the X-ray pattern, corresponding to a d-spacing of approximately 0.3 nm.

The hydrogen bond characteristics, such as H-bond length, angle, and amount, were quite comparable between D20, D40, H20, and H40. These clusters were composed of bent and moderately strong hydrogen bonds and were on average two hydrogen bonds in length, where a maximum chain length of seven hydrogen bonds was observed for each simulated dendritic polymer. Out of the four types of hydrogen bonds, OH...OH type bonds were the most prevalent followed by the C=O...OH bonds, and ester and ether hydrogen bonds contributed as a minority. The HBPs displayed a higher contribution of carbonyl, ester, and ether hydrogen bonds as compared to the perfect dendrimer. The generation number did not affect the degree of cluster formation considerably. The placement/distribution of end-groups in the structure slightly effected the type of H-bonding where the dendrimers, D20 and D40, formed slightly greater amount of clusters (length  $\geq 2$  hydrogen bonds), and the HBPs, H20 and H40, displayed a higher propensity to form single H-bonds.

Although the H-bonding network of the dendritic polymers was less extensive than that of liquid water, as approximately 45% of oxygen atoms participated in hydrogen bonding, H-bonded clusters of this kind represented a major H-bond mediated organization in the bulk structure, and may be directly related to physical properties such as the glass transition temperature. A detailed description of a H-bond mediated organization unique to the HBPs and related to the sharpening of the amorphous halo of the X-ray patterns, will be discussed in the subsequent chapter.

Remarkably, the 'chain-like' clusters of the bis-MPA dendritic polymers were reminiscent of those formed in small molecule structural fluids, such as water and liquid HF, showing more similarities to the linear, bent clusters of HF than to the tetrahedral

clusters of water. By identifying the H-bond organizations in these dendritic polymers, insight into H-bond arrangements of other globular macromolecules such as proteins may be gained, and applications that utilize H-bonding, particularly in biomedical field, may be improved.

#### References

1. Head-Gordon, T.; Hura, G. Water Structure from Scattering Experiments and Simulation. *Chem. Rev.* **2002**, *102*, 2651-2670.
2. Hult, A.; Johansson, M.; Malmström, E. Hyperbranched Polymers. *Adv. Polym. Sci.* **1999**, *143*, 1-34.
3. Malmström, E.; Johansson, M.; Hult, A. The effect of terminal alkyl chains on hyperbranched polyesters based on 2,2-bis(hydroxymethyl)propionic acid. *Macromol. Chem. Phys.* **1996**, *197*, 3199-3207.
4. Žagar, E.; Huskić, M.; Grdadolnik, J.; Žigon, M.; Zupančič-Valant, A. Effect of Annealing on the Rheological and Thermal Properties of Aliphatic Hyperbranched Polyester Based on 2,2-Bis(methylol)propionic Acid. *Macromolecules* **2005**, *38*, 3933-3942.
5. Žagar, E.; Huskić, M.; Žigon, M. Structure-to-Properties Relationship of Aliphatic Hyperbranched Polyesters. *Macromol. Chem. Phys.* **2007**, *208*, 1379-1387.
6. Rogunova, M.; Lynch, T. Y. S.; Pretzer, W.; Kulzick, M.; Hiltner, A.; Baer, E. Solid-state structure and properties of hyperbranched polyols. *J. Appl. Polym. Sci.* **2000**, *77*, 1207-1217.

7. Žagar, E.; Žigon, M. Aliphatic hyperbranched polyesters based on 2,2-bis(methylol)propionic acid—Determination of structure, solution and bulk properties. *Prog. Polym. Sci.* **2011**, *36*, 53-88.
8. Ball, P. Water: Water - an enduring mystery. *Nature* **2008**, *452*, 291-292.
9. Jedlovszky, P.; Brodholt, J. P.; Bruni, F.; Ricci, M. A.; Soper, A. K.; Vallauri, R. Analysis of the hydrogen-bonded structure of water from ambient to supercritical conditions. *The Journal of Chemical Physics* **1998**, *108*, 8528-8540.
10. Accelrys Software Inc., Theory: Classical simulation theory: Calculating properties: Correlation functions: Pair correlation function. In *Materials Studio Online Help*, Accelrys Software Inc.: San Diego, 2014.
11. Zarzycki, J., Structure of glass: Methods of study using radiation scattering. In *Glasses and the Vitreous State*, Cambridge University Press: New York, 1991; pp 76-93.
12. Accelrys Software Inc., Forcite: Theory in Forcite: Scattering. In *Materials Studio Online Help*, Accelrys Software Inc.: San Diego, 2014.
13. Accelrys Software Inc., Theory: Classical simulation theory: Calculating properties: Radius of gyration. In *Materials Studio Online Help*, Accelrys Software, Inc.: San Diego, 2014.
14. Desiraju, G. R. A Bond by Any Other Name. *Angew. Chem. Int. Ed.* **2011**, *50*, 52-59.
15. Žagar, E.; Grdadolnik, J. An infrared spectroscopic study of H-bond network in hyperbranched polyester polyol. *J. Mol. Struct.* **2003**, *658*, 143-152.



16. Socrates, G., *Infrared and Raman Characteristic Group Frequencies*. John Wiley & Sons, Ltd.: 2004.
17. Mourey, T. H.; Turner, S. R.; Rubinstein, M.; Fréchet, J. M. J.; Hawker, C. J.; Wooley, K. L. Unique behavior of dendritic macromolecules: intrinsic viscosity of polyether dendrimers. *Macromolecules* **1992**, *25*, 2401-2406.
18. Fréchet, J. M. J. Functional Polymers and Dendrimers: Reactivity, Molecular Architecture, and Interfacial Energy. *Science* **1994**, *263*, 1710-1715.
19. Turner, S. R.; Voit, B. I.; Mourey, T. H. All-aromatic hyperbranched polyesters with phenol and acetate end groups: synthesis and characterization. *Macromolecules* **1993**, *26*, 4617-4623.
20. Jeffrey, G. A., *An Introduction to Hydrogen Bonding*. Oxford University Press, Inc.: New York, 1997.
21. Steiner, T. The Hydrogen Bond in the Solid State. *Angew. Chem. Int. Ed.* **2002**, *41*, 48-76.
22. Maréchal, Y., The H<sub>2</sub>O Molecule in Liquid Water. In *The Hydrogen Bond and the Water Molecule*, Maréchal, Y., Ed. Elsevier: Amsterdam, 2007; pp 215-248.
23. Zeidler, A.; Salmon, P. S.; Fischer, H. E.; Neufeind, J. C.; Simonson, J. M.; Markland, T. E. Isotope effects in water as investigated by neutron diffraction and path integral molecular dynamics. *J. Phys.: Condens. Matter* **2012**, *24*, 284126.

24. Narten, A. H.; Thiessen, W. E.; Blum, L. Atom Pair Distribution Functions of Liquid Water at 25°C from Neutron Diffraction. *Science* **1982**, *217*, 1033-1034.
25. Soper, A. K.; Benmore, C. J. Quantum Differences between Heavy and Light Water. *Phys. Rev. Lett.* **2008**, *101*, 065502.
26. Silvestrelli, P. L.; Parrinello, M. Structural, electronic, and bonding properties of liquid water from first principles. *J. Chem. Phys.* **1999**, *111*, 3572-3580.
27. Chaplin, M. F., Water's Hydrogen Bond Strength. In *Water of Life: The Unique Properties of H<sub>2</sub>O*, Lynden-Bell, R. M., Morris, S.C., Barrow, J.D., Finney, J. L. & Harper, C.L.J., Ed. Taylor & Francis Group, LLC: Boca Raton, 2007.
28. Vallauri, P. J. R. Structural properties of liquid HF: a computer simulation investigation. *Mol. Phys.* **1998**, *93*, 15-24.
29. McLain, S. E.; Benmore, C. J.; Siewenie, J. E.; Urquidi, J.; Turner, J. F. C. On the Structure of Liquid Hydrogen Fluoride. *Angew. Chem. Int. Ed.* **2004**, *43*, 1952-1955.
30. Röthlisberger, U.; Parrinello, M. Ab initio molecular dynamics simulation of liquid hydrogen fluoride. *J. Chem. Phys.* **1997**, *106*, 4658-4664.
31. Friedrich, J.; Perlt, E.; Roatsch, M.; Spickermann, C.; Kirchner, B. Coupled Cluster in Condensed Phase. Part I: Static Quantum Chemical Calculations of Hydrogen Fluoride Clusters. *J. Chem. Theory Comput.* **2011**, *7*, 843-851.
32. Tanis, I.; Karatasos, K. Local Dynamics and Hydrogen Bonding in Hyperbranched Aliphatic Polyesters. *Macromolecules* **2009**, *42*, 9581-9591.

33. Maréchal, Y., Methods to Observe and Describe H-Bonds. In *The Hydrogen Bond and the Water Molecule*, Maréchal, Y., Ed. Elsevier: Amsterdam, 2007; pp 49-75.
34. Kreitmeir, M.; Bertagnolli, H.; Mortensen, J. J.; Parrinello, M. Ab initio molecular dynamics simulation of hydrogen fluoride at several thermodynamic states. *J. Chem. Phys.* **2003**, *118*, 3639-3645.
35. Stillinger, F. H.; Weber, T. A. Inherent pair correlation in simple liquids. *J. Chem. Phys.* **1984**, *80*, 4434-4437.

CHAPTER III  
PSEUDO-HEXAGONAL, HYDROGEN BOND-MEDIATED MESOPHASE  
FORMATION IN BIS-MPA HYPERBRANCHED POLYMERS

Abstract

A model was proposed outlining the spatial arrangements of the chain segments in bis-MPA HBPs which lead to a hydrogen bond mediated structural ordering phenomenon. Wide angle X-ray Diffraction (WAXD), FTIR spectroscopy, and differential scanning calorimetry (DSC) studies were combined to identify the packing structure of linear chain segments and explain how the structural order changed with temperature and time (R.O.2). High resolution synchrotron X-ray diffraction experiments were performed on the second and fourth generation Boltorn HBPs between 25-130°C, and the analogous change in hydrogen bonding with increasing temperature was characterized by FTIR spectroscopy of H40. Peak deconvolution of the high resolution synchrotron X-ray patterns revealed an additional narrow peak superimposed on the amorphous halo at intermediate temperatures. The structural origin of this narrow peak, representative of the structural ordering phenomenon in the bis-MPA HBPs, was assigned to a pseudo-hexagonal mesophase of cylindrically packed linear chain segments. The dynamics of the ordering process were revealed through DSC annealing experiments of H20 and H40 over a wide range of temperatures, specifically chosen to range from below  $T_g$  and span up to elevated temperatures where structural ordering was weakened. The observed thermodynamics and kinetics of mesophase formation were found to mimic those of three-dimensional crystals.

## Introduction

Briefly presented in Chapter I and described further in Chapter II, the experimentally observed sharp shape of the amorphous halo peak from the X-ray patterns of Boltorn HBPs was attributed to hydrogen bond driven structural ordering phenomenon specific to HBPs only. Evidence that the H-bonds in bis-MPA HBPs associate and form networks was first asserted by Månson's group.<sup>1</sup> Prior to rheological testing, the fifth-pseudo-generation Boltorn HBP was preheated to 160°C, which caused a disruption of the H-bond network. Network disruption was demonstrated by a change in the complex viscosity profile from shear-thinning for the non-preheated sample, to completely Newtonian after preheating. Zagar and coworkers then similarly observed a structural buildup through the formation of H-bonds during annealing as an increase in the complex viscosity over time.<sup>2</sup> These studies established that H-bond network formation could be manipulated via annealing, and was more extensive and formed faster for the second pseudo-generation than for the fourth.

Investigated further by DSC, the characteristic thermograms of annealed H20 and H40 samples displayed a broad endothermic peak above  $T_g$ , preceded by an exothermic peak at certain annealing conditions.<sup>2-4</sup> These transitions were not observed in either the perfect dendrimer or the end-group functionalized HBP indicating that H-bonding occurred between linear sequences specifically, and led to structural ordering of these otherwise amorphous HBPs. The exothermic peak was ascribed to the formation of H-bonds and the endothermic peak to the cleavage of H-bonds formed during annealing. A more thermally stable H-bond network was found to form at lower annealing temperatures and longer annealing times.

WAXD was instrumental in confirming this ordering phenomenon where the annealed X-ray patterns revealed a noticeable sharpening of the amorphous halo peak for Boltorn HBPs, attributed to formation of a H-bond network and the enhancement of structural ordering upon annealing, while the analogous fourth generation bis-MPA dendrimer proved insensitive to annealing treatments as it showed no change in the shape or intensity of its amorphous halo peak.<sup>2</sup> In Chapter II, the sharpness and intensity of the amorphous halo peak of Boltorn H40 decreased upon esterification, further connecting the sharp shape to hydrogen bonding interactions.

Although structural ordering was linked to hydrogen bonding of linear chain segments, as of yet, the spatial arrangements of atoms and/or molecules which would lead to such ordering have not been elucidated. Herein we utilize high resolution x-ray diffraction over a wide-temperature range to closely examine the nature of the amorphous halo peak, where it was hypothesized that the sharp nature was caused by an additional peak in the amorphous halo region. DSC annealing experiments were performed over a wider range of temperatures to understand the dynamics of ordering. Understanding the geometry and packing of chains/molecules that constitute this ordered phase will aid in tuning and/or enhancing the use of HBPs for potential smart-technology and self-healing applications.

## Experimental

### *Materials and Sample Preparation*

The Boltorn second, H20, and fourth, H40, pseudo-generation bis-MPA based hyperbranched polyesters were kindly donated by Perstorp Polyols Inc., Sweden. In abbreviation HX0, X denotes the pseudo-generation number. The theoretical molecular

weight of a hyperbranched polymer is equal to the molecular weight of the analogous perfect dendrimer. Therefore, the theoretical molecular weights of H20 and H40 were 1749 and 7323 g/mol, respectively. The molecular weights of H20 and H40 determined by SEC, as reported by Perstorp, were 2100 and 5100 g/mol, respectively. Perstorp reported 0.45 and 0.44 for the degree of branching (DB) of H20 and H40. The procedure followed to prepare thin sheets of H20 and H40 using the Carver Melt Press was detailed in Chapter II.

FTIR spectra were recorded at a resolution of  $4\text{ cm}^{-1}$  using a Bruker Tensor 37 FTIR spectrometer using the KBr pellet method. Spectra were collected in the mid-range. *Wide Angle X-ray Scattering (WAXD)*

Regular WAXD spectra were collected on a Rigaku Ultima III diffractometer, as described in Chapter II. Powdered samples were placed onto the sample stage and examined at angles from  $2\theta=1-60^\circ$  at a step rate of  $1^\circ/\text{s}$ . Quenched samples were prepared by heating to  $150^\circ\text{C}$  to erase thermal history, and subsequently quenching in liquid  $\text{N}_2$ . Annealed samples were prepared by first heating to  $150^\circ\text{C}$  to erase thermal history, followed by heating samples in an oven at the desired annealing temperature for 1 h, and finally quenching in liquid  $\text{N}_2$ .

Two-dimensional (2D) WAXS experiments were performed at the synchrotron X-ray beamline X27C at National Synchrotron Light Source (NSLS), Brookhaven National Laboratory (BNL). The wavelength of the incident X-ray was 0.1371 nm. The scattering angle was calibrated using silver behenate with the primary reflection peak at the scattering vector,  $q=(4\pi\sin\theta)/\lambda=1.076\text{ nm}^{-1}$ , where  $\theta$  is the half-scattering angle and  $\lambda$  is the wavelength. A MAR charge-coupled device (CCD) was used as detector and the

typical data acquisition time was 30 s. An Instec HCS410 hot stage equipped with a liquid-nitrogen cooling accessory was used for temperature-dependent X-ray experiments. One-dimensional (1D) WAXS curves were obtained by integrating the corresponding 2D patterns radially.

Peak deconvolution of the synchrotron X-ray patterns was conducted by PeakFit® (SeaSolve Software, Inc.) using the AutoFit Peaks I, Residual method. A slightly different protocol was employed for H20 than for H40. For H20, using the 25°C X-ray pattern, a linear progressive baseline and Savitsky-Golay smoothing of 1% was first applied to the raw data. Four ‘Gaussian-Lorentzian sum (area)’ peaks were manually fit to the spectra and then statistical fitting was performed until convergence of  $\chi^2$  to ten digits. The peak scan parameters obtained using the 25°C X-ray pattern were saved and used as the initial conditions for peak fitting of the 40, 60, 80, and 100°C X-ray patterns for H20, as well as for the initial conditions for peak fitting of the 25, 40, and 60°C X-ray patterns of H40. Deconvolution of the non-synchrotron data was conducted using a similar approach. The quenched H20 pattern was deconvoluted first and the scan parameters were saved and used as the starting conditions for the H20 annealed, and the H40 quenched and annealed patterns.

#### *Differential Scanning Calorimetry (DSC)*

Thermal analysis was conducted using TA Instruments DSC Q-100. The calibration was carried out using indium and sapphire standards. All samples were dried in a vacuum oven for at least 24 hours at 50°C prior to testing. Heating and cooling rates of 10°C·min<sup>-1</sup> were used over the entire temperature range. For examining the effect of annealing upon the thermal transitions, samples were first heated to 200°C to erase



thermal history and then cooled to the annealing temperature at  $30^{\circ}\text{C}\cdot\text{min}^{-1}$ , which was the maximum rate of the instrument. The samples were held at the annealing temperature for 1 h and subsequently quenched to  $-50^{\circ}\text{C}$  before heating scans were conducted at  $10^{\circ}\text{C}\cdot\text{min}^{-1}$ .

## Results and Discussion

### *Temperature-FTIR Spectroscopy Analysis*

FTIR spectra of Boltorn H40 collected between 25 and  $120^{\circ}\text{C}$  are shown in Figure 28. The broad and asymmetric hydroxyl stretching vibration ( $\nu\text{OH}$ ) near  $3400\text{ cm}^{-1}$ , and the carbonyl stretching vibration ( $\nu\text{C}=\text{O}$ ) near  $1733\text{ cm}^{-1}$  are highlighted in Figure 28. The frequency shift of each of these vibrations was plotted as a function of temperature (Figure 29) to monitor the change in H-bonding with increasing temperature. At  $25^{\circ}\text{C}$  hydrogen bonding was the strongest, indicated by the broadness, associated with different types of inter- and intramolecular hydrogen bonded hydroxyls,<sup>5,6</sup> and relative location of the  $\nu\text{O-H}$  band. As temperature increased, hydrogen bond interactions were weakened, as seen by the narrowing and blue-shift of  $\nu\text{O-H}$  band. Above  $80^{\circ}\text{C}$  the change in frequency of the  $\nu\text{O-H}$  band was marginal. Because free hydroxyls typically appear as a sharp band between  $3670\text{-}3580\text{ cm}^{-1}$  and have been reported at  $3560\text{ cm}^{-1}$  for Boltorn H40 specifically,<sup>5,6</sup> the shape and position,  $3517\text{ cm}^{-1}$ , of the  $\nu\text{O-H}$  band revealed that not all of the hydrogen bonds were destroyed at  $120^{\circ}\text{C}$ . The frequency of  $\nu\text{C}=\text{O}$  remained constant with temperature,  $1733\text{ cm}^{-1}$ , and jumped to  $1736\text{ cm}^{-1}$  at  $100^{\circ}\text{C}$ . Above  $100^{\circ}\text{C}$  the change in the frequency of  $\nu\text{C}=\text{O}$  was marginal. At  $120^{\circ}\text{C}$ , the relative position of  $\nu\text{C}=\text{O}$  suggested that some of the carbonyls were still hydrogen bonded as free carbonyls were observed near  $1741\text{ cm}^{-1}$  for Boltorn H40 specifically<sup>5</sup> and from Chapter II, H-

bonded carbonyls appeared near  $1732\text{ cm}^{-1}$  and blue-shifted to  $1741\text{ cm}^{-1}$  at 100% theoretical esterification where all hydrogen bonding was disrupted.

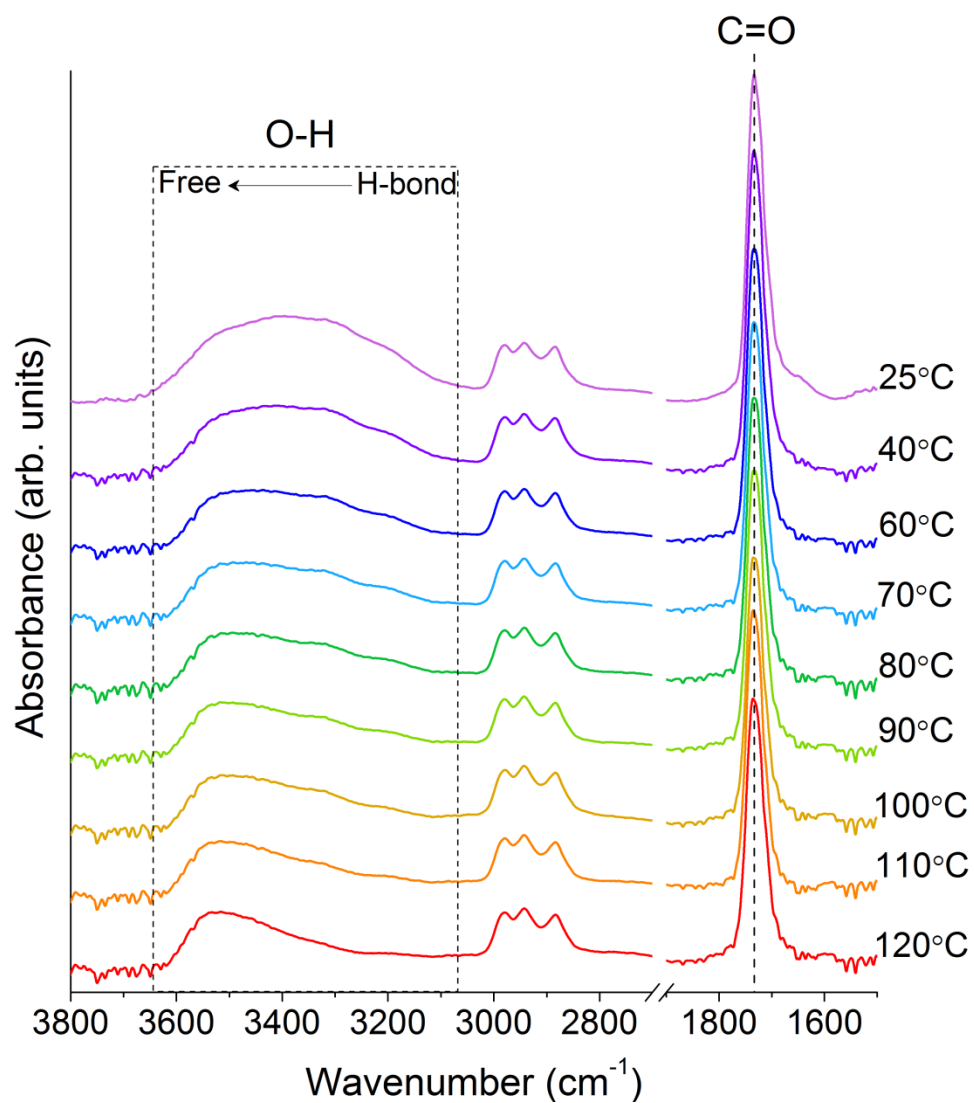


*Figure 28.* FTIR spectra for Boltorn H40 between 25-120°C. The curves were stacked vertically for clarity. The hydroxyl and carbonyl stretching vibrations are highlighted.

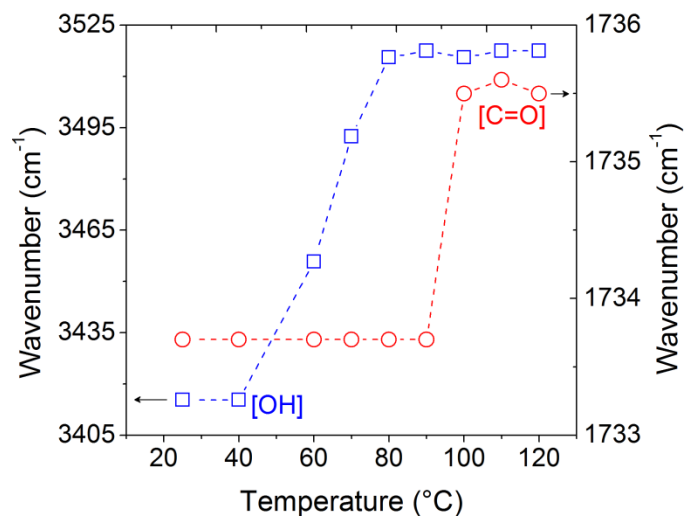
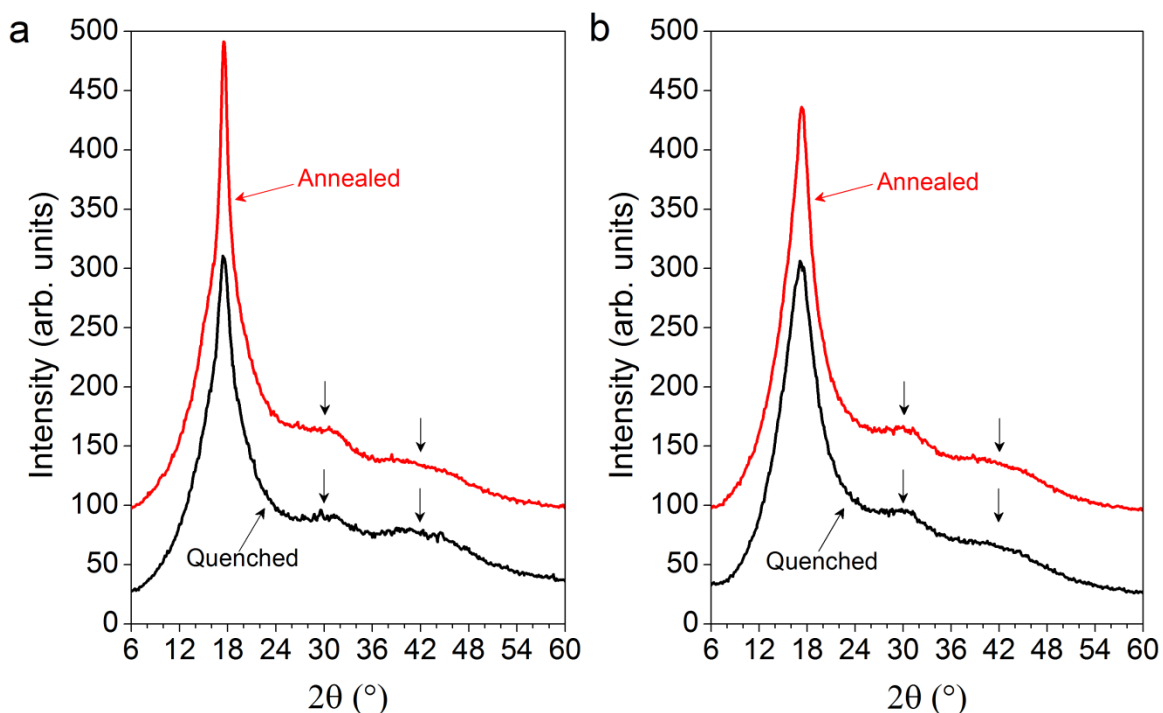


Figure 29. Frequency shift of hydroxyl (left axis) and carbonyl (right axis) stretching vibration as a function of temperature.

#### *X-Ray Diffraction of Boltorn HBPs*

Wide-angle X-ray diffraction patterns were obtained for the second and fourth pseudo-generation bis-MPA HBP samples which were either quenched from the melt or annealed at 60°C for 1 h (Figure 30). The patterns for each generation displayed three characteristic peaks, a sharp reflection at  $2\theta \approx 17^\circ$ , and two low intensity, broad reflections at  $2\theta \approx 30^\circ$  and  $42^\circ$ , which corresponded to d-spacing values of approximately 0.5, 0.3, and 0.2 nm respectively. The d-spacing, shape, and intensity of the reflections at  $2\theta \approx 30^\circ$  and  $42^\circ$  were relatively unaffected by annealing. Compared to the low intensity peaks, the reflection at  $2\theta \approx 17^\circ$  displayed somewhat unique behavior. After annealing, the d-spacing corresponding to  $2\theta \approx 17^\circ$  decreased by 1% and the shape and intensity also considerably changed for both H20 and H40. Closer examination of the reflection at  $2\theta \approx 17^\circ$  revealed that this peak was relatively broad towards the bottom, resembling an amorphous halo of a typical amorphous polymer, and narrower towards the top, somewhat reminiscent of a semi-crystalline polymer peak. This shape peculiarity was more pronounced for H20 than for H40 and intensified for each generation upon

annealing. The placement of two peaks, which may represent two distinct ordering phenomena, in the amorphous halo region was investigated further by higher resolution ( $\lambda=0.1371$  nm) synchrotron WAXD.



*Figure 30.* Wide-angle X-ray diffraction (WAXD) patterns of Boltorn (a) H20 and (b) H40. Samples were either quenched from the melt or annealed at 60°C for 1 h. The arrows highlight the low intensity peaks at  $2\theta \approx 30$  and  $42^\circ$ . The annealed curves were stacked vertically above the quenched ones.

Representative synchrotron X-ray diffraction patterns for H20, between 25-130°C, and H40, between 25-120°C, are shown in Figure 31. Similar to the non-synchrotron X-ray patterns, the synchrotron diffraction patterns for each generation and at each temperature, displayed a relatively intense reflection at  $2\theta \approx 15^\circ$  and two low intensity, broad reflections at  $2\theta \approx 26^\circ$  and  $35^\circ$ , with corresponding d-spacing values of approximately 0.5, 0.3, and 0.2 nm. Although the reflection at  $2\theta \approx 35^\circ$  was slightly truncated in width due to the limiting upper value of  $2\theta$ , preliminary synchrotron X-ray scattering patterns for H20, collected over a larger angular range,  $2\theta \approx 1-45^\circ$ ,

corroborated the existence of this peak (see Appendix, Figures 57 and 58). The peak at  $2\theta \approx 15^\circ$  corresponded to the amorphous halo region, the structural origin of the peak at  $2\theta \approx 26^\circ$ , discerned in Chapter II, was ascribed to the hydrogen bonded chain-like-clusters, and the structural origin of the peak at  $2\theta \approx 35^\circ$  was unclear. For both H20 and H40, as temperature increased, the reflection at  $2\theta \approx 15^\circ$  decreased in intensity, became broader, and shifted to higher values of  $2\theta$ , whereas the temperature dependence of the reflections at  $2\theta \approx 26^\circ$  and  $36^\circ$  was unclear from the diffractograms in Figure 31.

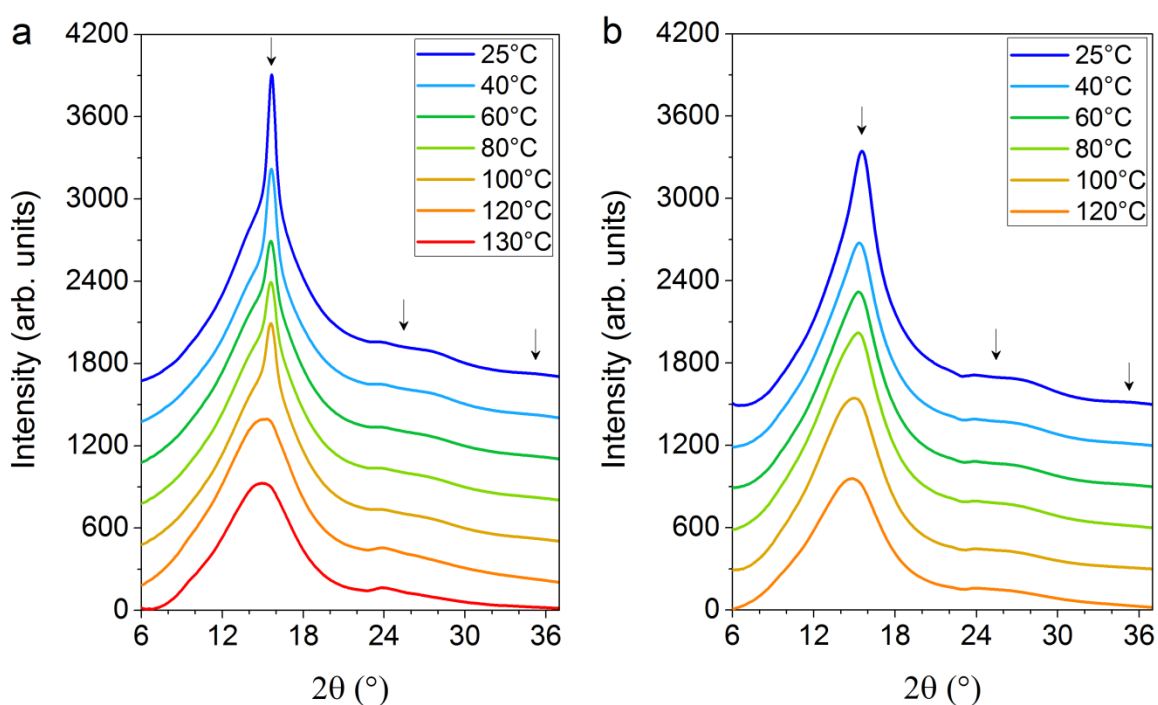


*Figure 31.* Synchrotron X-ray patterns ( $\lambda = 0.1371$  nm) for (a) H20 at 25, 40, 60, 80, 100, 120, and 130°C and (b) H40 at 25, 40, 60, 80, 100, and 120°C. Curves were shifted vertically for clarity where the upper-most curve corresponds to the lowest temperature and the lower-most curve corresponds to the highest temperature. The spacing between each curve is approximately 300 arb. units. The arrows indicate the main reflections.

In the X-ray patterns of H20 particularly, at temperatures between 25 and 100°C the reflection at  $2\theta \approx 15^\circ$  appeared to be composed of two peaks rather than just one, whereas above 100°C the  $2\theta \approx 15^\circ$  peak resembled a typical broad amorphous halo. Although this effect was less pronounced for H40, the reflection at  $2\theta \approx 15^\circ$  in the X-ray

patterns between 25 and 80°C was still quite narrow in shape, especially in comparison to broad amorphous halo at 120°C. Furthermore, the temperature range from FTIR spectroscopy where the change in frequency became marginal for both  $\nu\text{O-H}$  and  $\nu\text{C=O}$ ,  $T \approx 80\text{-}100^\circ\text{C}$ , corresponded to the temperatures from the H40 X-ray patterns where the amorphous halo shape transitioned from relatively narrow to broad, from 80 to 100°C. The narrow shape of the amorphous halo was accordingly linked to ordering related to hydrogen bonding of both  $\text{O-H}\cdots\text{O-H}$  and  $\text{O-H}\cdots\text{O=C}$  type associations. To investigate whether an additional peak, slightly shifted to the right of the amorphous halo, contributed to the overall sharp shape of the reflection at  $2\theta \approx 15^\circ$ , peak deconvolution of the synchrotron and the non-synchrotron X-ray patterns was conducted.

#### *Peak Deconvolution*

Deconvolution of the synchrotron X-ray data was only performed for patterns where four peaks were apparent, i.e. at temperatures where the amorphous halo appeared to be composed of two peaks or in the case of H40, had a sharp character. Thus, deconvolution was performed between 25-100°C for H20 and 25-60°C for H40. Although the amorphous halo in the 80°C X-ray pattern of H40 was narrow, the deconvolution was not included in this analysis due to the poor statistical fit. Shown in Figures 32 and 33 are the deconvoluted patterns for the synchrotron X-ray data at all temperatures for H20 and H40 respectively. The peak centered at approximately  $2\theta \approx 15^\circ$  was deconvoluted into two peaks, 'Peak 1' and 'Peak 2', and the two small, broad reflections at  $2\theta \approx 26^\circ$  and  $36^\circ$  were deconvoluted as 'Peak 3' and 'Peak 4' respectively. The deconvolution of H40 was less accurate because the precise placement of two peaks in the amorphous halo region was more difficult since the amorphous halo region was not

very sharp, as compared to that of H20, and two peaks were less easily discernable. For Peaks 1-4, shown in Tables 4 and 5 are the angular position, corresponding d-spacing, and intensity at each temperature for H20 and H40 respectively. The temperature dependence of the d-spacing and intensity of each deconvoluted peak for each generation is depicted in Figure 34.

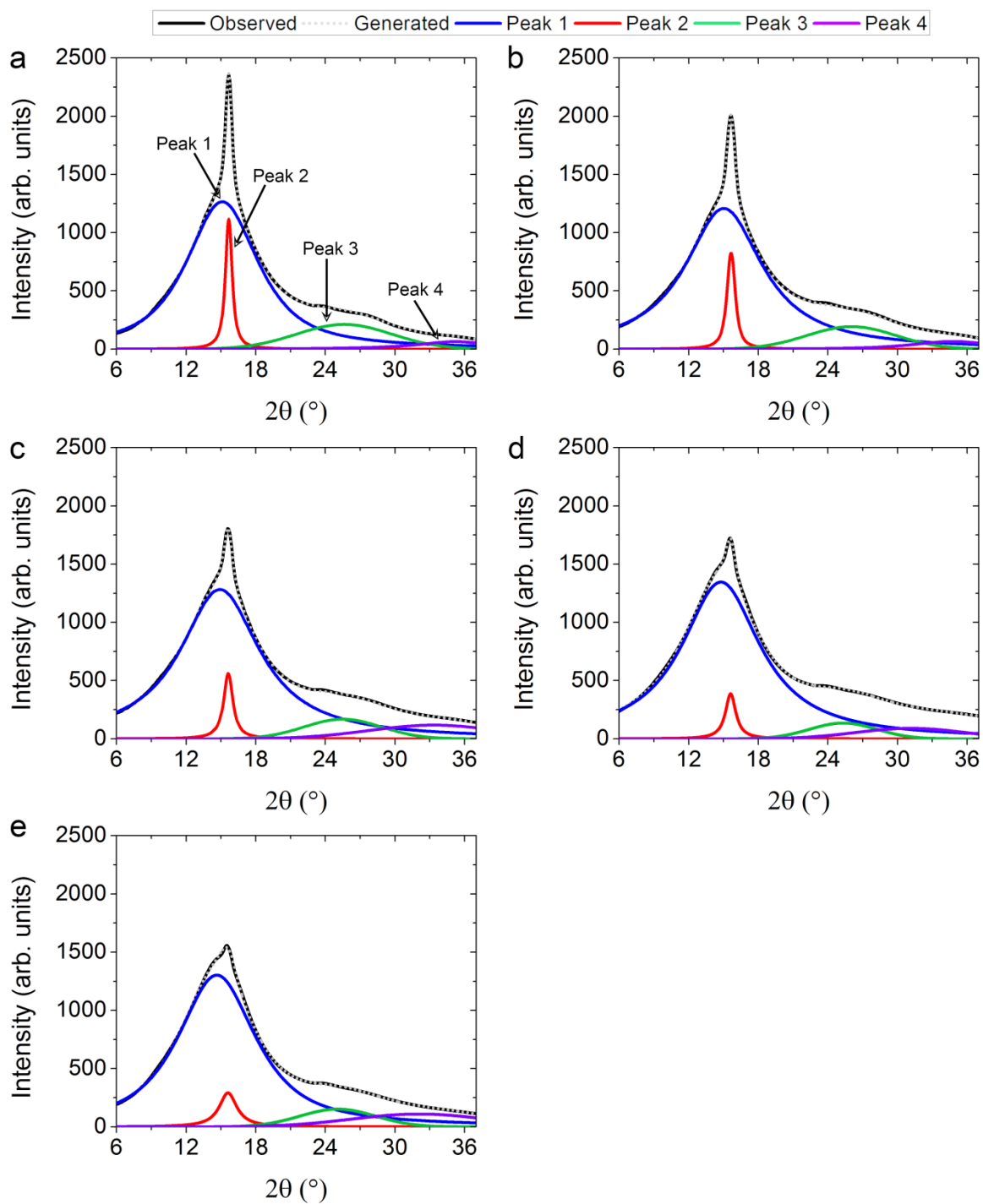


*Figure 32.* Peak deconvolution results for the synchrotron X-ray patterns of Boltorn H20 at (a) 25, (b) 40, (c) 60, (d), 80, and (e) 100°C. Each pattern was deconvoluted into four peaks: Peak 1 (blue), Peak 2 (red), Peak 3 (green), and Peak 4 (purple), indicated with arrows in (a).



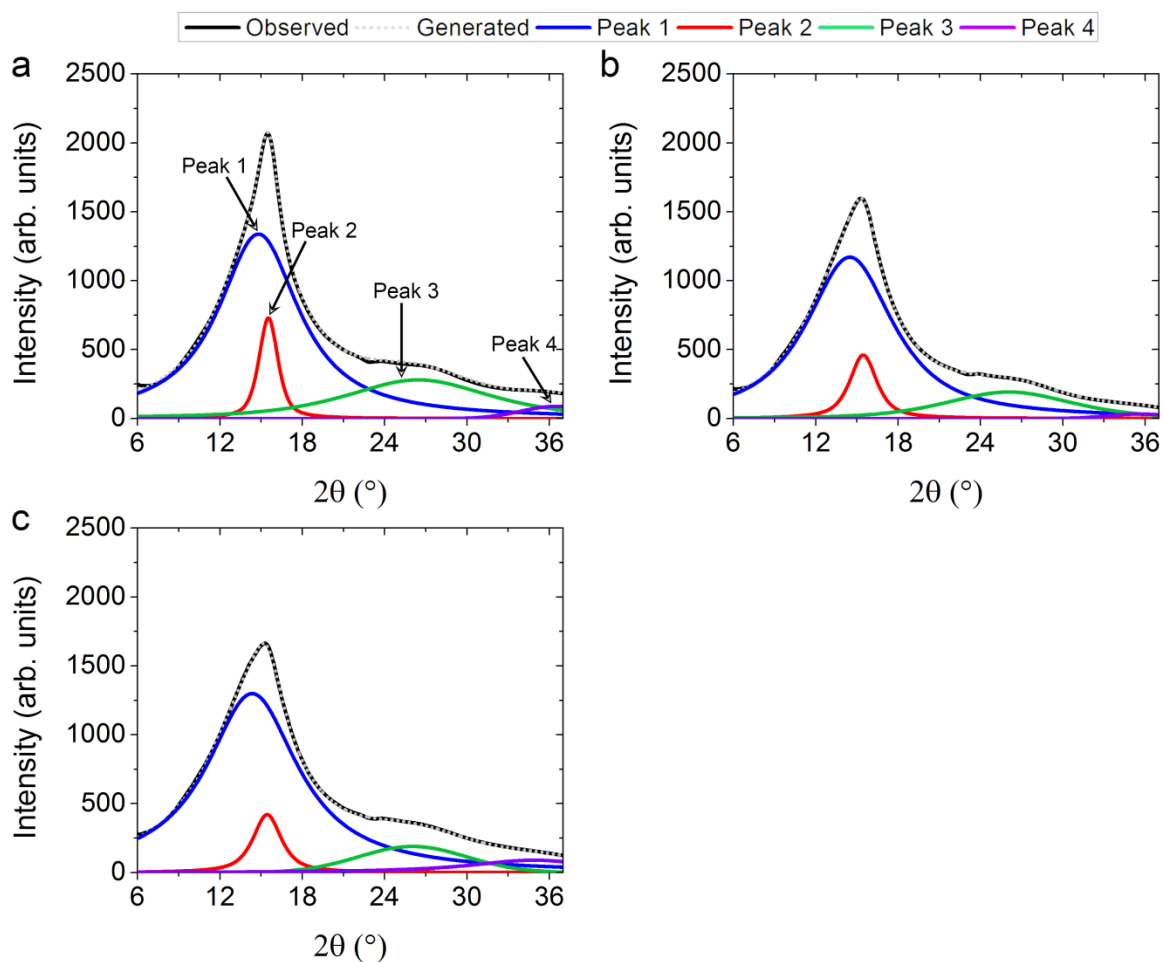


Figure 33. Peak deconvolution results for the synchrotron X-ray patterns of Boltorn H40 at (a) 25, (b) 40, and (c) 60°C. Each pattern was deconvoluted into four peaks: Peak 1 (blue), Peak 2 (red), Peak 3 (green), and Peak 4 (purple), indicated with arrows in (a).

Table 4

*Deconvolution results of the angular position ( $2\theta$ ),  $d$ -spacing, and intensity*

*corresponding to Peaks 1-4 from the synchrotron X-ray patterns of H20 at 25, 40, 60, 80 and 100°C*

Temp. (°C)	2θ (°)	Peak 1	
		d-spacing (nm)	Intensity (arb. units)
25	15.1	0.522	1266
40	15.0	0.524	1208
60	14.9	0.529	1282
80	14.8	0.532	1346

Table 4 (continued).

100	14.6	0.538	1330
<b>Peak 2</b>			
Temp. (°C)	2 $\theta$ (°)	d-spacing (nm)	Intensity (arb. units)
25	15.7	0.503	1117
40	15.7	0.503	828
60	15.6	0.504	562
80	15.6	0.505	388
100	15.6	0.505	292
<b>Peak 3</b>			
Temp. (°C)	2 $\theta$ (°)	d-spacing (nm)	Intensity (arb. units)
25	25.6	0.309	212
40	26.0	0.304	194
60	25.5	0.311	169
80	25.3	0.313	135
100	25.1	0.316	152
<b>Peak 4</b>			
Temp. (°C)	2 $\theta$ (°)	d-spacing (nm)	Intensity (arb. units)
25	35.2	0.227	65
40	34.7	0.230	66
60	33.3	0.239	118
80	31.1	0.247	90
100	32.4	0.246	125

Table 5

*Deconvolution results of the angular position (2 $\theta$ ), d-spacing, and intensity corresponding to Peaks 1-4 from the synchrotron X-ray patterns of H40 at 25, 40, and 60°C*

<b>Peak 1</b>			
Temp. (°C)	2 $\theta$ (°)	d-spacing (nm)	Intensity (arb. units)
25	14.7	0.535	1184
40	14.4	0.543	1129
60	14.5	0.546	1162
<b>Peak 2</b>			
Temp. (°C)	2 $\theta$ (°)	d-spacing (nm)	Intensity (arb. units)
25	15.5	0.508	857
40	15.4	0.511	553
60	15.4	0.511	466

Table 5 (continued).

---

<b>Peak 3</b>			
Temp. (°C)	2 $\theta$ (°)	d-spacing (nm)	Intensity (arb. units)
25	26.5	0.308	246
40	26.2	0.302	247
60	26.0	0.304	198

<b>Peak 4</b>			
Temp. (°C)	2 $\theta$ (°)	d-spacing (nm)	Intensity (arb. units)
25	36.2	0.221	60
40	37.4	0.219	59
60	35.8	0.223	35

---

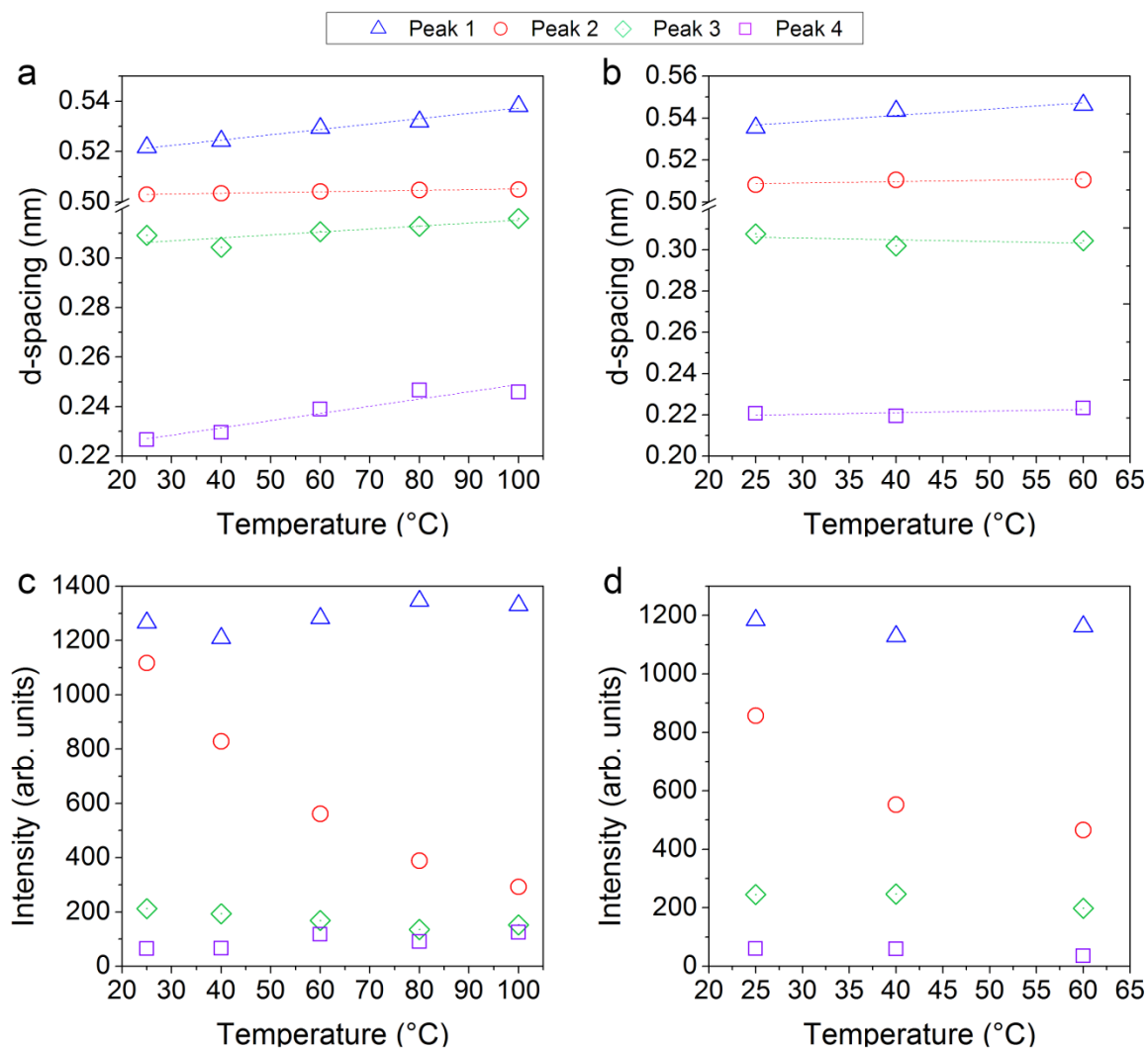


Figure 34. Change in d-spacing and intensity of Peaks 1-4 as a function of temperature for H<sub>2</sub>O (a) and (b), and H<sub>4</sub>O (b) and (d). All values were obtained from peak deconvolution.

The hypothesis proposed above was confirmed as the amorphous halo region was deconvoluted into two distinctly shaped peaks: Peak 1 and Peak 2. The broad shape of Peak 1 was indicative of the amorphous halo, representing short-range order between C-C and C-O close packed atoms in the bulk of the polymer.<sup>7</sup> A linear regression was fit to the d-spacing-temperature curves for H<sub>2</sub>O and H<sub>4</sub>O (Figure 34a,b) to calculate the thermal expansivity of the d-spacing, ( $E_{d_{sp}} = \delta d_{sp} / \delta T$ ). The  $E_{d_{sp}}$  values corresponding to Peak

1,  $(2.1 \pm 0.1) \times 10^{-4} \text{ nm} \cdot \text{K}^{-1}$  for H20 and  $(3 \pm 1) \times 10^{-4} \text{ nm} \cdot \text{K}^{-1}$  for H40, were positive and a magnitude larger than the corresponding  $E_{d_{sp}}$  values for Peak 2,  $(2.9 \pm 0.4) \times 10^{-5} \text{ nm} \cdot \text{K}^{-1}$  for H20 and  $(6 \pm 4) \times 10^{-5} \text{ nm} \cdot \text{K}^{-1}$  for H40. Furthermore, the  $E_{d_{sp}}$  values for Peak 1 were of the same order of magnitude as the volumetric thermal expansivity of Boltorn H20 and H40,  $(4.43 \pm 0.03) \times 10^{-4} \text{ cm}^3 \cdot \text{g}^{-1} \cdot \text{K}^{-1}$  and  $(3.99 \pm 0.01) \times 10^{-4} \text{ cm}^3 \cdot \text{g}^{-1} \cdot \text{K}^{-1}$  respectively, which will be presented in Chapter IV. The agreement between d-spacing thermal expansion and volumetric thermal expansion, as well as the relatively constant intensity of Peak 1 over the studied temperature range, supported that Peak 1 was the amorphous halo. The larger d-spacing of Peak 1 for H40 at each temperature, may have been related to the larger molecular weight of H40.

In comparison to Peak 1, Peak 2 was much narrower in shape. The overall sharp shape of the amorphous halo was due to the superimposition of Peak 2 onto Peak 1, where Peak 2 was related to the hydrogen bond-mediated ordering phenomenon of the HBPs. The relatively constant d-spacing (Tables 4 and 5 and Figure 34) indicated that the distance between linear chain segments within the ordered regions was not strongly affected by temperature. The relative amount of ordering was observed to decrease with increasing temperature, following the decreasing intensity of Peak 2, where Peak 2 was undetectable at elevated temperatures,  $T > 100^\circ\text{C}$  for H20 and  $T > 80^\circ\text{C}$  for H40. It was hypothesized that HBP structural ordering was reminiscent of the ordering observed for thermotropic liquid crystalline systems<sup>8,9</sup> since the linear chain segments, being only a few monomers in length, were quite short and may exhibit rigid behavior on small length scales,<sup>10-12</sup> were relatively straight and cylindrical in shape as compared to the branched dendritic regions, and participated in hydrogen bond-mediated ordering, which was stable

within a certain temperature range. This hypothesis was supported and expanded upon by comparison with the hydrogen bond forming linear polymer, nylon-6, which has been shown to form a pseudo-hexagonal  $\gamma$ -phase that, similar to Peak 2, appeared in the X-ray diffraction pattern as a narrow [001] reflection superimposed on the amorphous halo at intermediate temperatures and cooling rates.<sup>13-15</sup> The mesophase of nylon-6 was composed of parallel and straight but conformationally disordered chain segments with cylindrical symmetry and the H-bonding within these small domains was almost complete but not restricted to a specific crystallographic direction.<sup>13</sup> Based on the comparison with nylon-6, the following model was proposed to explain the structural ordering phenomena associated with the sharpness of the amorphous halo:

In the bis-MPA hyperbranched polyesters, pseudo-hexagonally packed, small aggregates of parallel and straight, but conformationally disordered linear chain segments with cylindrical symmetry may form at intermediate temperatures (i.e. temperatures above the  $T_g$  and below some ceiling temperature). Terminal units that are adjacent to linear units may participate but perhaps only as minor contributors to the ordering. The mesophase ordering was considered to be enthalpically driven by H-bonding and was restricted to two-dimensional order, rather than three-dimensional order observed in crystals (Figure 35).

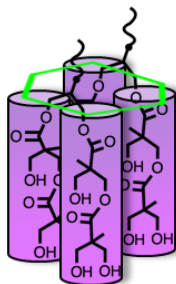


*Figure 35.* Schematic of the pseudo-hexagonal packing structure of linear chain segments which form mesophase aggregates in Boltorn hyperbranched polymers. The shape of each linear chain segment was approximated as cylindrical.

From the X-ray deconvolution it was observed that the lower pseudo-generation HBP, H20, displayed enhanced mesophase formation at each temperature, compared to the higher pseudo-generation HBP, H40. Due to a lower molar mass and shorter average chain length, H20 molecules may have higher mobilities than the larger H40 molecules, enabling faster mesophase formation of H20 during the considered time-scale. This molecular weight effect was observed for nylon-6 as well.<sup>13</sup> Steric considerations may also play a role in mesophase formation for dendritic polymers, where linear chain segments may be less accessible for ordering in the more crowded structure of H40.

Deconvolution of Peak 3, which corresponded to  $2\theta \approx 26^\circ$  and d-spacing  $\approx 0.3$  nm, shed some light on the temperature behavior of the ordered “chain-like-clusters.” As temperature increased, the d-spacing corresponding to Peak 3 increased by approximately 2% for H20, whereas the corresponding trend for H40 was unclear (from 25 to 40°C the d-spacing decreased by 2%, and from 40 to 60°C the d-spacing increased by 1%.) The observed increase in O-O distances within the clusters may have been caused by thermal expansion of the bulk polymer. Alternatively, the increase in d-spacing of Peak 3 along with the temperature may also have been due to a weakening of hydrogen bonding (Figure 1) with increasing temperature. Both H20 and H40 showed a slight decrease in

the intensity of Peak 3 with increasing temperature, approximately 28% for H20 and 19% for H40. The H-bonded clusters were accordingly prevalent even at higher temperatures, which was supported by FTIR spectra of Boltorn H40 (Figure 28) which indicated that even at 120°C, not all of the hydroxyl and carbonyl groups were free.

The broad shape of Peak 4 indicated a structural origin related to amorphous ordering. The deconvolution of Peak 4 was difficult because the synchrotron WAXD data was cut off at  $2\theta \approx 38^\circ$ . The change in d-spacing and intensity for Peak 4 showed similar trends as Peak 1. The intensity maxima for both generations were relatively constant over the temperature range, and the d-spacing values showed a positive linear trend with temperature, where the linear relationship was weaker for H40. For H20, the thermal expansivity of the d-spacing,  $E_{dsp}$ , of Peak 4,  $(2.92 \pm 0.51) \times 10^{-4} \text{ nm}\cdot\text{K}^{-1}$ , was similar to the  $E_{dsp}$  for Peak 1. To assess whether Peak 4 was the secondary reflection of Peak 1, the theoretical  $2\theta$  angle corresponding to the secondary reflection of Peak 1,  $n=2$ , was calculated using the d-spacing values for Peak 1 and the Bragg equation

$$2\theta_{\text{Peak4}} = 2 \sin^{-1} \left( \frac{\lambda}{d_{\text{Peak1}}} \right) \quad (8)$$

The observed  $2\theta$  values for Peak 4 (Tables 4 and 5) were ~4-16% larger, depending on temperature, than the theoretical values calculated from equation 1. This amount of deviation was expected because the amorphous halo region halo was quite broad and may have been composed of multiple atom pair correlations, i.e. C-C and/or C-O. Peak 4 was assigned as the secondary reflection of the amorphous halo.

After confirming the existence of a second peak in the amorphous halo region from the synchrotron X-ray analysis, the changes in the X-ray pattern upon annealing (Figure 30) were further investigated by deconvolution of the non-synchrotron WAXD



patterns. The final deconvoluted patterns of the non-synchrotron X-ray data for samples quenched from the melt, and samples annealed at 60°C for 1 h, are shown in Figure 36 for H20 and H40. Analogous to the peak assignments from the synchrotron deconvolution, the peak centered at approximately  $2\theta \approx 17^\circ$  was deconvoluted into two peaks, 'Peak 1' and 'Peak 2', and the two small, broad reflections at  $2\theta \approx 30^\circ$  and  $42^\circ$  were deconvoluted as 'Peak 3' and 'Peak 4' respectively. The angular position, corresponding d-spacing, and intensity of each peak at each condition (quenched vs. annealed) are shown in Tables 6 and 7 for H20 and H40 respectively.

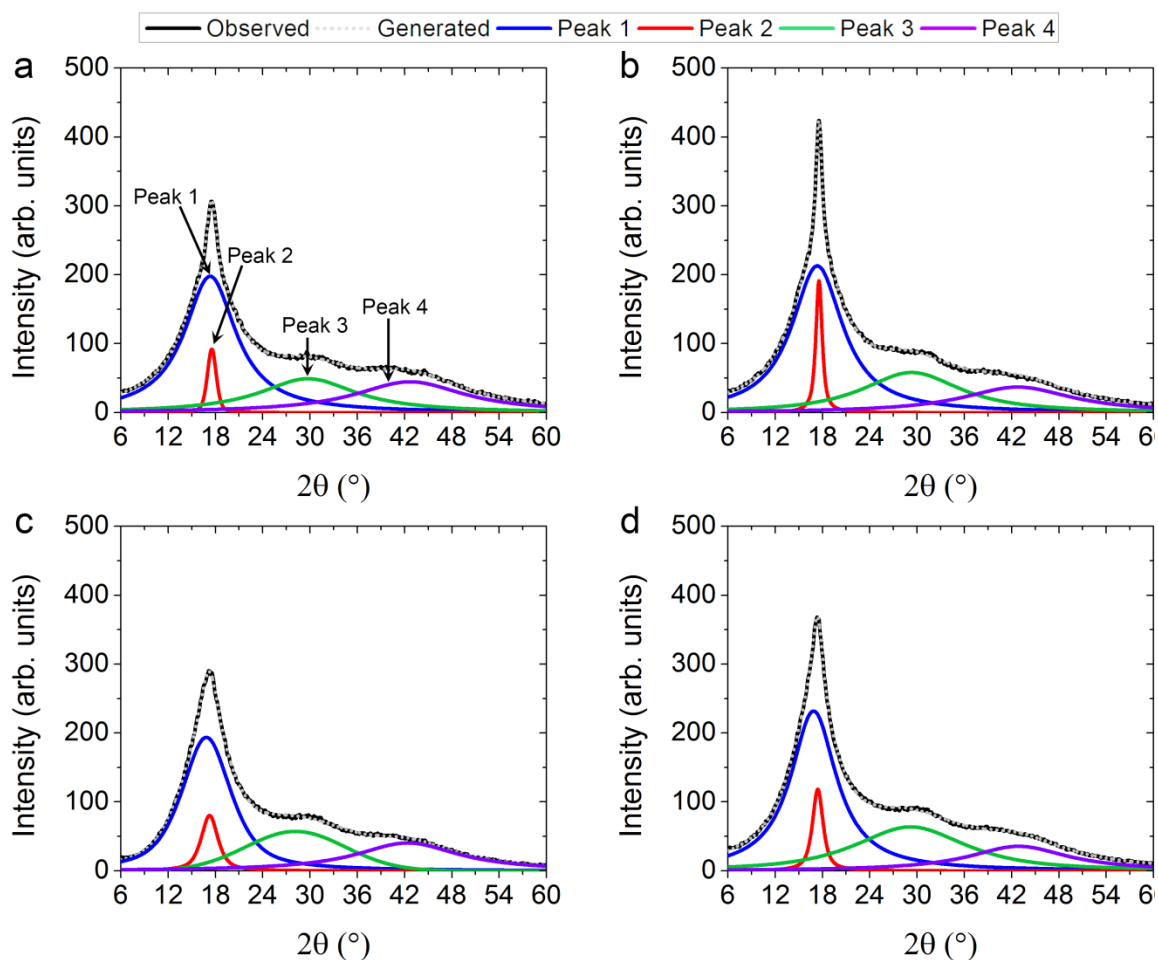


Figure 36. Peak deconvolution results for the non-synchrotron X-ray patterns of quenched (a) H2O and (c) H4O, and annealed (b) H2O and (d) H4O. Each pattern was deconvoluted into four peaks: Peak 1 (blue), Peak 2 (red), Peak 3 (green), and Peak 4 (purple), indicated with arrows in (a).

Table 6

*H2O deconvolution results of angular position ( $2\theta$ ),  $d$ -spacing, and intensity*

*corresponding to Peaks 1-4 for non-synchrotron quenched and annealed X-ray patterns*

<b>Peak 1</b>			
Treatment	$2\theta$ (°)	$d$ -spacing (nm)	Intensity (arb. units)
Quenched	17.3	0.513	198
Annealed	17.3	0.513	213
<b>Peak 2</b>			
Treatment	$2\theta$ (°)	$d$ -spacing (nm)	Intensity (arb. units)

Table 6 (continued).

Quenched	17.5	0.507	92
Annealed	17.6	0.504	192
<b>Peak 3</b>			
Treatment	2 $\theta$ (°)	d-spacing (nm)	Intensity (arb. units)
Quenched	29.7	0.301	49
Annealed	29.3	0.305	58
<b>Peak 4</b>			
Treatment	2 $\theta$ (°)	d-spacing (nm)	Intensity (arb. units)
Quenched	42.7	0.212	45
Annealed	42.8	0.211	37

Table 7

*H40 deconvolution results of angular position (2 $\theta$ ), d-spacing, and intensity*

*corresponding to Peaks 1-4 for non-synchrotron quenched and annealed X-ray patterns*

<b>Peak 1</b>			
Treatment	2 $\theta$ (°)	d-spacing (nm)	Intensity (arb. units)
Quenched	16.8	0.528	194
Annealed	16.8	0.528	198
<b>Peak 2</b>			
Table 7 (continued)			
Treatment	2 $\theta$ (°)	d-spacing (nm)	Intensity (arb. units)
Quenched	17.2	0.516	81
Annealed	17.4	0.510	141
<b>Peak 3</b>			
Treatment	2 $\theta$ (°)	d-spacing (nm)	Intensity (arb. units)
Quenched	28.1	0.318	57
Annealed	28.5	0.313	62
<b>Peak 4</b>			
Treatment	2 $\theta$ (°)	d-spacing (nm)	Intensity (arb. units)
Quenched	42.4	0.213	41
Annealed	42.9	0.211	36

Deconvolution confirmed that the shape and position of Peak 1, Peak 3 and Peak 4 did not change considerably after annealing for either generation (Tables 6 and 7). Each of these peaks displayed a small decrease in intensity after annealing, which was

negligible in comparison to the increase in intensity for Peak 2, 108% for H20 and 75% for H40. The amplification of the intensity was accompanied by an increase in the narrowness and a small decrease in d-spacing, 1%, of Peak 2. Thus, in light of the proposed model, annealing samples at 60°C increased the amount of the mesophase formation, and perhaps slightly decreased the spacing between linear chains within the mesophase aggregates.

#### *Differential Scanning Calorimetry of Boltorn H20 and H40*

The thermal behavior of the second and fourth pseudo-generation bis-MPA HBPs was investigated by DSC. Each sample was first heated to 200°C to erase thermal history after which (1) annealed samples were cooled to the respective annealing temperature,  $0 < T_a < 120^\circ\text{C}$ , held isothermally at for 1 h, and then cooled to  $-50^\circ\text{C}$  and (2) quenched samples were cooled to  $-50^\circ\text{C}$ . The second heating, taken as the final scan, was performed from  $-50^\circ\text{C}$  to  $200^\circ\text{C}$ . The final DSC scans of H20 and H40 for the first and second quenching and selected annealing temperatures are shown in Figure 37. The thermograms of H20 and H40 displayed a characteristic second-order step-transition at the glass transition temperature,  $T_g \approx 7^\circ\text{C}$  for H20 and  $T_g \approx 29^\circ\text{C}$  for H40, where the difference in  $T_g$  was due to the larger molecular weight of H40. Annealing and/or quenching the samples did not affect the  $T_g$  considerably. Above the glass transition, the DSC trace was dependent on thermal treatment. The observations of exo- and endothermic peaks in the DSC trace indicated that these HBPs may undergo a first-order transition above  $T_g$ .

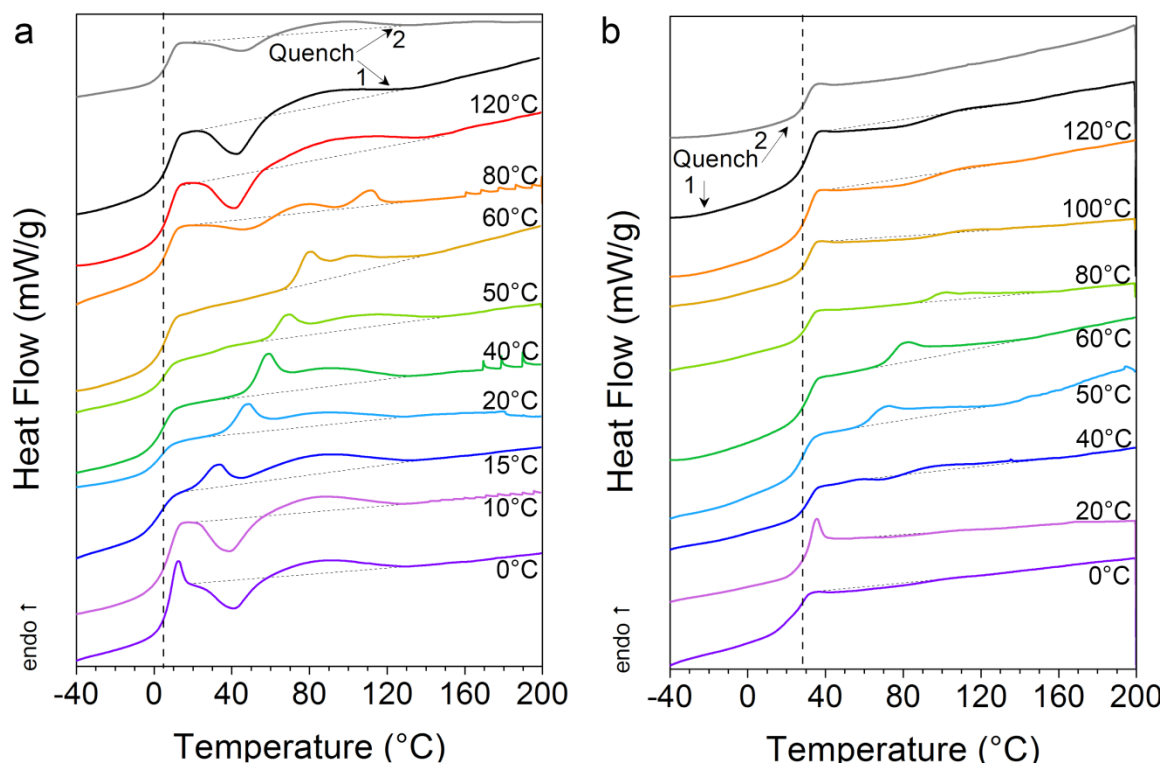
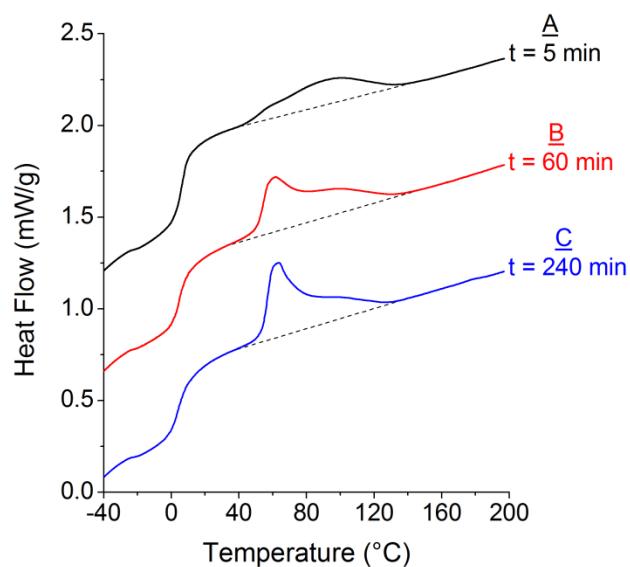


Figure 37. DSC thermograms for quenched and annealed samples of (a) H20 and (b) H40. Curves were stacked vertically for clarity. The annealing temperature ( $T_a$ ) is indicated next to each curve.

For each HBP, the samples which were annealed below  $T_g$  displayed an enthalpy overshoot on the second order step-transition in the DSC curves, 0°C for H20, 0 and 20°C for H40, which was caused by physical aging.<sup>16</sup> The first and second scans of the quenched samples, as well as samples annealed at 0, 10, 80, and 120°C for H20 and 100 and 120°C for H40, showed an exothermic peak followed by a broad endothermic peak which was bimodal at certain temperatures. Samples annealed between 15-60°C for H20 and 40-80°C for H40 did not show an exothermic peak but displayed an asymmetric, bimodal endothermic peak above the glass transition. The DSC trace for the H20 sample annealed at 80°C was particularly peculiar as a bimodal peak was observed after an exothermic peak. The bimodal endotherm in Figure 37 consisted of one narrower more intense peak and a broad peak. Although this bimodal endothermic peak has been

previously observed in the DSC thermograms of bis-MPA HBPs,<sup>2,4,17</sup> the structural origin of each peak within the endotherm has not been elucidated as of yet.

By considering the thermodynamics and kinetics of mesophase formation to be analogous to that of a crystalline system,<sup>18</sup> the peculiar nature of the DSC thermogram of the bis-MPA HBPs was explained. In the following description, the equilibrium melting temperature ( $T_m^\circ$ ) represents the temperature at which infinitely sized mesophase melts. The annealing process was regarded as being dynamic, roughly split into short-term and long-term events. When the Boltorn HBPs were quenched from 200°C to a respective annealing temperature ( $T_a$ ) below  $T_m^\circ$ , mesophase aggregates of different sizes with  $T_m > T_a$  (broad endothermic peak in Figure 38A), as well as embryos with  $T_m < T_a$ , were initially born as a result of the random fluctuations in the density of the liquid.<sup>19</sup> The embryos were not seen in the DSC trace. The initially born mesophase aggregates were observed experimentally as the relatively unimodal, broad endothermic peak shown in Figure 38A by annealing H20 for only 5 minutes at 40°C, representing short-term annealing. The thickness and melting temperature of the mesophase aggregates which were formed were dictated by the degree of undercooling,  $\Delta T = T_m^\circ - T_a$ .<sup>20</sup> Because the average radius of the initially born mesophase aggregates and the critical radius of the embryos was inversely proportional to the degree of undercooling, annealing at lower temperatures led to the formation of both mesophase aggregates and embryos of smaller sizes, as compared to annealing at higher temperatures. Experimentally, this was observed as a slight shift of the whole endothermic transition in the DSC trace to higher temperatures for higher annealing temperatures (Figure 37) and as the positive linear relationship between  $T_m$  and  $T_a$  (Figure 39).



*Figure 38.* DSC thermograms for Boltorn H20 annealed at  $T_a = 40^\circ\text{C}$  for (A) 5 min, (B) 60 min, and (C) 240 min. The curves were stacked vertically for clarity.

As annealing was continued, through the lateral attachment of additional linear chain segments embryos were transformed into mesophase aggregates with melting temperatures in the range of the respective annealing temperature and the initially born mesophase aggregates grew in size as well. The transformation of embryos into larger, stable mesophase aggregates was observed in the DSC trace of H20 and H40 as the narrow endothermic peak (Figure 37). Figure 38B displays the long term effects of annealing, during which stable embryos were converted into mesophase aggregates as evidenced by the emergence of a narrow endothermic peak at approximately  $62^\circ\text{C}$  at  $t = 60$  min. If annealing progressed for even longer times the embryos would presumably grow into even larger mesophase aggregates, shifting the narrow endothermic peak to even higher temperatures, which was observed in Figure 38C at  $t = 240$  min. For crystalline systems, this phenomenon is called lamellar thickening. Zagar and coworkers observed this phenomenon in an annealing study of Boltorn H40 where DSC

thermograms displayed a shift of the narrow endothermic peak to a higher melting temperature as annealing time increased from 4 to 48 hours.<sup>2</sup>

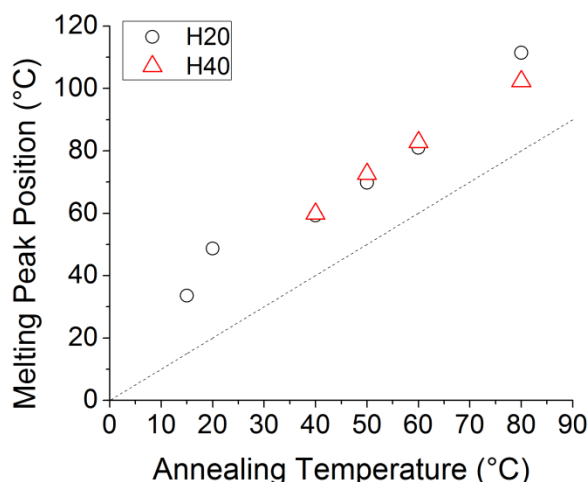


Figure 39. Melting temperature of mesophase aggregates ( $T_m$ ) as a function of annealing temperature ( $T_a$ ) for Boltorn H20 and H40.

For each annealed sample, the enthalpy of melting,  $\Delta H$ , was calculated ( $\Delta H = H_c - H_m$  where  $H_c$  and  $H_m$  are the enthalpy of crystallization and melting). By studying a wider range of annealing temperatures than previously reported,<sup>2,4</sup> a more complex relationship between  $\Delta H$  and annealing temperature was revealed. Shown in Figure 40, the enthalpy of melting values at each respective  $T_a$  indicated that the amount of mesophase formed was greater at lower annealing temperatures (for  $T_a > T_g$ ) and greatest at some critical  $T_a$ . This parabolic relationship was understood by considering the ‘mesophase-formation rate’ dependence on annealing temperature, where  $\Delta H$  was directly proportional to the rate. The rate of transformation of the Boltorn HBPs from the liquid phase to the mesophase was governed by two competing effects: the formation of mesophase aggregates, controlled by the degree of undercooling,  $\Delta T = T_m - T_a$ , and the diffusion or mobility of chain segments, which was dependent on the vicinity of  $T_a$  to  $T_g$ . If the rate was solely governed by the degree of undercooling then  $\Delta H$  would be greatest



at the lowest annealing temperature. However, when annealing at temperatures near or below  $T_g$ , all diffusive motion is frozen-in and chains lack mobility to form stable mesophase. Thus, as  $T_a$  was gradually increased above  $T_g$ , the HBP chains gained mobility, which increased the rate of mesophase formation, and analogously  $\Delta H$ . At some critical annealing temperature, the rate reached a maximum value and above this temperature the undercooling effect dominated, leading to decreasing rates of mesophase formation as  $T_a$  approached  $T_m^\circ$ . This phenomena was experimentally observed for the Boltorn HBPs, where for H20 by annealing immediately above  $T_g$ , for example at  $T_a = 20^\circ\text{C}$ ,  $\Delta H$  jumped from 0 to 13 J/g as chains gained mobility.  $\Delta H$  continued to increase up to a critical  $T_a$ ,  $40^\circ\text{C}$ . Then  $\Delta H$  decreased gradually in proportion to the decreasing degree of undercooling. At approximately  $T_a = 120^\circ\text{C}$ ,  $\Delta H \cong 0$ , indicating that this annealing temperature was close to the equilibrium melting temperature,  $T_m^\circ$ . Although less dramatic, this trend was also observed for the higher pseudo-generation, H40. The critical  $T_a$  for H40 (Figure 40) was  $60^\circ\text{C}$ , which was  $20^\circ\text{C}$  greater than that of H20 indicating that the critical annealing temperature may be related to the glass transition of each respective polymer.

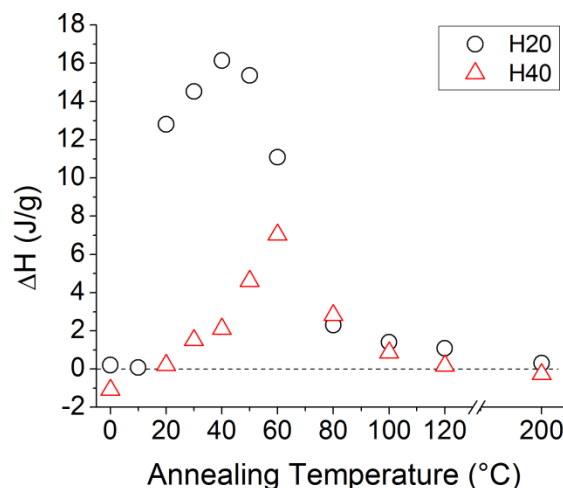


Figure 40. Enthalpy of melting of mesophase ( $\Delta H$ ) at each annealing temperature ( $T_a$ ) for Boltorn H20 (black) and H40 (red). The dashed lines represents  $\Delta H=0$ .

The values of  $\Delta H$  for each HBP were relatively low, similar to literature values reported for Boltorn H20 and H40,<sup>2,4</sup> and were comparable to the latent heat required for the liquid crystal to isotropic liquid transition, 8-30 J/g.<sup>21,22</sup> The annealing temperatures at which  $\Delta H > 0$  and the narrow endothermic peak was observed, corresponded to the temperatures from synchrotron X-ray diffraction that displayed a narrow peak, Peak 2, associated with the mesophase,  $25^\circ\text{C} \lesssim T \lesssim 100^\circ\text{C}$  for H20 and  $25^\circ\text{C} \lesssim T \lesssim 80^\circ\text{C}$  for H40, which supported that  $\Delta H$  represented the latent heat required to melt the mesophase. The exothermic peaks analogously represented the formation of the mesophase aggregates during the heating scan. The lower values of  $\Delta H$  for H40, as compared to H20, indicated that a lower amount of mesophase formed upon annealing at each respective temperature, which was in accordance with conclusions made from X-ray diffraction above.

Lastly, the special case of annealing H20 at  $80^\circ\text{C}$  where the peculiarly shaped DSC curve (Figure 37) displayed an exothermic peak followed by two endothermic peaks was explained. At  $80^\circ\text{C}$ , the rate of mesophase formation was relatively slow, and during

the timescale considered only a small amount of larger mesophase aggregates formed, as evidenced by a narrow endothermic transition at approximately  $T_m = 111^\circ\text{C}$ . Thus, a considerable population of linear chain segments was available for mesophase formation. During the heating scan, the available chains ordered at approximately  $45^\circ\text{C}$  (exothermic peak) and melted at approximately  $78^\circ\text{C}$  (endothermic peak) (Figure 37). The absence of an exothermic peak in the DSC traces of H20 corresponding to lower annealing temperatures suggested that most of the linear chain segments were either participating in mesophase ordering during the annealing process or existed as stable embryos.

### Conclusions

In this chapter, R.O.2 was accomplished as the spatial arrangement of HBP chain segments that led to structural ordering was identified and the dynamics of the ordering process upon annealing were explained. Through peak deconvolution of higher resolution X-ray patterns over a wide temperature-range, the sharp nature of the amorphous halo was attributed to an additional peak superimposed on to the amorphous halo, which was quite narrow in shape, representing a relatively ordered morphology. The structural origin of this peak was assigned to a temperature-dependent mesophase, similar to that of nylon-6, consisting of small cylindrical aggregates of pseudo-hexagonally packed, H-bonded linear chain segments. The dynamics of the annealing process was revealed by DSC experiments. The mesophase aggregates, consisting of a few laterally hydrogen bonded chains, formed two-dimensional crystals. The size of the aggregates, specifically the radius, increased upon annealing as additional chains attached laterally. The number of chains in a cylindrical aggregate varied, evidenced by the broadness of the endothermic peaks in the DSC thermograms which corresponded to a wide range of melting

temperatures, but the spacing between chains was relatively uniform. The interchain spacing of the mesophase for H20 molecules was ~1% smaller than that of H40. H20 displayed a larger amount of mesophase formation than H40 at each given temperature and time interval due to two effects: (1) more open structure and (2) higher chain and/or molecular mobility. While annealing considerably affected the formation of the mesophase it did not affect the formation of the “chain-like-clusters” of O-H...O groups. Furthermore, the variable temperature-X-ray patterns revealed that clusters were prevalent even at elevated temperatures, as evidenced by the appearance of the peak corresponding to a d-spacing of 0.3 nm even at 130°C.

#### References

1. Luciani, A.; Plummer, C. J. G.; Nguyen, T.; Garamszegi, L.; Månson, J.-A. E. Rheological and physical properties of aliphatic hyperbranched polyesters. *J. Polym. Sci. Part B: Polym. Phys.* **2004**, *42*, 1218-1225.
2. Žagar, E.; Huskić, M.; Grdadolnik, J.; Žigon, M.; Zupančič-Valant, A. Effect of Annealing on the Rheological and Thermal Properties of Aliphatic Hyperbranched Polyester Based on 2,2-Bis(methylol)propionic Acid. *Macromolecules* **2005**, *38*, 3933-3942.
3. Rogunova, M.; Lynch, T. Y. S.; Pretzer, W.; Kulzick, M.; Hiltner, A.; Baer, E. Solid-state structure and properties of hyperbranched polyols. *J.App. Polym. Sci.* **2000**, *77*, 1207-1217.
4. Žagar, E.; Huskić, M.; Žigon, M. Structure-to-Properties Relationship of Aliphatic Hyperbranched Polyesters. *Macromol. Chem. Phys.* **2007**, *208*, 1379-1387.

5. Žagar, E.; Grdadolnik, J. An infrared spectroscopic study of H-bond network in hyperbranched polyester polyol. *J. Mol. Struct.* **2003**, *658*, 143-152.
6. Socrates, G. *Infrared and Raman Characteristic Group Frequencies*; John Wiley & Sons, Ltd., 2004.
7. Alexander, L. E. Introduction to Diffraction By Polymers. in *X-Ray Diffraction Methods in Polymer Science*; Krieger: Huntington, NY, 196943-47.
8. Van Hecke, G. R. Thermotropic liquid crystals. A use of chemical potential-temperature phase diagrams. *J. Chem. Ed.* **1976**, *53*, 161.
9. Kato, T.; Fréchet, J. M. J.; Wilson, P. G.; Saito, T.; Uryu, T.; Fujishima, A.; Jin, C.; Kaneuchi, F. Hydrogen-bonded liquid crystals. Novel mesogens incorporating nonmesogenic bipyridyl compounds through complexation between hydrogen-bond donor and acceptor moieties. *Chem. Mater.* **1993**, *5*, 1094-1100.
10. Schmidt, M.; Paradossi, G.; Burchard, W. Remarks on the determination of chain stiffness from static scattering experiments. *Makromol. Chem., Rapid Commun.* **1985**, *6*, 767-772.
11. Mehraeen, S.; Sudhanshu, B.; Koslover, E. F.; Spakowitz, A. J. End-to-end distribution for a wormlike chain in arbitrary dimensions. *Phys. Rev. E* **2008**, *77*, 061803.
12. Yamakawa, H. Polymer Statistical Mechanics. *Annu. Rev. Phys. Chem.* **1974**, *25*, 179-200.
13. Cavallo, D.; Gardella, L.; Alfonso, G. C.; Portale, G.; Balzano, L.; Androsch, R. Effect of cooling rate on the crystal/mesophase polymorphism of polyamide 6. *Colloid Polym. Sci.* **2011**, *289*, 1073-1079.

14. Mileva, D.; Androsch, R.; Zhuravlev, E.; Schick, C. Morphology of mesophase and crystals of polyamide 6 prepared in a fast scanning chip calorimeter. *Polymer* **2012**, *53*, 3994-4001.
15. Mileva, D.; Kolesov, I.; Androsch, R. Morphology of cold-crystallized polyamide 6. *Colloid Polym Sci* **2012**, *290*, 971-978.
16. Echeverria, I.; Su, P.-C.; Simon, S. L.; Plazek, D. J. Physical aging of a polyetherimide: Creep and DSC measurements. *J. Polym. Sci. Part B: Polym. Phys.* **1995**, *33*, 2457-2468.
17. Žagar, E.; Žigon, M. Aliphatic hyperbranched polyesters based on 2,2-bis(methylol)propionic acid—Determination of structure, solution and bulk properties. *Prog. Polym. Sci.* **2011**, *36*, 53-88.
18. Keller, A.; Cheng, S. Z. D. The role of metastability in polymer phase transitions. *Polymer* **1998**, *39*, 4461-4487.
19. Muthukumar, M. Nucleation in Polymer Crystallization. in *Advances in Chemical Physics*, Vol. 128 (ed. Rice, S.A.), John Wiley & Sons, Inc.: Hoboken, NJ, 2003.
20. Marand, H.; Xu, J.; Srinivas, S. Determination of the Equilibrium Melting Temperature of Polymer Crystals: Linear and Nonlinear Hoffman-Weeks Extrapolations. *Macromolecules* **1998**, *31*, 8219-8229.
21. Chen, R. H. Thermodynamics for Liquid Crystals. in *Liquid Crystal Displays*; John Wiley & Sons, Inc.: Hoboken, NJ, 2011, pp 111-123.
22. Singh, S.; Dunmur, D. A. Physical Properties of Liquid Crystals. in *Liquid Crystals: Fundamentals*; World Scientific: River Edge, NJ, 2002, pp 57-91.

## CHAPTER IV

BULK VOLUMETRIC AND THERMODYNAMIC PROPERTIES OF BIS-MPA  
BASED DENDRIMERS AND HYPERBRANCHED POLYMERS

## Abstract

The bulk physical properties of the second and fourth generation dendrimers and HBPs based on a PP50 core and a bis-MPA monomer were experimentally probed and simulated atomistically. The effect of generation number and hydrogen bond-mediated structural ordering on bulk volume, free volume, and thermodynamic parameters was determined. PVT dilatometry was utilized to experimentally determine the bulk specific volume of Boltorn H20 and H40 at various temperatures and pressures, from which the thermal expansivity and compressibility were calculated. The average free volume hole-size ( $v_h$ ) as well as the number of holes was determined through positron annihilation lifetime spectroscopy (PALS). In the analysis of experimental V-T, V-P, and  $v_h$ -T behavior, specific attention was given to evidence of a first-order transition, related to the phenomenon of mesophase ordering (Chapter III). The absolute and fractional free and occupied volume was calculated using two different methods: Dlubek and Simha-Somcynksy (SS). Because the analogous perfect dendrimers were not experimentally available, MD simulations of the second and fourth generation dendrimers, D20 and D40, as well as H20 were performed to determine the free and occupied volume and relevant thermodynamic properties. Simulated properties were compared with the analogous experimental ones to evaluate the extent to which computer simulations can model the bulk, volumetric behavior of dendritic polymers.

## Introduction

The current understanding of structure-property relationships of highly branched, three-dimensional macromolecules is lacking, where only a few studies report the bulk volumetric and thermodynamic behavior of dendrimers,<sup>1,2</sup> and no such studies exist for HBPs. In solution, differences between the properties of dendrimers and linear polymers have been highlighted, where due to a lack of chain entanglements, dendrimers displayed Newtonian behavior under shear and lower solution and melt viscosities as compared to their linear counterparts.<sup>3,4</sup> Additionally, while linear polymers display a constant or monotonic increase in the intrinsic viscosity with molecular weight, dendrimers displayed a non-monotonic relationship due to a structural transition at generation 3-4.<sup>5,6</sup> In the bulk state, polybenzylether (PBE) dendrimers exhibited a similar structural transition, observed as the bulk modulus and coefficient of thermal expansion passing through a maximum value with increasing generation number.<sup>1</sup> The structure of HBPs then presents an even more complicated picture, being intermediate between that of linear polymers and perfect dendrimers. For example in solution, the intrinsic viscosity–MW behavior of HBPs was a hybrid of linear polymers and dendrimers. The dissimilar behavior of HBPs and dendrimers was accorded to a different relationship between mass-to-volume ratio and molecular weight. Dendrimers were hypothesized to show an equal increase in mass and volume with generation number,<sup>7</sup> while this relationship was relatively undefined for the HBPs.

The motion of molecules in amorphous structures is primarily dependent on the energy available for motion, and the open space for said molecule to move into.<sup>8</sup> Thus, free volume, on the macro and nanoscale, is a critical parameter in fundamentally



understanding all subsequent properties that depend on molecular motion, such as thermal behavior and relaxations involving localized and/or cooperative molecular movement. For several decades now, experimental techniques involving the annihilation of positrons with electrons have been used to investigate the nanoscale nature of the regions of free volume between molecules, or “holes,” which are present due to the structural disorder in materials. Most of these studies have been focused on linear polymers where only a few exist for dendrimers and HBPs. PALS can be used to measure the dimensions of such holes, giving a nanoscopic view of the free volume. The macroscopic volume can be measured by PVT dilatometry and in combination with PALS data, the number of holes and the total occupied and free volume can be calculated. PVT dilatometry records the specific volume as a function of temperature or pressure by means of a linear variable differential transducer (LVDT). The LVDT is attached to a bellows which encloses the sample cell. Thus, as a change in volume occurs, the bellows position moves accordingly. The Simha-Somcynsky equation of state (SS EOS) can be applied to the PVT data to determine a range of volumetric properties such as the free volume hole fraction ( $h$ ), occupied fraction ( $y$ ), as well as the free ( $V_f$ ) and occupied ( $V_{occ}$ ) volume as function of temperature. Providing a statistical model for liquid behavior over a wide temperature and molecular weight range, the SS EOS is based on the lattice hole theory which considers a macromolecular system consisting of  $N$   $n$ -mers each divided into  $s$  equivalent segments, where  $sM_s = nM_{rep} = M_n$  and  $M_s$  is the molar mass of each  $s$  segment,  $M_{rep}$  is the molar mass of a monomer repeat unit, and  $M_n$  is the number average molecular weight of the respective macromolecule. Each  $s$  segment represents an ‘occupied’ cell in the lattice, and the fraction of occupied lattice

sites is  $y$  and the remaining empty sites are represented by the fraction,  $h = (1 - y)$ . The incorporation of empty lattice sites introduces a degree of disorder into the crystal-like cell structure. The 6-12 Lennard-Jones (L-J) potential approximates intersegmental, or non-bonded, interactions, which are described by a maximum attraction energy (minimum in the potential energy plot),  $\epsilon^*$ , and a repulsion or hard-core volume,  $v^*$ . The SS theory assumes random mixing and employs the Flory-Huggins approach for configurational entropy calculations.<sup>9</sup> By differentiating the Helmholtz free energy at thermodynamic equilibrium, the SS EOS is yielded in the form of two coupled equations, which are solved simultaneously

$$\tilde{P}\tilde{V}/\tilde{T} = \left[ 1 - y \left( 2^{\frac{1}{2}} y \tilde{V} \right)^{-\frac{1}{3}} \right]^{-1} + y/\tilde{T} \left[ 2.002(y\tilde{V})^{-4} - 2.409(y\tilde{V})^{-2} \right] \quad (9)$$

$$3c \left[ \left( 2^{-\frac{1}{6}} (1/y\tilde{V})^{\frac{1}{3}} \right) / \left( 1 - 2^{-\frac{1}{6}} y (1/y\tilde{V})^{\frac{1}{3}} \right) - y (1/y\tilde{V})^2 (3.033 (1/y\tilde{V})^2 - 2.409/6\tilde{T}) \right] + (1 - s) - s \ln(1 - y)/y = 0 \quad (10)$$

where  $\tilde{P} = P/P^*$ ,  $\tilde{V} = V/V^*$ , and  $\tilde{T} = T/T^*$  are the reduced variables, and  $P^*$ ,  $V^*$ , and  $T^*$  are the scaling parameters.<sup>10</sup> For longer macromolecular chains,  $s \Rightarrow \infty$  and therefore, it is typically assumed that  $3c/s \Rightarrow 1$ . The scaling parameters are defined as follows

$$\left. \begin{aligned} P^* &= zq\epsilon^*/sv^* \\ T^* &= zq\epsilon^*/Rc \\ V^* &= v^*/M_s \end{aligned} \right\} (P^*V^*T^*)/M_s = Rc/s \Rightarrow R/3 \quad (11)$$

where  $R$  is the universal gas constant. At ambient pressure, and in the temperature range  $\tilde{T} = 0.016 - 0.071$ , a common simplification of the universal interpolation expression can be used to determine the scaling parameters

$$\ln \tilde{V} = a_0 + a_1 \tilde{T}^{\frac{3}{2}} \quad (12)$$

where  $a_0 = -0.10346$  and  $a_1 = -23.854$ .<sup>11</sup>

The SS theory has been mostly applied to linear polymer matrices at equilibrium (i.e. melt and/or liquid state), where the thermodynamics were dominated by chain entanglements.<sup>8,9,12-14</sup> In this way, the applicability of the SS theory to dendritic polymers, which may have different thermodynamic behavior than linear ones, is still questionable. To date, only one study reports the ability of the SS theory to accurately describe the PVT surface, thermal expansion coefficient, and compressibility coefficient of dendrimers in the bulk.<sup>2</sup> The SS theory has not been applied to simulated V-T data as of yet either.

The bulk physical properties of bis-MPA dendritic polymers were probed and related to their hydrogen bond organizations as well as structure. The purpose of this study was to (i) characterize the bulk volumetric and thermodynamic properties of the second and fourth pseudo-generation bis-MPA HBPs in the melt state, (ii) determine the effect of hydrogen bond-mediated structural ordering on macro- and nanoscale volumetric and/or thermodynamic properties, (iii) simulate bulk volumetric and thermodynamic properties of the second and fourth generation dendrimers D20 and D40, as well as the analogous second pseudo-generation HBP, H20, and (iv) evaluate the ability of the SS theory to predict free volume in HBPs, especially where structural ordering was prevalent.

## Experimental

### *Materials*

The Boltorn second, H20, and fourth, H40, pseudo-generation bis-MPA based hyperbranched polyesters were kindly donated by Perstorp Polyols Inc., Sweden. In

abbreviation HX0, X denotes the pseudo-generation number. In addition to HX0 HBPs, throughout the text their perfect dendrimer analogous will be similarly designated as DX0. The theoretical molecular weights of D20 and D40 are 1749 and 7316 g/mol, respectively. The molecular weight of H20 and H40 determined by SEC and as reported by Perstorp, are 2100 and 5100 g/mol, respectively. Perstorp reported 0.45 and 0.44 for the degree of branching (DB) of H20 and H40. All received materials were dried under vacuum and stored in a desiccator prior to use. Thin film samples of Boltorn H20 and H40 were prepared by compression molding using a Carver Melt Press, where the procedure used was described in Chapter II.

#### *Pressure-Volume-Temperature (PVT) Dilatometry*

PVT dilatometry was utilized to determine the specific volume at variable temperature and pressure for Boltorn H20 and H40. A detailed description of the procedure was presented above in Chapter II.

#### *Positron Annihilation Lifetime Spectroscopy (PALS)*

The average free volume hole-size of Boltorn H20 and H40 over a wide temperature range was experimentally probed using PALS. Positrons ( $e^+$ ) are positively charged antiparticles of the electron, which undergo annihilation events when combined with electrons. In condensed materials such as polymers, free positrons undergo thermalization by inelastic collisions with the surrounding media to produce secondary electrons, which can form a bound positron-electron pair, positronium atom (Ps), of anti-parallel, para-positronium ( $p$ -Ps), and parallel, ortho-positronium ( $o$ -Ps) spin states. The  $o$ -Ps can pick off an electron with antiparallel spin, resulting in an average  $o$ -Ps lifetime of a few nanoseconds.<sup>14</sup> PALS measures the lifetime of positrons injected into a polymer

sample from a positron-emitting nucleus such as Na<sup>22</sup>. The lifetime ( $\tau_3$ ) of the long-lived o-Ps species is used to extract the average size of (spherical) holes

$$\tau_3 = \frac{1}{2} \left[ 1 - \frac{R}{R+d} + \frac{1}{2\pi} \sin \left( \frac{2\pi R}{R+d} \right) \right]^{-1} \quad (13)$$

where  $R$  is the average hole radius, and  $d = 0.1656$  nm is the empirically determined electron layer thickness. The average size of a free volume hole can then be calculated as  $v_h = 4/3\pi R^3$ . PALS experiments were conducted with a fast-fast coincidence system, described elsewhere.<sup>12,14,15</sup> Two cylindrical samples of each polymer, which were approximately 1 mm thick and 10 mm in diameter, were encased in aluminum foil and dried for at least 24 hours prior to testing. The Na<sup>22</sup> positron source was sandwiched between the two samples and placed in the sample chamber. All measurements were taken over an hour, obtaining a total of  $1 \times 10^6$  counts in each PALS spectrum. The PALS spectra were processed using PATFIT-88 software. The error associated with determining  $\tau_3$  values using this software was approximately  $\pm 2\%$ .

#### *Molecular Dynamics (MD) Simulations*

Three hydroxylated bis-MPA based dendritic systems were modeled, utilizing PP50 as a core molecule: (1) second generation perfect dendrimer, ‘D20,’ (2) fourth generation perfect dendrimer, ‘D40’; (3) second generation hyperbranched polymer, ‘H20’. The protocol utilized to simulate the final relaxed structures and volume-temperature curves for the bis-MPA dendritic polymers is detailed in Chapter II.

### Results and Discussion

The volume-temperature (V-T) curves for Boltorn H20 and H40, at  $p = 0$  and in the temperature range of 28-130°C, are compared in Figure 41. The V-T data were representative of the melt state behavior of each HBP as the glass transition temperature,

$T_g$ , of H20 and H40 was approximately 7 and 29°C respectively. At each temperature, H20 displayed a larger total specific volume than H40. The specific volume values of H20 and H40 were comparable to those of PBE dendrimers of similar molecular weight and at similar temperatures.<sup>1</sup> The average melt thermal expansivity,  $E_m = (\partial V/\partial T)_p$ , for each HBP was calculated as the slope of the linear regression of the V-T data. The melt expansivity of H20,  $(4.43 \pm 0.03) \cdot 10^{-4} \text{ cm}^3/\text{K}$  was approximately 10% greater than that of H40,  $(3.99 \pm 0.01) \cdot 10^{-4} \text{ cm}^3/\text{K}$ , indicating that the lower generation HBP had greater translational mobility than the higher generation HBP above  $T_g$ . The  $E_m$  values of the Boltorn HBPs were on the same order of magnitude as various linear polymers,<sup>8,16-20</sup> but lay on the lower end of the spectrum perhaps due to their extensive H-bonding through the chain-like-clusters (Chapter II).

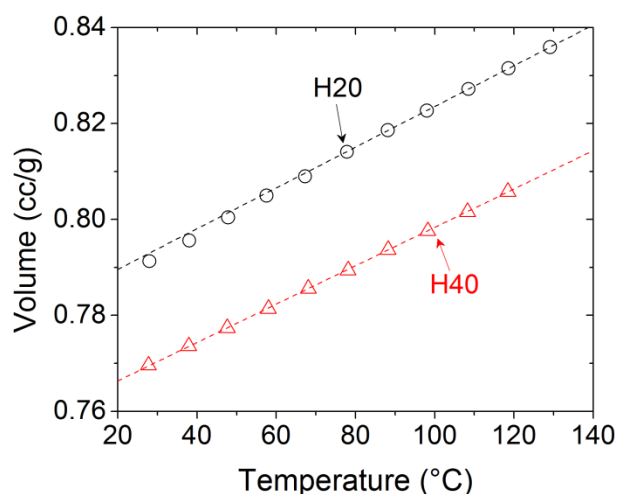


*Figure 41.* Experimental volume-temperature curves for Boltorn H20 and H40 at  $p = 0$ . The dashed lines represent the linear fit of the volume at the four highest temperature points. The linear fit was extrapolated over the entire temperature range.

The macroscopic V-T behavior was analyzed for evidence of a first-order transition related to mesophase ordering, which was observed as the endothermic peak in the DSC traces of Boltorn H20 and H40 (Chapter III). Because the enthalpy of melting,  $\Delta H$ , of the mesophase was relatively small as compared to  $\Delta H$  for crystalline polymers,<sup>21-</sup>

<sup>24</sup> and a range of melting temperatures were observed from DSC, it was unclear whether the mesophase-to-liquid transition would appear in the macroscopic volumetric data. At  $p=0$ , the V-T data from Figure 41 did not indicate the presence of a first-order transition, since a discontinuity in volume was not detectable for either generation in the examined temperature range. The thermal expansion coefficient,  $\alpha_m = (1/V)(\partial V/\partial T)_p$ , was calculated to determine whether the formation of mesophase affected higher derivatives of the free energy. The first derivative of a binomial fit of the V-T data was normalized by the volume at each temperature to yield  $\alpha_m$ . Shown in Figure 42,  $\alpha_m$  was relatively constant with temperature for H40, which has been observed for other dendritic polymers.<sup>1,2</sup> The  $\alpha_m$  values of H20 however anomalously displayed a negative correlation with temperature. The negative correlation of  $\alpha_m$  with temperature may have been caused by the greater driving force for mesophase formation at lower temperatures as compared to higher temperatures. The higher thermal expansion of H20 at lower temperatures was representative of a small densification of volume, which was shown by extrapolating a linear regression of the four highest temperature volume points over the entire temperature range. The regression was fit between 98-130°C for H20 and 88-118°C for H40, because in these respective regions mesophase formation was relatively negligible ( $\Delta H \approx 0$ , Chapter III). For H40, the extrapolated fit was in good agreement with the experimental data indicating that macroscale volume was not considerably affected by mesophase formation. However for H20, the volume points between 28 and 48°C were slightly lower than the extrapolated fit, showing a small effect of mesophase formation on the bulk volume. Therefore, although evidence of a first order transition through a discontinuity in volume was not observed for either HBP in Figure 41, the

mesophase ordering was found to influence H20 at lower temperatures by slightly densifying volume and in turn affecting the second derivative of the Gibbs free energy,  $\alpha_m$ . Because the  $\Delta H$  values of H40 were even smaller than those of H20, it was concluded that the fraction of the bulk polymer that formed mesophase in H40 was too small to detect at  $p=0$ .

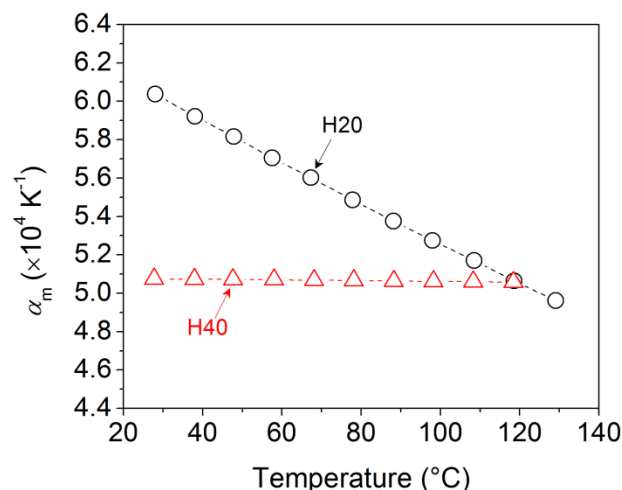


Figure 42. Melt state thermal expansion coefficient,  $\alpha_m$ , for H20 and H40 at  $p = 0$ .

The effect of increasing pressure on the volume and thermal expansion coefficients of H20 and H40 was also assessed. V-T curves for H20 and H40 between 10-160 MPa, at each 10 MPa interval, are shown in Figure 43. For both H20 and H40, the volume was decreased as pressure was increased. While a change in  $T_g$  at higher pressures was undetectable for H20 in the analyzed temperature range, the  $T_g$  of H40 increased to approximately 39°C at 10 MPa and up to 48°C at 160 MPa shown in Figure 43. The thermal expansion coefficients were calculated for H20 and H40 at selected pressures of 10, 40 and 150 MPa shown in Figure 44. For H40,  $\alpha_m$  was calculated only above  $T_g$ . As the pressure was increased to 10 MPa, the  $\alpha_m$  values of H40 displayed a slight negative correlation with temperature, similar to the  $\alpha_m$  values of H20 at  $p=0$ . Both



H2O and H40 displayed a negative correlation between  $\alpha_m$  and temperature at each pressure. Increasing pressure may have induced more mesophase formation as molecules were in closer proximity to each other and linear chain segments could find each other more easily for ordering.

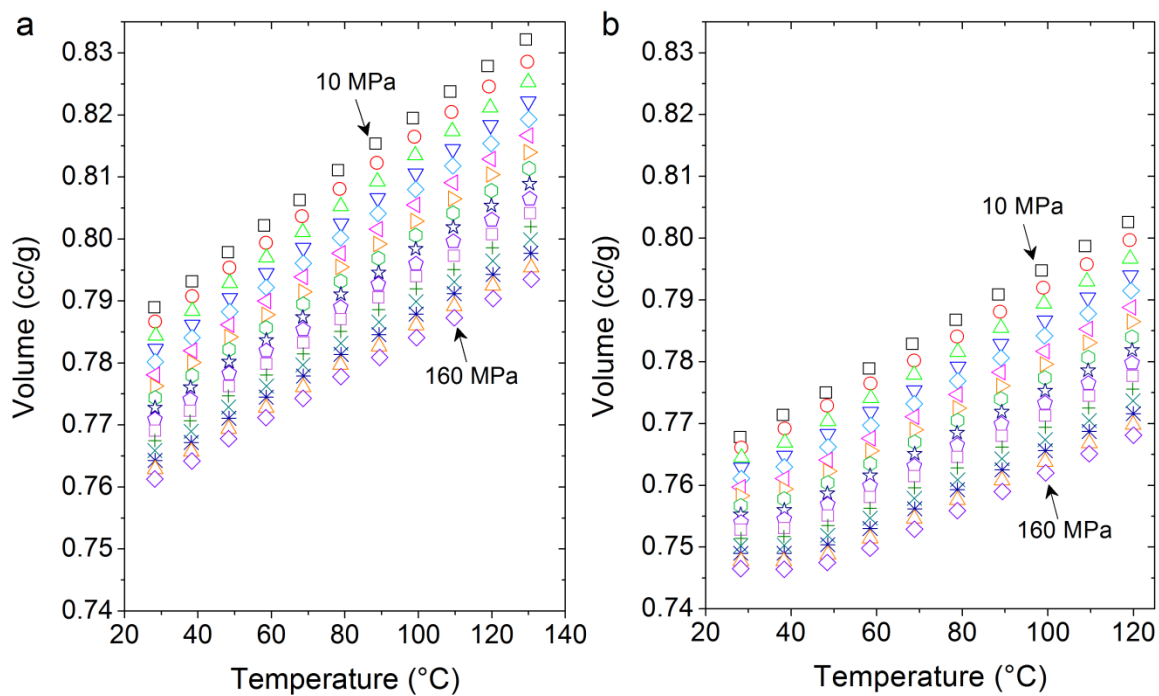


Figure 43. Isobaric volume-temperature curves at 10, 20, 30, 40, 50, 60, 70, 80, 90, 100, 110, 120, 130, 140, 150, and 160 MPa for Boltorn (a) H2O and (b) H40.

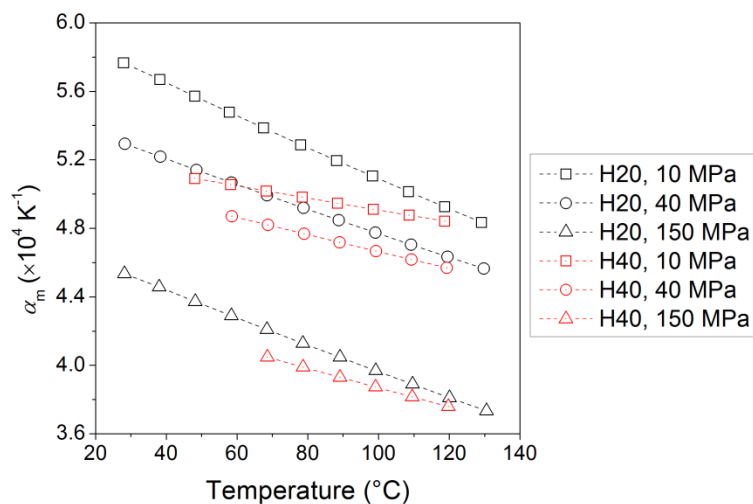


Figure 44. Temperature dependence of melt state thermal expansion coefficients,  $\alpha_m$ , for H2O and H40 at 10, 40, and 150 MPa.

The isothermal compressibility,  $\beta_m = (1/V)(\partial V/\partial P)_T$ , of H2O and H40 was determined by taking the first derivative of the binomial fit to the V-P data set, and normalizing by volume at each pressure. The compressibility values for H2O and H40 are plotted as a function of pressure at each temperature in the melt state (Figure 45a,b), as well as a function of temperature at  $p=0$  (Figure 45c). Compressibility decreased with increasing pressure, as lower free volume was available at higher pressures, and the compressibility was greater for H2O as compared to H40 at each temperature, indicating that the lower generation HBP, H2O, had greater free volume than the higher generation HBP, H40.

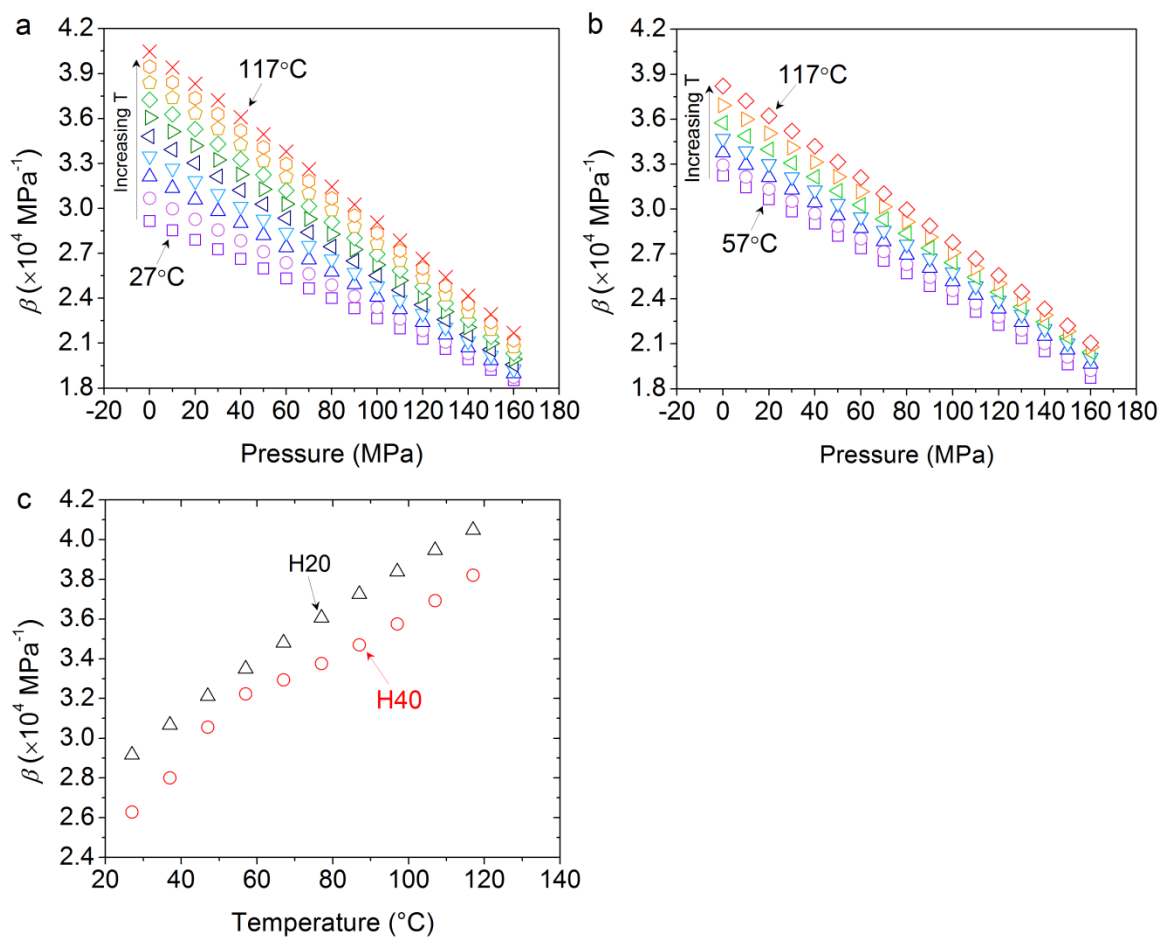


Figure 45. Isothermal compressibility,  $\beta_m$ , curves as a function of pressure for Boltorn (a) H2O between 27-117°C and (b) H4O between 57-117°C. (c) Isothermal compressibility,  $\beta_m$ , as a function of temperature at  $p = 0$  for H2O and H4O.

### Local Free Volume

The local free volume in Boltorn H2O and H4O was probed by PALS. The average hole-size,  $v_h$ , as a function of temperature in the melt and glassy states are shown in Figure 46. The glass transition temperature was determined from the intersection of two straight lines fitted to the melt and glassy  $v_h$  values. The values of  $T_g$  from PALS,  $2.8 \pm 0.2^{\circ}\text{C}$  for H2O and  $36 \pm 6^{\circ}\text{C}$  for H4O, were similar to those determined from DSC. In the melt state,  $v_h$  increased with temperature as molecular and/or segmental motion increased rapidly. The thermal expansion of the hole-size,  $e_{m,h}$ , was similar for each

generation in the melt state,  $0.79 \pm 0.1 \text{ \AA}^3/\text{K}$  for H20  $0.82 \pm 0.2 \text{ \AA}^3/\text{K}$  for H40. In the glassy state, due to the loss of chain mobility, o-Ps was trapped in the local free volume holes within the glassy matrix so that the hole-size corresponded to the size of the pre-existing holes. The thermal expansion of the hole-size in the glass,  $e_{g,h}$ , then considerably decreased as compared to the melt, but was not equal to zero due to the anharmonic molecular vibrations and local motions in the vicinity of the holes.<sup>17</sup> The  $e_{g,h}$  values were similar for both generations,  $0.13 \pm 0.01 \text{ \AA}^3/\text{K}$  for H20 and  $0.15 \pm 0.02 \text{ \AA}^3/\text{K}$  for H40. The larger hole-size of H20 in the melt state may have resulted from the higher segmental mobility of H20 molecules, which were composed of shorter, less bulky chain segments as compared to H40. A visual representation of the different shapes of H20 vs. H40 can be found in Chapter II. As low temperatures were approached, both H20 and H40 transitioned into the glassy state at a similar critical hole-size value  $54 \pm 1 \text{ \AA}^3$  for H20, and H40  $62 \pm 4 \text{ \AA}^3$ , supporting the free volume glass transition theory which states that upon approaching a critical free volume size, the polymer vitrifies due to insufficient space for diffusion steps.<sup>25</sup> In the glassy state the hole-size was similar for each generation. This behavior was also observed for linear polystyrenes where the lower-molecular weight species displayed larger hole-sizes in the melt state but similar hole-size in the glassy state.<sup>26</sup>

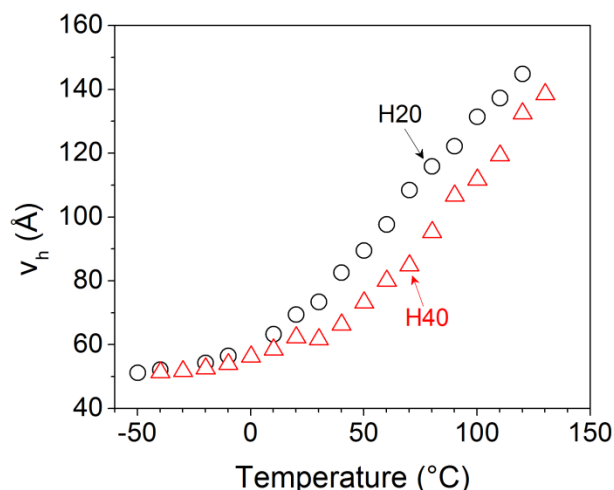


Figure 46. Average free volume hole-size ( $v_h$ ) as a function of temperature of Boltorn H20 and H40 determined from PALS.

Nanoscale thermodynamics were characterized by calculating the thermal expansion coefficient of the hole-size for Boltorn H20 and H40, which was compared with the analogous macroscale thermal expansion coefficient of specific volume. Previously it was observed that approximately 80 to 100°C above  $T_g$ , the increase in the o-Ps lifetime with temperature slowed down and leveled off due to a number of reasons, one of which was that the structural relaxation time of the polymer reaches the order of  $\tau_3$  leading to a smearing of holes during the lifetime of o-Ps.<sup>17,27,28</sup> Although this effect, referred to as the formation of the positron “bubble” state,<sup>28</sup> was not obvious in the  $v_h$ -T plots of H20 and H40 (Figure 46), the hole-size values corresponding to  $T > T_g + 80^\circ\text{C}$  were not used in calculation of the thermal expansion coefficients. A binomial fit was applied to the  $v_h$ -T data, between 30 to 80°C for H20 and 40 to 100°C for H40, and the first derivative at each temperature was divided by the respective hole-size to yield the thermal expansion coefficient of the hole size in the melt  $\alpha_{h,m} = (1/v_h)(\partial v_h/\partial T)$ . The values of the thermal expansion coefficient of hole-volume were a magnitude larger than those of the macroscopic volume, which was observed for nylon-6 as well.<sup>27</sup> This may

indicate that the hole-size changed more rapidly than the macroscopic volume in the melt state. Interestingly, similar to the trend observed for the macroscopic volume, a negative correlation between  $\alpha_{h,m}$  and temperature was observed for H20 while the  $\alpha_{hm}$  values for H40 were constant in the melt range. Mesophase ordering was found to affect local free volume in addition to macroscale volume for the lower generation species, H20.

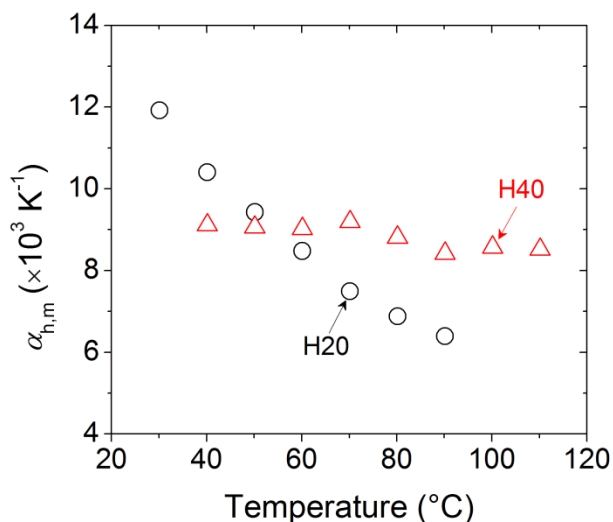


Figure 47. The variation of the melt thermal expansion coefficient of the hole-size,  $\alpha_{h,m}$ , with temperature.

#### *Free and Occupied Volume: SS vs. Dlubek's Method*

Total free volume and occupied volume were determined for the second and fourth pseudo-generation bis-MPA hyperbranched polyesters in the melt range utilizing two different approaches: the SS theory and Dlubek's method. The resultant  $V_f$  and  $V_{occ}$  values for each generation and from each approach were compared.

The wellness of the SS fit to the experimental V-T data is shown in Figure 48. The simplified universal interpolation expression (equation 12) was applied to the V-T data using a non-linear curve fit in OriginPro<sup>®</sup> (v8.0724 Northampton, MA), yielding the scaling parameters  $V^*$ ,  $0.794 \pm 0.002$  cc/g for H20 and  $0.7767 \pm 0.0006$  cc/g for H40,

and  $T^*$ ,  $11511 \pm 122$  K for H2O and  $11990 \pm 57$  K for H4O. The SS EOS provided a better fit for the V-T data of H4O (Figure 49b) as compared to H2O (Figure 49a), as the standard error associated with  $V^*$  and  $T^*$  were an order of magnitude smaller for H4O than for H2O and shown by a larger  $R^2$  value for H4O, 0.999, as compared to H2O, 0.997. The fit may have been less accurate for H2O because the SS lattice-hole theory was not able to account for hydrogen bond-mediated ordering. The ordering was experimentally observed as the densification of volume at low temperatures (Figure 41) for H2O, but not for H4O. The fit quality was acceptable for H2O though since the difference between the experimental and SS volume at each temperature was less than 0.1%. The Boltorn HBPs displayed a similar fit quality as poly(benzyl ether) dendrimers.<sup>2</sup> The reduced variables,  $\tilde{V}$  and  $\tilde{T}$  were calculated using the scaling parameters, and the occupied fraction,  $y$ , was determined at each temperature by solving equation 9 using *Solver* (Microsoft Excel). The occupied volume ( $V_{occ} = yV$ ) and free volume ( $V_f = (1 - y)V$ ) were calculated accordingly. Figure 50 presents the SS determined  $V_{occ}$  and  $V_f$  values in comparison with the analogous values from Dlubek's method.

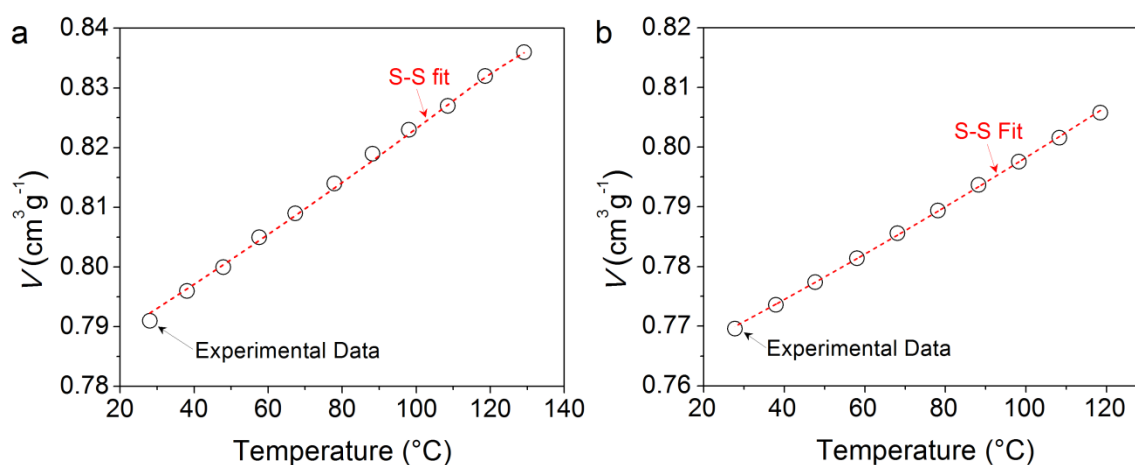


Figure 48. SS EOS fit (red dashed line) to experimental specific volume from PVT dilatometry (open circles) for Boltorn (a) H2O and (b) H4O.

While the SS approach utilizes a set of theoretical assumptions, the only assumption made in Dlubek's method is that the number density of holes,  $N_h$ , is relatively constant in the melt state. The number density of holes was estimated by the following relations

$$V = V_{occ} + N_h v_h \quad (14)$$

$$N_h = E_f / e_{h,r} \quad (15)$$

where  $V_f = N_h v_h$ .<sup>17</sup> The total specific volume,  $V$ , and the specific free volume,  $V_f$ , are each plotted for the temperature range  $T > T_g$  as a function of  $v_h$  in Figure 49a and b respectively. Because both  $V$  and  $V_f$  follow a linear function for  $T > T_g$ ,  $N_h$  was assumed to be constant as a function of temperature. This behavior was observed for other polymers as well.<sup>17,28</sup> The values for  $N_h$  from equation 14,  $5.61 \pm 0.08 \cdot 10^{20}$  holes/g for H20 and  $5.1 \pm 0.2 \cdot 10^{20}$  holes/g for H40, and equation 15,  $5.38 \pm 0.09 \cdot 10^{20}$  holes/g for H20 and  $4.8 \pm 0.2 \cdot 10^{20}$  holes/g for H40, were in good agreement. H20 displayed approximately a 10% greater hole-density than H40 in the melt range.

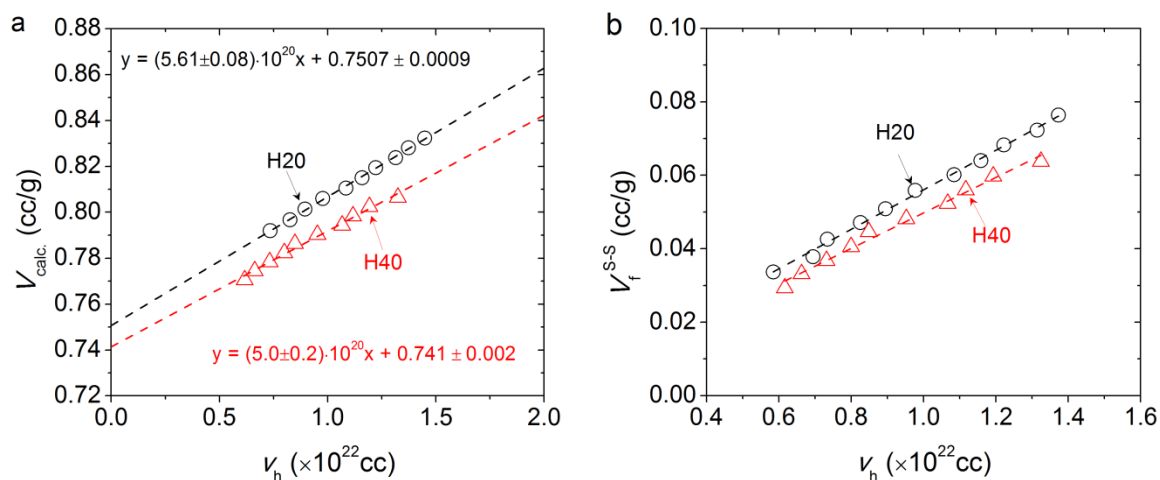
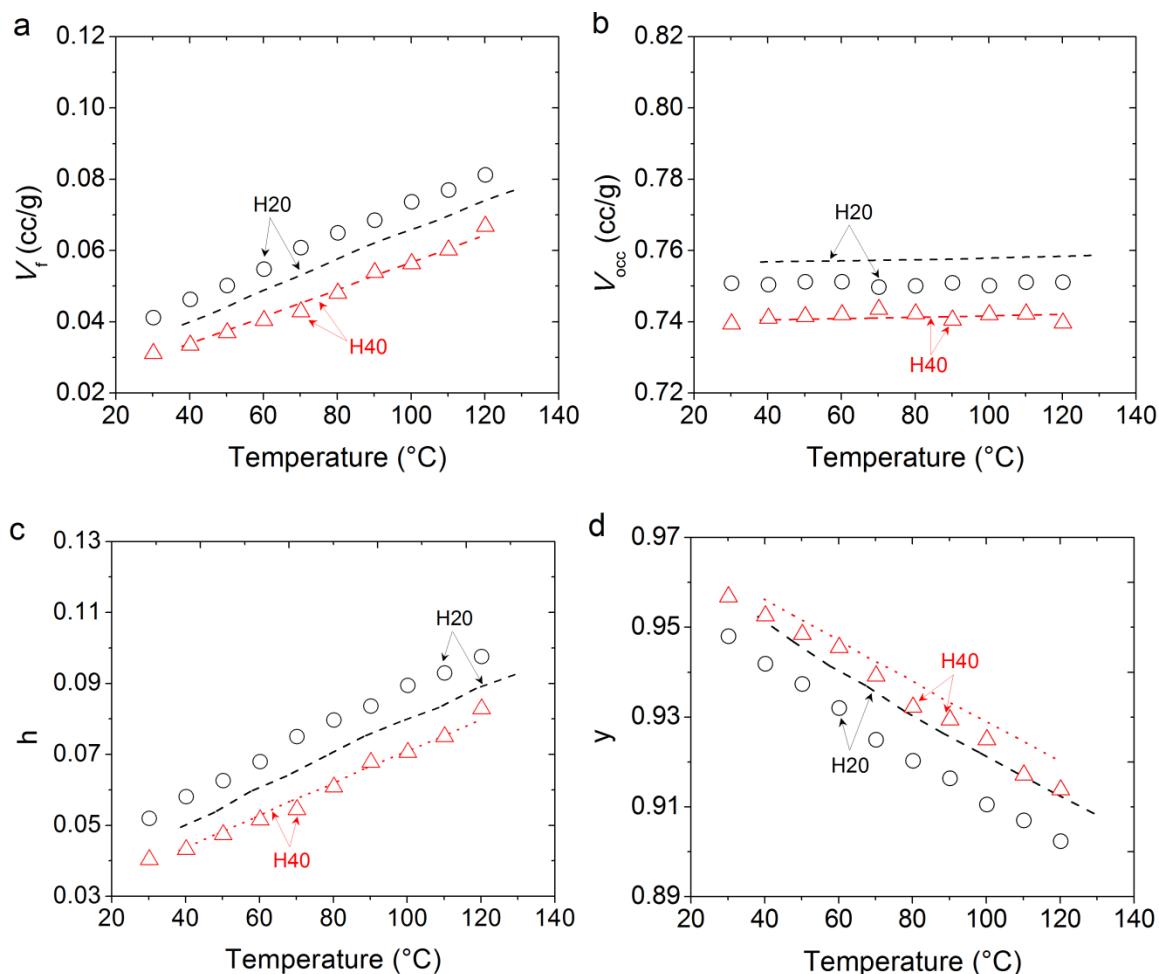


Figure 49. (a) Total volume ( $V_{calc.}$ ) from PVT dilatometry and (b) specific free volume ( $V_f^{SS}$ ) from SS EOS, as a function of average hole-size ( $v_h$ ) for Boltorn H20 and H40. The dashed lines represent the linear fit for each respective data set.



The values for  $V_f$  and  $V_{occ}$  for Boltorn H20 and H40, calculated using the  $N_h$  values from equation 14, were plotted as a function of temperature in Figure 50. The SS EOS and Dlubek's method produced the same final result, that H20 had greater free and occupied volume compared to H40 in the melt state. The  $V_f$  and  $V_{occ}$  values calculated through the SS EOS for H40 were in good agreement the analogous values determined through Dlubek's method. For H20 however, the SS free volume was slightly lower, and the SS occupied volume was slightly higher than the analogous Dlubek's method values. The discrepancy in the H20 results was not surprising due to the propensity of H20 to form mesophase more readily than H40. The SS EOS may have underestimated the free volume for H20 since the lattice-hole theory does not account for structural ordering.



**Figure 50.** Specific (a) free volume ( $V_f$ ) and (b) occupied volume ( $V_{occ}$ ) and fractional (c) free volume ( $h$ ) (d) occupied volume, ( $\gamma$ ) for Boltorn H20 and H40. Open symbols represent values calculated from the Dlubek approach and the dashed lines represent calculations from the SS EOS.

#### *Simulated Volume-Temperature SS Analysis: Free and Occupied Volume*

Volume-temperature curves for the second and fourth generation bis-MPA dendrimers, D20 and D40, and the second pseudo-generation bis-MPA HBP, H20, were simulated using Materials Studio (Accelrys, San Diego). Presented in Chapter II and replotted in Figure 51 below are the simulated V-T curves for D20, D40, and H20. The experimental V-T curves of Boltorn H20 and H40 are shown in Figure 51 for comparison. Although the simulated V-T data were in good agreement with the

experimental trends, each simulated data set was more scattered than the analogous experimental one. The fourth generation dendrimer, D40, showed the most scattering and the largest deviation from linearity as the  $R^2$  value was the lowest, 0.868. The second generation dendrimer, D20, and HBP, H20, displayed slightly less scattering than D40, but the  $R^2$  values of D20 and H20, 0.923 and 0.926 respectively, were still lower than that of experimental H20, 0.999. The melt thermal expansivity of simulated D20 and H20,  $(4.3 \pm 0.4) \cdot 10^{-4} \text{ cm}^3/\text{g} \cdot \text{K}$  and  $(4.6 \pm 0.4) \cdot 10^{-4} \text{ cm}^3/\text{g} \cdot \text{K}$  respectively, were within  $\pm 4\%$  of the experimental  $E_m$  of H20,  $(4.43 \pm 0.03) \cdot 10^{-4} \text{ cm}^3/\text{g} \cdot \text{K}$ , thus showing good agreement with experimental thermodynamic quantities. The  $E_m$  of simulated D40,  $(3.2 \pm 0.4) \cdot 10^{-4} \text{ cm}^3/\text{g} \cdot \text{K}$ , was 19% lower than the experimental thermal expansivity of H40,  $(3.99 \pm 0.01) \cdot 10^{-4} \text{ cm}^3/\text{g} \cdot \text{K}$ . It was unclear whether this difference in expansivity of D40 vs. Boltorn H40 was due to a different thermal expansion behavior of the dendrimer vs. the HBP or due to simulation errors. The overall effect of generation number on thermal expansion was the same in the simulated systems as the experimental ones, where the lower generation simulated dendritic polymers, D20 and H20, displayed a higher  $E_m$  than the higher generation dendrimer D40.

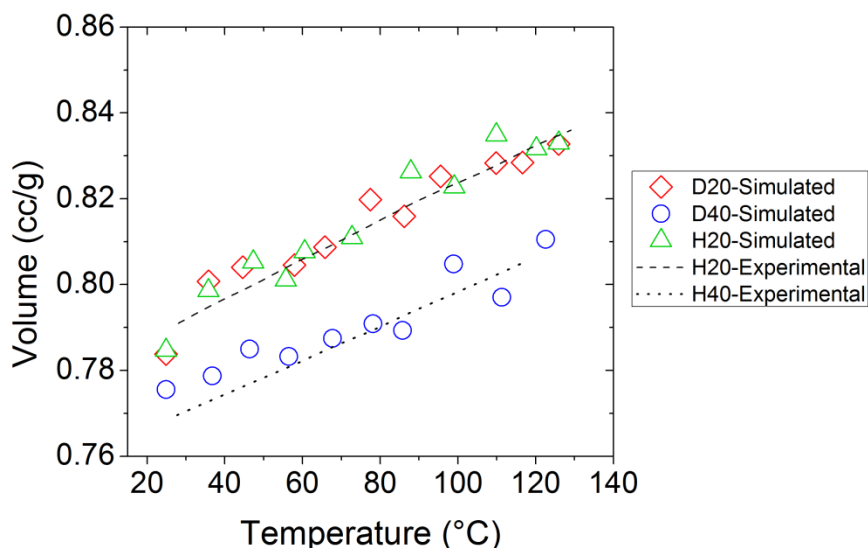


*Figure 51.* Simulated volume-temperature (V-T) points at atmospheric pressure for simulated D2O, D4O and H2O. The experimental V-T curves at ambient pressure are shown as a dashed line for Boltorn H2O and a dotted line for Boltorn H4O.

Following the same procedure used for the experimental V-T data sets, each simulated data set was fit to the universal interpolation expression, yielding the scaling parameters  $V^*$  and  $T^*$ ,  $0.799 \pm 0.009$  cc/g and  $11816 \pm 768$  K for D2O,  $0.80 \pm 0.01$  cc/g and  $13858 \pm 1174$  K for D4O, and  $0.79 \pm 0.01$  cc/g and  $11216 \pm 705$  K for H2O. The large amount of scattering in the simulated V-T data sets, produced less accurate SS fits, as compared to the fit quality of the analogous experimental data sets, evidenced by the lower  $R^2$  values and higher standard errors associated with  $V^*$  and  $T^*$  (Table 8).

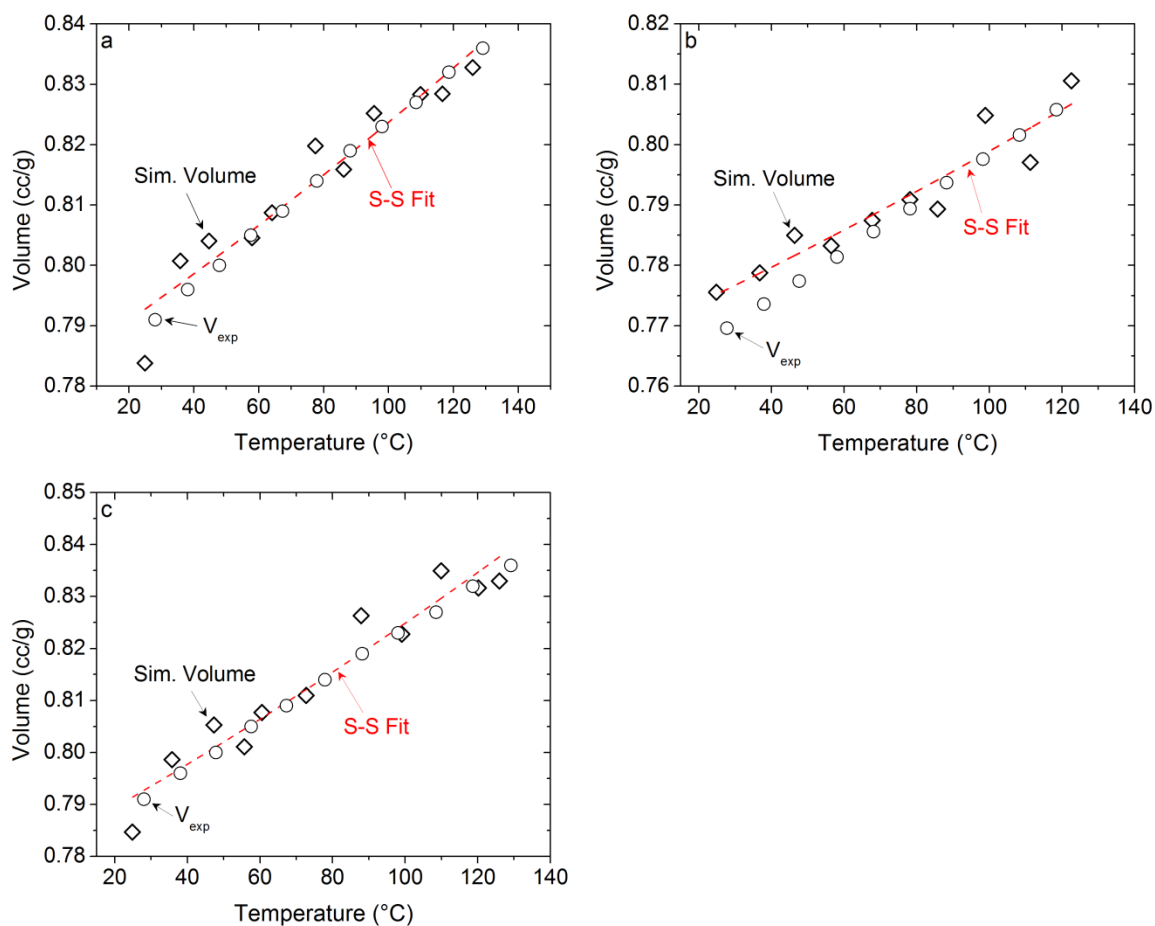


Figure 52. The SS fit (dashed line) to the simulated volume-temperature data sets of (a) D20, (b) D40, and (c) H20. Each analogous experimental V-T data set, Boltorn H20 for (a) and (c) and Boltorn H40 for (b) is plotted with the simulated data.

Table 8

*Scaling and SS Fit Parameters for Experimental Boltorn H20 and H40, as well as simulated D20, D40, and H20*

	V*	T*	Adj. R <sup>2</sup>	Reduced $\chi^2$
H20 <sup>e</sup>	0.794 ± 0.002	11511 ± 122	0.9975	5.4 · 10 <sup>-7</sup>
H40 <sup>e</sup>	0.7767 ± 0.0006	11990 ± 57	0.9995	6.7 · 10 <sup>-8</sup>
D20 <sup>s</sup>	0.799 ± 0.009	11816 ± 768	0.9136	1.9 · 10 <sup>-5</sup>
D40 <sup>s</sup>	0.80 ± 0.01	13858 ± 1174	0.8725	1.6 · 10 <sup>-5</sup>
H20 <sup>s</sup>	0.79 ± 0.01	11216 ± 705	0.9189	2.2 · 10 <sup>-5</sup>

Table 8 (continued).

---

<sup>e</sup> experimental system

<sup>s</sup> simulated system

The occupied fraction,  $y$ , was solved utilizing the same approach used for the experimental data set and  $V_{occ}$  and  $V_f$  were calculated accordingly. Figure 53 presents the SS determined the occupied and free volume for each simulated system, D20, D40, and H20, in comparison to the analogous experimental  $V_{occ}^{SS}$  and  $V_f^{SS}$  values. The simulated analysis displayed that D20 and H20 had similar free and occupied volume, and that D20 had a larger free volume than, but similar occupied volume as, D40 in the melt range. The high amount of scattering in the simulated D40 V-T data set reduced the accuracy of the predicted free and occupied volume. The free volume for D40 was lower than that of Boltorn H40, and the occupied volume of D40 was higher than that of Boltorn H40. The overall conclusion made from the simulated SS analysis, as compared to the experimental SS analysis, was similar in terms of free volume, since the lower generation dendrimer had greater free volume than the higher generation dendrimer, but was different in predicting the occupied volume.

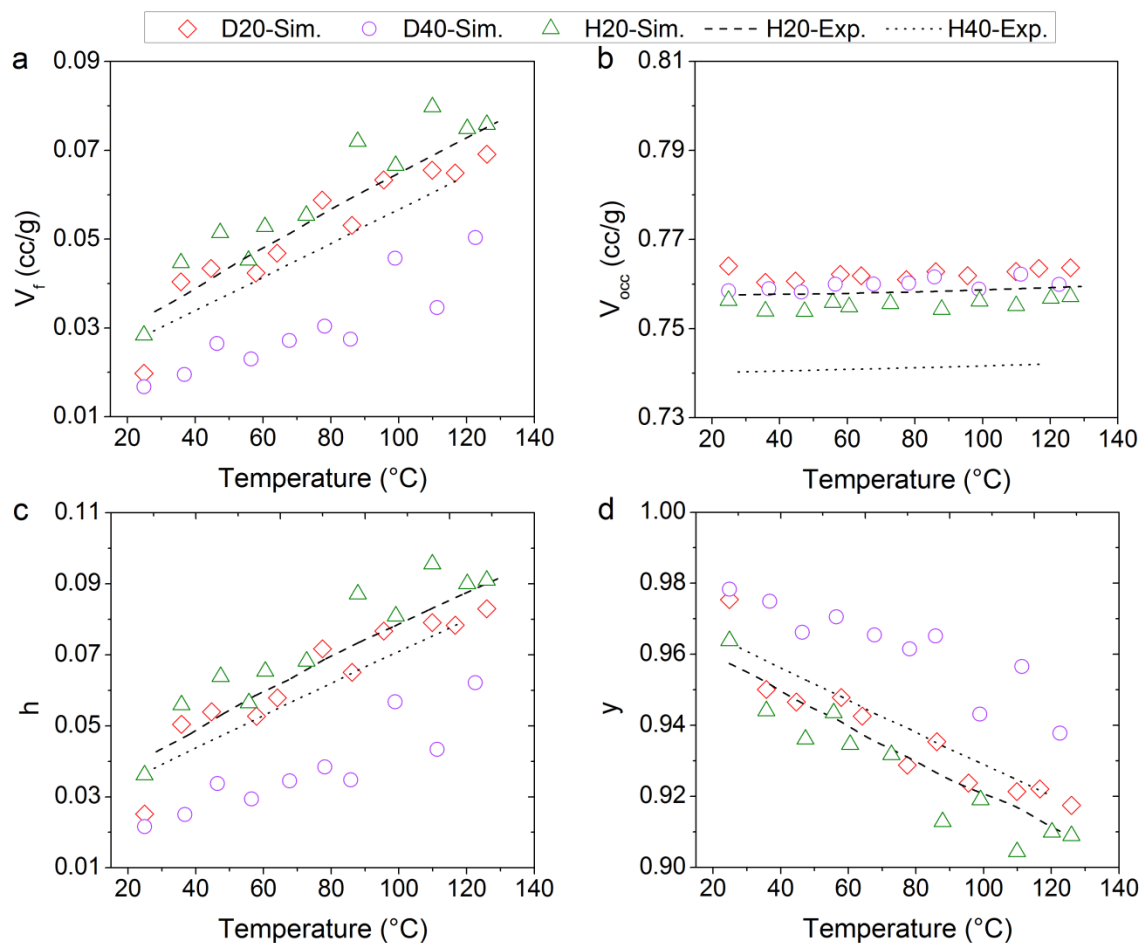


*Figure 53.* (a) Free and (b) occupied volume, and fractional (c) free and (d) occupied volume results calculated by the SS EOS for simulated D20, D40, and H20. In each plot, the analogous experimental SS EOS  $V_f$  and  $V_{occ}$  values for Boltorn H20 (dashed line) and Boltorn H40 (dotted line) are displayed.

### Conclusions

The volumetric and thermodynamic properties of Boltorn H20 and H40 were experimentally determined using PVT dilatometry and PALS, and compared with the analogous properties of simulated D20, D40, and H20. The lower generation hyperbranched polymer, H20, displayed greater specific volume, thermal expansivity and isothermal compressibility values in the melt state as compared to the higher generation H40. H20 displayed a larger hole size than H40 in the melt state, but upon reaching some critical value, the hole size converged for both generations in the glassy state. The

volumetric and thermodynamic properties of the HBPs were not unusually different from other linear polymers and dendrimers. The mobility of H20 molecules was observed to be greater than that of H40 through both specific volume and hole-size thermal expansivity, explaining the enhanced mesophase formation of H20 over H40.

At ambient pressure, the hydrogen bond mediated mesophase ordering (Chapter III) affected the volumetric and thermodynamic properties of H20 only, due to the relatively short time-scale of the experiments (R.O.3). A slight densification of volume was observed immediately above  $T_g$ , indicating that mesophase formation was significantly large enough to affect macroscale properties. Additionally, the negative correlation between the thermal expansion coefficient and temperature, for both the specific volume and hole size, suggested that at lower temperatures, as mesophase formed, an overall greater mobility of the bulk polymer was observed. Evidence of mesophase formation for H40 was observed at increased pressure.

Application of the SS theory to the Boltorn HBPs described the PVT surface of the HBPs well but the lattice-hole theory was not able to account for the hydrogen bond-mediated structural ordering observed for H20 at lower temperatures. Both the SS and Dlubek method produced the same conclusion that the lower generation HBP, H20, had greater free and occupied volume than the higher generation HBP, H40 in the melt state.

The simulated bulk volume and thermal expansivity of the perfect dendrimers D20, D40, and hyperbranched polymer H20 displayed good agreement with the analogous experimental trends, indicating that MD simulations were able to approximate the physical properties of dendritic molecules in the bulk (R.O.5). The determination of free volume through the application of the SS theory was problematic due to the



relatively high amount of scatter in the simulated V-T points as compared to experimentally V-T points. Therefore, an alternative method must be determined to probe free volume in the simulated systems. Future work will entail collection of experimental PVT data for the perfect dendrimers, which will be used to validate the simulated volume points.

#### References

1. Hay, G.; Mackay, M. E.; Hawker, C. J. Thermodynamic properties of dendrimers compared with linear polymers: General observations. *J. Polym. Sci. Part B: Polym. Phys.* **2001**, *39*, 1766-1777.
2. Simha, R.; Utracki, L. A. PVT properties of linear and dendritic polymers. *J. Polym. Sci. Part B: Polym. Phys.* **2010**, *48*, 322-332.
3. Odian, G. Dendritic (Highly Branched) Polymers. in *Principles of Polymerization*; John Wiley & Sons, Inc., 2004, pp 174-180.
4. Hawker, C. J.; Farrington, P. J.; Mackay, M. E.; Wooley, K. L.; Fréchet, J. M. J. Molecular Ball Bearings: The Unusual Melt Viscosity Behavior of Dendritic Macromolecules. *J. Am. Chem. Soc.* **1995**, *117*, 4409-4410.
5. Mourey, T. H.; Turner, S. R.; Rubinstein, M.; Fréchet, J. M. J.; Hawker, C. J.; Wooley, K. L. Unique behavior of dendritic macromolecules: intrinsic viscosity of polyether dendrimers. *Macromolecules* **1992**, *25*, 2401-2406.
6. Fréchet, J. M. J. Functional Polymers and Dendrimers: Reactivity, Molecular Architecture, and Interfacial Energy. *Science* **1994**, *263*, 1710-1715.

7. Turner, S. R.; Voit, B. I.; Mourey, T. H. All-aromatic hyperbranched polyesters with phenol and acetate end-groups: synthesis and characterization. *Macromolecules* **1993**, *26*, 4617-4623.
8. Kilburn, D.; Dlubek, G.; Pionteck, J.; Bamford, D.; Alam, M. A. Microstructure of free volume in SMA copolymers I. Free volume from Simha–Somcynsky analysis of PVT experiments. *Polymer* **2005**, *46*, 859-868.
9. Utracki, L. A.; Simha, R. Pressure-Volume-Temperature Dependence of Polypropylene/Organoclay Nanocomposites. *Macromolecules* **2004**, *37*, 10123-10133.
10. Robertson, R. E.; Simha, R. Volume Relaxation and The Lattice-Hole Model. in *Polymer Physics: From Suspensions to Nanocomposites and Beyond*; Utracki, L. A., Jamieson, A. M., Eds.; John Wiley & Sons, Inc., 2010, pp 163-164.
11. Utracki, L. A.; Simha, R. Analytical Representation of Solutions to Lattice-Hole Theory. *Macromolecular Theory and Simulations* **2001**, *10*, 17-24.
12. Kobayashi, Y.; Zheng, W.; Meyer, E. F.; McGervey, J. D.; Jamieson, A. M.; Simha, R. Free volume and physical aging of poly(vinyl acetate) studied by positron annihilation. *Macromolecules* **1989**, *22*, 2302-2306 .
13. Simha, R.; Somcynsky, T. On the Statistical Thermodynamics of Spherical and Chain Molecule Fluids. *Macromolecules* **1969**, *2*, 342-350.
14. Kluin, J. E.; Yu, Z.; Vleeshouwers, S.; McGervey, J. D.; Jamieson, A. M.; Simha, R.; Sommer, K. Ortho-positronium lifetime studies of free volume in polycarbonates of different structures: influence of hole size distributions. *Macromolecules* **1993**, *26*, 1853-1861.

15. Chang, G.-W.; Jamieson, A. M.; Yu, Z.; McGervey, J. D. Physical aging in the mechanical properties of miscible polymer blends. *J. Appl. Polym. Sci.* **1997**, *63*, 483-496.
16. Dlubek, G. Local Free-Volume Distribution From PALS and Dynamics of Polymers. in *Polymer Physics: From Suspensions to Nanocomposites and Beyond*; Utracki, L. A., Jamieson, A. M., Eds.; John Wiley & Sons, Inc., 2010, pp 421-472.
17. Dlubek, G.; Bondarenkob, V.; Pionteck, J.; Supejb, M.; Wutzlerd, A.; Krause-Rehberg, R. Free volume in two differently plasticized poly(vinyl chloride)s: a positron lifetime and PVT study. *Polymer* **2003**, *44*, 1921-1926.
18. Dlubek, G.; Kilburn, D.; Alam, M. A. Temperature and Pressure Dependence of  $\alpha$ -Relaxation and Free Volume in Poly(vinyl acetate). *Macromol. Chem. Phys.* **2005**, *206*, 818-826.
19. Chen, R. H. Thermodynamics for Liquid Crystals. in *Liquid Crystal Displays*; John Wiley & Sons, Inc.: Hoboken, NJ, 2011, pp 111-123.
20. Dlubek, G.; Pionteck, J.; Rätzke, K.; Kruse, J.; Faupel, F. Temperature Dependence of the Free Volume in Amorphous Teflon AF1600 and AF2400: A Pressure-Volume-Temperature and Positron Lifetime Study. *Macromolecules* **2008**, *41*, 6125-6133.
21. Hamada, F.; Wunderlich, B.; Sumida, T.; Hayashi, S.; Nakajima, A. Density and heat of fusion of folded chain polyethylene crystals. *J. Phys. Chem.* **1968**, *72*, 178-185.

22. Lagaron, J. M.; Vickers, M. E.; Powell, A. K.; Davidson, N. S. Crystalline structure in aliphatic polyketones. *Polymer* **2000**, *41*, 3011-3017.
23. Righetti, M. C.; Di Lorenzo, M. L.; Angiuli, M.; Tombari, E. Structural Reorganization in Poly(butylene terephthalate) during Fusion. *Macromolecules* **2004**, *37*, 9027-9033.
24. Jang, J.; Lee, D. K. Plasticizer effect on the melting and crystallization behavior of polyvinyl alcohol. *Polymer* **2003**, *44*, 8139-8146.
25. Cohen, M. H.; Grest, G. S. Liquid-glass transition, a free-volume approach. *Phys. Rev. B* **1979**, *20*, 1077-1098 .
26. Cavallo, D.; Gardella, L.; Alfonso, G. C.; Portale, G.; Balzano, L.; Androsch, R. Effect of cooling rate on the crystal/mesophase polymorphism of polyamide 6. *Colloid Polym. Sci.* **2011**, *289*, 1073-1079.
27. Dlubek, G.; Redmann, F.; Krause-Rehberg, R. Humidity-induced plasticization and antiplasticization of polyamide 6: A positron lifetime study of the local free volume. *J. Appl. Polym. Sci.* **2002**, *84*, 244-255.
28. Srithawatpong, R.; Peng, Z. L.; Olson, B. G.; Jamieson, A. M.; Simha, R.; McGervey, J. D.; Maier, T. R.; Halasa, A. F.; Ishida, H. Positron annihilation lifetime studies of changes in free volume on cross-linking cis-polyisoprene, high-vinyl polybutadiene, and their miscible blends. *J. Polym. Sci. Part B: Polym. Phys.* **1999**, *37*, 2754-2770.

## CHAPTER V

## CONCLUDING REMARKS AND FUTURE DIRECTIONS

Through synergistic efforts of computer simulations and experimentation, the current understanding of the bulk hydrogen bond organizations, and volumetric and thermodynamic properties of dendrimers and HBPs has been improved upon, where the fundamental findings reported herein have a wider impact on the improvement of synthetic procedures and assignment of potential niche applications of dendrimers and HBPs.

The pervasive and ambiguous H-bond microstructure of the bis-MPA dendritic polymers was defined through the identification of two ordered H-bond topologies. A routine procedure for statistically analyzing the hydrogen bond characteristics via simulations was established, which will be utilized in all future work. The high concentration of hydroxyl end-groups and interior carbonyl, ester, and ether moieties participated in the formation of hydrogen bond assisted chain-like-clusters in the bulk of both the perfect dendrimers and HBPs (R.O.1). These chain-like-clusters remarkably bared resemblance to hydrogen bond clusters observed in small molecule fluids such as water and HF. Because the formation of tetrahedral clusters endows water with unique physical properties, it was speculated that these chain-like-clusters in the dendritic polymers may constitute a key organization responsible for favorable physical properties such as enhanced mechanical strength, increased glass transition temperature, and higher viscosity.

A second hydrogen bond organization, unique to the bis-MPA HBPs only, was defined as a pseudo-hexagonally packed mesophase consisting of small aggregates of

parallel and straight linear chain segments with cylindrical symmetry, constituting the fundamental geometry responsible for the previously observed structural ordering phenomenon (R.O.2). Because the mesophase was assumed to be conformationally disordered, it was interesting to find that the kinetics and thermodynamics of the 2-D mesophase aggregates mimicked those of 3-D crystalline polymers. Through the annealing of the HBPs, at temperatures above their glass transition and below 120°C, linear chain segments were able to associate through lateral hydrogen bonds, forming cylindrical aggregates of various radii but relatively uniform length. The amount of mesophase formation for each generation was optimized by annealing at a temperature approximately 30-40°C above  $T_g$  but the total amount of mesophase formed was limited to the percent and availability of linear segments in each polymer. Identifying the specific packing structure of this ordered phase will aid in fine-tuning and perhaps enhancing mesophase formation for the potential use of HBPs in smart-technology applications, specifically in the area of self-healing films.

A bridge between the structure and hydrogen bonding organizations of dendritic polymers and their bulk physical properties was built (R.O.3). The more “open” structure of the second generation HBP as compared to the fourth generation, was visually observed in Chapter II, and resulted in a greater amount of total free volume, larger hole-size, as well as higher thermal expansivity in the melt state, indicating that the molecules of H20 had greater mobility as compared to those of H40, which also explained the enhanced structural ordering of H20 as compared to H40 observed from X-ray and DSC experiments. The thermal expansivity values of H20 and H40 lay on the lower end of the spectrum when compared to other polymers. The slight thermal expansion suppression

may be a result of extensive hydrogen bonding through the chain-like-clusters in the bulk. Although the transition from an ordered mesophase to isotropic liquid was undetectable as a first order transition from volume-temperature curves, structural ordering was found to affect the nanoscale hole-size as well as macroscale volumetric thermal expansion coefficient of H<sub>2</sub>O.

The second and fourth generation PP50 core, bis-MPA based perfect dendrimers, D20 and D40, and HBPs, H20 and H40, were successfully modeled (R.O.4). The globular molecular shape in the bulk was fundamentally different for the dendrimers and HBPs, where the former molecules were more spherical and the latter more elongated, irregular, and pancake-shaped. For the perfect dendrimers as generation number increased, the shape transitioned from relatively spherical to ellipsoidal whereas for the hyperbranched polymer a similar type of shape was observed between H20 and H40. In simulating bulk volumetric and thermodynamic properties, better agreement was observed between the experimental and simulated free volume results for the second generation than for the fourth generation. Simulations may be useful for approximating the thermal expansivity of the HBPs and dendrimers but application of the Simha-Somcynsky theory to simulated volume-temperature data did not yield results similar to experimental ones (R.O.5).

This dissertation laid the foundation for future studies, which will investigate the effect of molecular architecture on hydrogen bond topologies and physical properties through the synergistic efforts of computer simulations and experimental techniques. Through collaboration with Dr. Grayson at Tulane University a series of bis-MPA based structural isomers (Figure 54) of the perfect dendrimer, hyperbranched polymer, and

linear polymer will be synthesized and the role of key variables such as end-group reactivity, generation number, and degree of branching will be determined. These materials will also be prepared using 2,2-bis(hydroxymethyl)butyric acid, or bis-MBA monomer, shown in Figure 54D, where situating the butyl group between the hydroxyls, instead of the methyl group of bis-MPA, may interfere with the formation of the hydrogen bonded chain like clusters, changing the bulk physical properties of the resultant polymers. Perfect dendrimers based on a pentaerythritol core will also be prepared to study the effect of branching architecture and core symmetry. All experimental materials will be modeled and their bulk hydrogen bond structure and physical properties will be simulated.

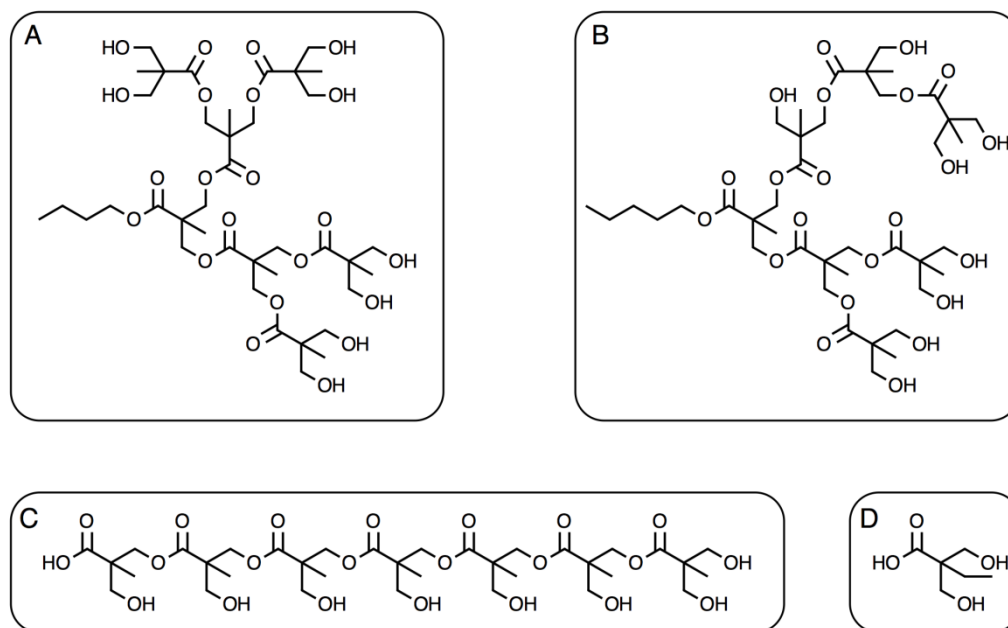


*Figure 54.* Schematic of the bis-MPA based 7-mer structural isomers of the (A) perfect dendrimer, (B) hyperbranched polymer, and (C) linear polymer. Structure (D) is of the monomer 2,2-bis(hydroxymethyl)butyric acid, bis-MBA.

An understanding of the chemical reactivity of the end-groups is necessary to optimize applications such as cross-linking, self-assembly, and peripheral drug-loading,



and also to improve the synthesis and modification of dendritic polymers. The chemical reactivity of the different types of end-groups in the dendrimers, HBPs, and linear polymers will be studied using Matrix-Assisted Laser Desorption/Ionization Time-of-Flight Mass Spectrometry (MALDI-ToF MS) and  $^1\text{H}$  Nuclear Magnetic Resonance (NMR) spectroscopy, each technique providing complementary information. Preliminary scouting work was performed in this dissertation on Boltorn H40, where the kinetics of crosslinking with hexamethylene diisocyanate and end-capping with hexyl isocyanate were probed using  $^1\text{H}$  NMR spectroscopy (Figure 55). The NMR spectra display the consumption of the different types of hydroxyl groups, terminal (4.5 ppm) and linear (4.9 ppm), as well as the formation of the urethane proton product. This preliminary research revealed the formation of a third type of hydroxyl group called “pseudo-linear,” observed as a shoulder in the linear hydroxyl group peak (Figure 55, highlighted region), which was representative of a “deactivated” hydroxyl adjacent to a reacted terminal hydroxyl group. The deactivation event of a terminal hydroxyl may be a fundamental reaction mechanism leading to  $\text{DB} < 1$  during HBP synthesis. Through monitoring the kinetics it was determined that terminal hydroxyls were more reactive than linear hydroxyls and once formed, the pseudo-linear hydroxyls were also consumed. Although all hydroxyl end-groups were available for reaction, long reaction times, approximately 1 week, were needed to fully functionalize all hydroxyl groups, which highlighted the globular nature of these polymers.

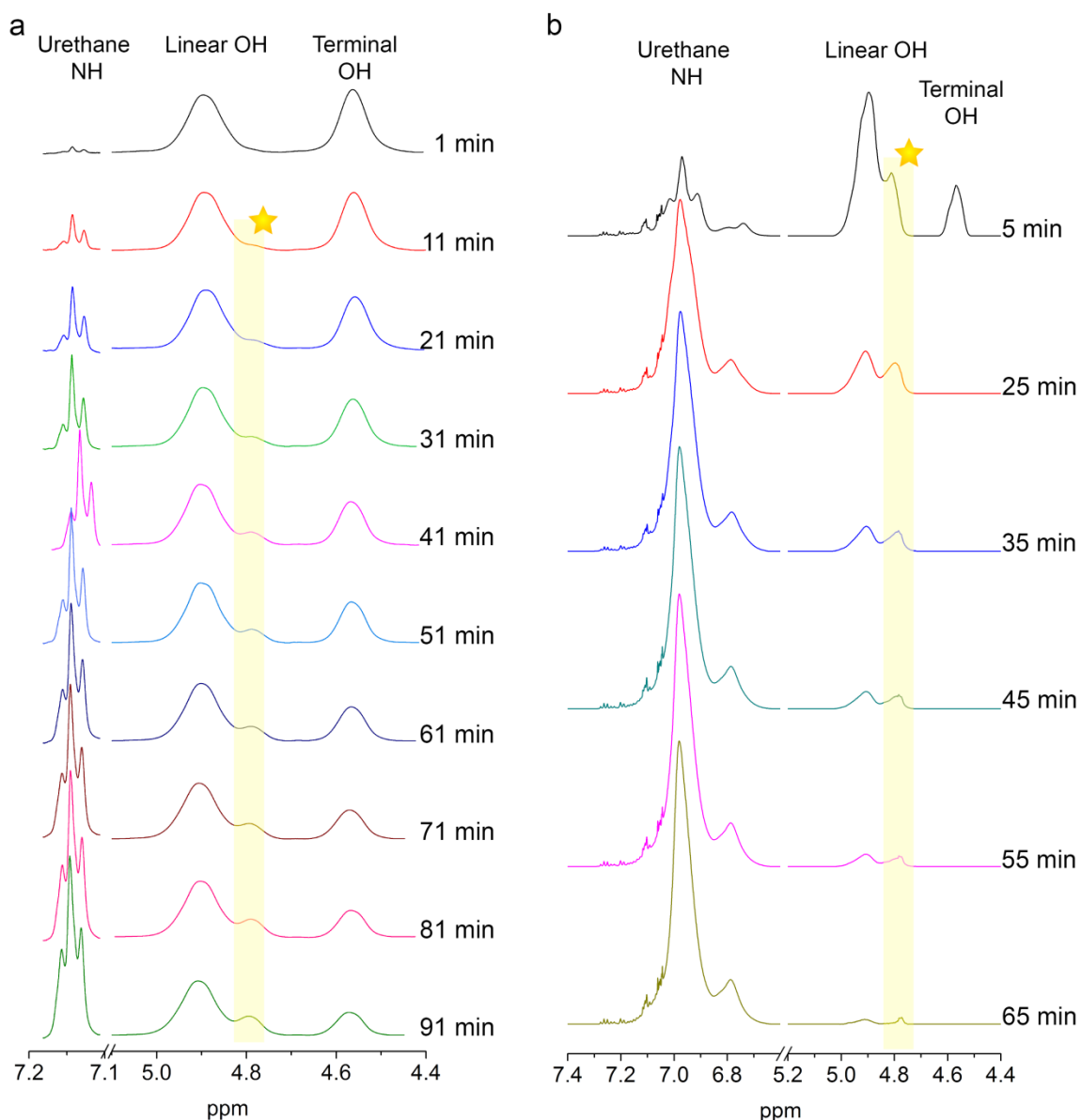


*Figure 55.* NMR spectra for the kinetics of end-capping Boltorn H40 at 90°C with (a) hexamethylene diisocyanate and (b) hexyl isocyanate. The gold star and yellow rectangle indicate the formation and consumption of the third type of hydroxyl group, "pseudo-linear."

Because atomistic MD simulations are limited in the range of system size and time scale they can reach, future work will attempt to model the pseudo-hexagonal mesophase formation in the bis-MPA HBPs using coarse-grained MD simulations. The current simulations of D20 and D40 will be compared with experimental PVT behavior

dendrimers synthesized by Dr. Grayson's research group. Since the Simha-Somcynsky analysis provided a poor fit to the relatively scattered simulated volume-temperature curves of D20, D40, and H20, an alternative method will be established to calculate the free volume of simulated structures.

APPENDIX  
SUPPLEMENTARY FIGURES

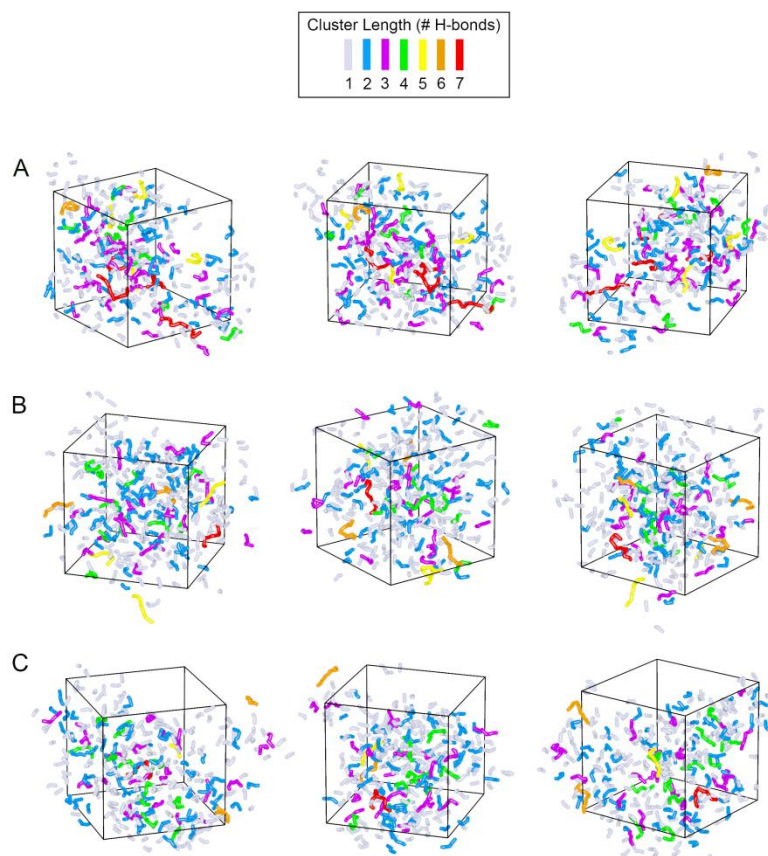


*Figure 56.* Three-dimensional view of “chain-like-clusters” in the final relaxed amorphous cells of (A) D40, (B) H20, and (C) H40. Three rotated views of the amorphous cell are shown. Hydrogen and oxygen atoms, as well as covalent and hydrogen bonds are represented by sticks, to form a continuous O-H $\cdots$ O representation of a cluster. All types of oxygen atoms were included in the clusters. The different colors represent clusters of different lengths.

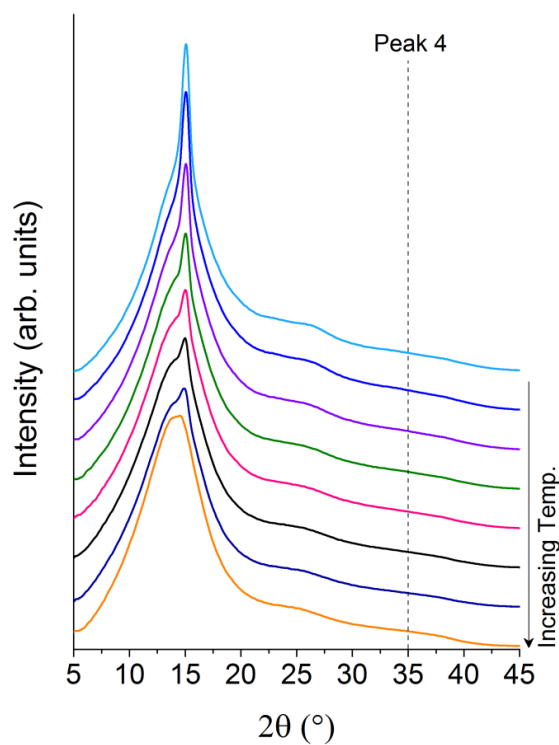


Figure 57. Synchrotron X-ray patterns ( $\lambda = 0.1371$  nm) for Boltorn H20, collected over a wide angular range, at room temperature and higher temperatures. Curves were shifted vertically for clarity. The dashed line indicates Peak 4 ( $2\theta \approx 35^\circ$ ).

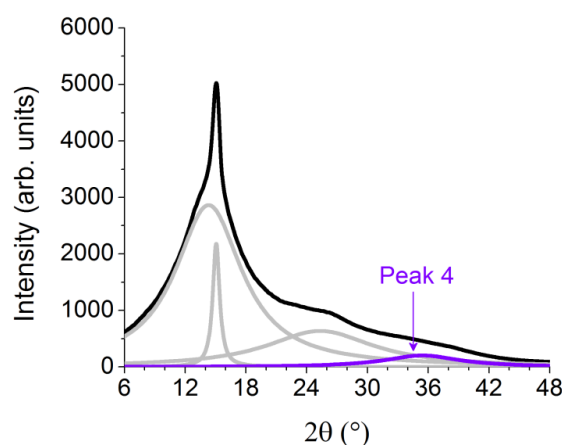


Figure 58. Deconvolution of synchrotron X-ray pattern ( $\lambda = 0.1371$  nm) for Boltorn H20 at room temperature. Peaks 1-3 are shown in grey and Peak 4 is shown in purple at  $2\theta \approx 35^\circ$ .